Structure, shape and dynamics of biological membranes

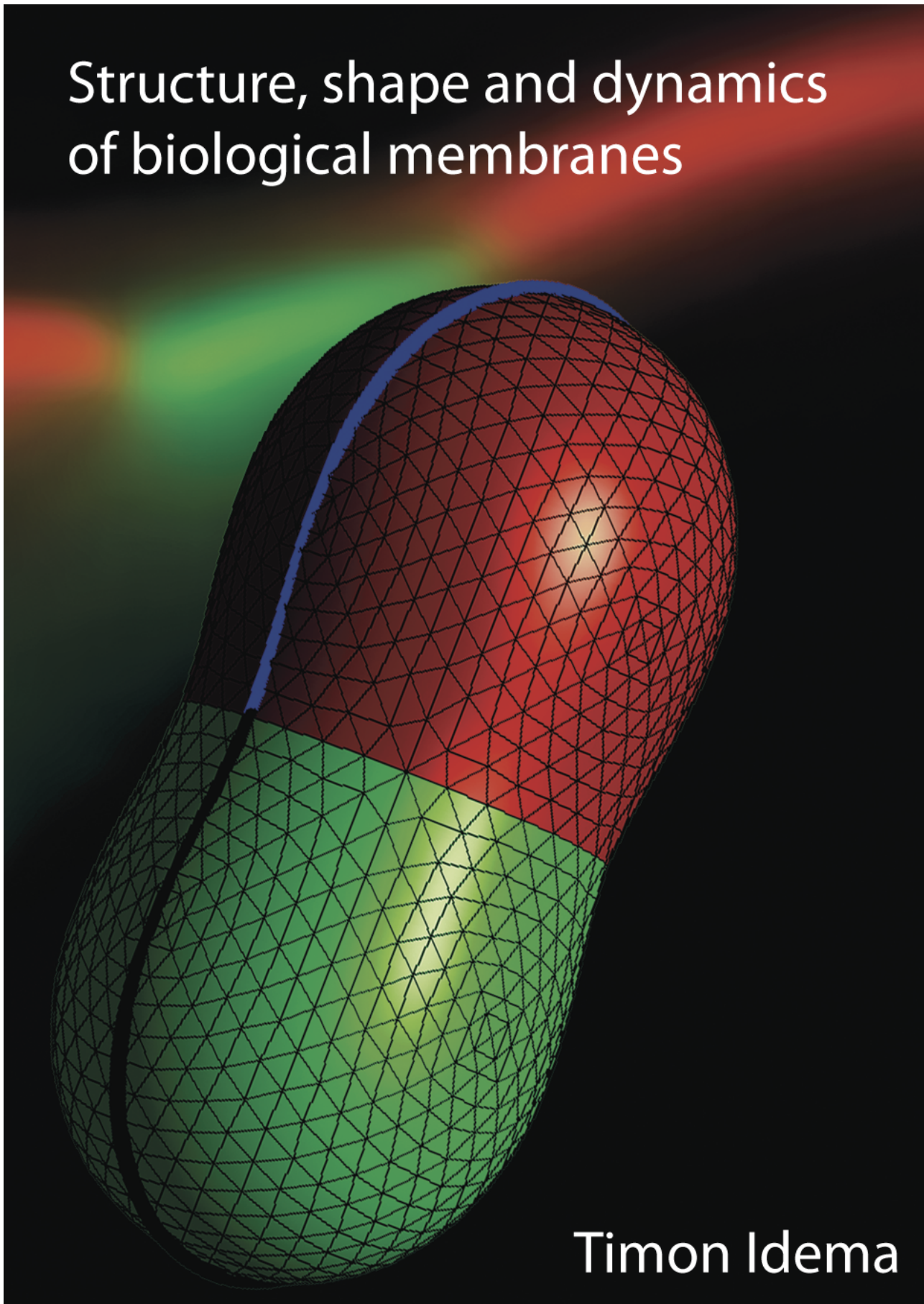

Timon Idema

Structure, shape and dynamics of biological membranes

P R O E F S C H R I F T

ter verkrijging van
de graad van Doctor aan de Universiteit Leiden,
op gezag van Rector Magnificus prof. mr. P. F. van der Heijden,
volgens besluit van het College voor Promoties
te verdedigen op donderdag 19 november 2009
klokke 13.45 uur

door

Tymen Idema

geboren te Winterswijk
in 1981

Promotiecommissie:

Promotor:	prof. dr. H. Schiessel
Co-Promotor:	dr. C. Storm (Technische Universiteit Eindhoven)
Overige leden:	prof. dr. T. Schmidt
	prof. dr. M. A. Peletier (Technische Universiteit Eindhoven)
	prof. dr. B. A. Mulder (Universiteit Wageningen / AMOLF)
	prof. dr. J. van Ruitenbeek

ISBN 978-90-8593-060-0
Casimir PhD Series, Delft-Leiden 2009-15
Dit werk maakt deel uit van het onderzoekprogramma van de Stichting voor Fundamenteel Onderzoek der Materie (FOM), die financieel wordt gesteund door de Nederlandse Organisatie voor Wetenschappelijk Onderzoek (NWO).

CONTENTS

CHAPTER 1

INTRODUCTION

Biophysics is the study of the physics behind biological processes. Biophysicists therefore want to know both *how* things happen in living systems and *why* they happen. The terrain where both disciplines overlap, and both these questions can be asked, is mainly a single cell. A cell is large enough to be a living system in its own right, and thanks to recent advances in observational techniques the different processes within the cell that make up its life cycle can now be studied in great detail. It would be a gross exaggeration to state that a single cell is simple enough to be within the reach of a description in terms of elementary physics, however, in some simplified cases, these same cellular processes can also be studied from a physicists point of view. Living systems have to abide by the laws of physics every bit as much as billiard balls and planets do, and even though they are much more complicated, the basic rules remain the same. Nonetheless, like it is an impossible task to describe the flow of water based on a microscopic description of the motion of all individual molecules, it is not realistic to expect the processes in a much more complicated, living system to be any more tractable. Like in hydrodynamics we have to resort to effective and often phenomenological models based on statistical physics. Even in cases where single-molecule descriptions are possible, we still have to invoke statistics to be able to come up with predictions on the scales available to experiment. Biophysics therefore is mainly statistical physics, and like for example the turbulent flow of water, which has remained a puzzle over the many centuries since it was first studied by Leonardo da Vinci, figuring out the physics behind the fundamental processes that regulate the cell will remain a challenge for many years - if not centuries - to come.

1.1 Cells

Cells are the building blocks of all living creatures. The vast majority of the species that we know of are unicellular. However, the majority of the organisms that we can actually see with the naked eye, like plants and animals, are multicellular. Unicellular organisms were first described by Anthonie van Leeuwenhoek, who used his newly developed microscope to study many different samples in the second half of the 17th century. Simultaneously, Robert Hooke, also known for the law of elasticity named after him, discovered that cork was made of many chamber-like subunits, for which he coined the term cell in 1665. Later on, Hooke also discovered cells in the tissue of living plants. Nonetheless, it took till 1839 for the general cell theory, stating that all living organisms are composed of cells, to be developed by Matthias Schleiden and Theodor Schwann. The general cell theory in its modern form encompasses more that just the statement that cells are the basic subunits of life. It also states that all cells come from preexisting cells, and that they pass on hereditary information from one generation to the next. This information is stored in the genetic code of the DNA molecule found in all cells, which also encodes for all its characteristic properties and functions.

All cells share some common features. They are well-defined compartments bound by a plasma membrane, a bilayer of lipid molecules (see section 1.2). The cells of some groups of organisms (*e.g.* plants) also have a more rigid cell wall outside the plasma membrane, whereas others (*e.g.* animals) do not. The inside of the cell is an aqueous solution containing many chemicals. Genetic information is stored in DNA, a polymer with a double-helix structure. The building blocks of DNA are four both chemically and structurally different bases, which provide four 'letters' in which the genetic information is written. Parts of the DNA known as genes encode for the production of proteins, which are themselves polymers made of amino acids. There are 22 different amino acids known, each of which is coded for by 3 bases in the DNA. Proteins occur in a wide range of types and with a large variety in function. Some are basic structural subunits, while others play important roles in processes like chemotaxis, signaling, transport, cell division and apoptosis (cell death). Proteins are produced from the DNA code in two steps. First, a part of the code (the gene, or a part of it) is transcribed from DNA to an RNA molecule, another biopolymer which also has four different subunits, corresponding to the bases of the DNA. The RNA subsequently gets translated into a protein. This at first sight rather cumbersome method allows for a physical separation between the DNA containing the valuable genetic code, and the many other processes in a cell.

In eukaryotic cells the DNA is stored in a separate compartment called the nucleus. The region outside the nucleus is called the cytoplasm. DNA transcription onto RNA takes place inside the nucleus. After the transcription, the RNA is transported outside the nucleus and translation takes place in the cy-

toplasm. Most eukaryotes have another specialized subunit called the endoplasmic reticulum where RNA translation and protein production takes place. Cells without a nucleus are known as prokaryotes. The division between pro- and eukaryotes is the first that can be made when classifying organisms. All multicellular organisms, including animals, plants and fungi, but also some unicellular ones like yeast, are eukaryotes; all bacteria are prokaryotes. Although it is an exaggeration to state that prokaryotes have no internal structure at all, they do not contain internal membranes separating different parts of the cells in functional units called organelles, like eukaryotes do.

The cells of many eukaryotic species have a high level of internal organization. As indicated above, the boundary between the inside of the cell and the outside world is a lipid bilayer membrane, known as the plasma membrane of the cell. Inside, there are many organelles, subunits with specific functions that themselves are also bounded by lipid bilayer membranes. Examples are the endoplasmic reticulum, the Golgi apparatus (which functions as the distribution center of the cell) and mitochondria (which even have a double membrane and function as the power plant of the cell, converting sugar into the biological fuel ATP).

Apart from being organized into subunits, eukaryotic cells also possess a cytoskeleton. The cytoskeleton is a network of biopolymers which enhances the structure of the cell and provides a network for transportation within the cell. Three types of biopolymers make up the cytoskeleton: microtubules, actin filaments and intermediate filaments. Both microtubules and actin filaments are polar, while intermediate filaments are apolar. Actin filaments are the most flexible part of the cytoskeleton and are predominantly found in the cell cortex, just beneath the plasma membrane. Actin has an important function in cell motility, a process in which cells extend protrusions such as lamellipodia and filopodia, but also in adhesion in mature, stationary cells. Intermediate filaments are found throughout the cell, where they provide it with mechanical strength. Moreover, also intermediate filaments play an important role in cell adhesion, in particular in sheets of epithelial cells (found for instance at the inside surface of all cavities of the body), where they are crucial factors in relaxing mechanical stress. Microtubules are the stiffest component of the cytoskeleton with a persistence length much larger than the size of a cell. They are predominantly radially organized in the cell, with one end usually attached to an organizing center (called the centrosome) close to the nucleus and the other end close to the plasma membrane at the cell periphery. Because they are polar, both microtubules and actin provide platforms for motion of molecular motors through the cell. These motors are responsible for the various transport processes within the cell, as well as for separating the cell into two parts during division. Motors are further introduced in section 1.3.

Cells are by no means static. Even in mature organisms, cells grow and divide to replace dead cells continuously. We call the period that leads from the birth of a cell to the point that it divides the cell cycle. Given the right environ-

mental conditions, the cell cycle of a bacterium can be as short as 20 minutes, whereas that of a cell in a mature multicellular organism can take up to a year. The cycle of an eukaryotic cell can be divided into two clear phases: the interphase or growth phase, and the M or dividing phase. Duplication of the DNA already takes place during the growth phase. During the M phase, first the nucleus is split in two (each containing a complete copy of the DNA), a process known as mitosis. The cell subsequently divides in two separate daughter cells. Prokaryotes have a similar cycle, in which first the DNA is duplicated, after which it is pulled to opposing ends of the cell and the cell divides. In both systems, the proper separation of the DNA is a crucial step, in which molecular motors (and in the case of eukaryotes, also the cytoskeleton) play a vital role.

1.2 Membranes

Biological membranes consist of a double layer of lipid molecules. Lipids are a class of molecules with the common feature that each of them has a hydrophilic (polar) head and up to three hydrophobic tails. There are many different kinds of head groups, exhibiting a rich variation in characteristics like charge and size. The tails always consist of hydrocarbon chains which are mostly saturated, although a single tail may have some unsaturated bonds. Common examples of lipids include cholesterol, fatty acids, phospholipids, sphingolipids and vitamins.

Molecules that contain both hydrophilic and hydrophobic parts are known as amphiphiles and may self-organize in an aqueous environment. The self-organization is driven by the reduction in free energy that can be achieved by shielding the hydrophobic part from the water molecules. If the lipids are roughly wedge-shaped, the shielding can effectively be done by organizing the lipids into micelles, in which the tails are all directed towards a common center point and the head groups face outward (see figure 1.1a). The conical shape is found in lipids which have a large head group and typically only a single hydrocarbon tail. For more cylindrical-shaped lipids the micelle organization is not as advantageous, because the head groups will not be able to completely shield the tails from the (much smaller) water molecules. Such lipids therefore rather organize into lipid sheets which have no intrinsic curvature. To separate the hydrophilic and hydrophobic parts such a sheet should be a bilayer of lipids, with the tails pointing inwards and the heads once again on the outside (see figure 1.1b). In an aqueous environment a lipid bilayer will close up on itself to create a shape without exposed edges, resulting what is known as a liposome or vesicle. The two lipid layers in a vesicle are called the inner and outer leaflet of the membrane. Vesicles have a small curvature, which means that the cylindrically shaped lipids will incur a small bending energy penalty (measured by the bending modulus κ of the lipid bilayer membrane). Moreover, in biological systems the inner and outer leaflet may have different compositions, and the

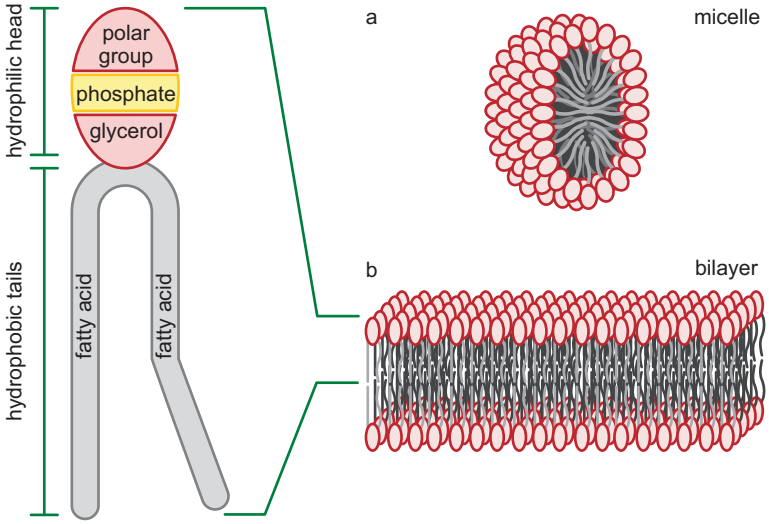

Figure 1.1: Biological membranes are bilayers of lipid molecules. A schematic image of a lipid is shown on the left. Lipids consist of a hydrophilic (polar) head group and one or more hydrophobic tails, which are long fatty acids. In aqueous solution, lipids self-organize into larger structures. Lipids which are cone-like in shape may organize in a micelle (a), more cylindrically-shaped lipids typically organize into bilayers (b). In water, bilayers close up on themselves, creating a vesicle or liposome with aqueous solutions both inside and outside.

inside and the outside of a vesicle may contain different solutions. All biological membranes are lipid bilayer sheets.

Although the biological significance of the head groups is large, in the biomimetic membranes we will focus on in this thesis their role is small. Head groups are used in experiments to specifically attach fluorescent markers, but do not influence the organization of the membrane itself. In contrast, there is an important property of the tail groups of the lipids used which directly influences the membrane structure [1]. Some of the hydrocarbon tail chains are completely saturated, whereas others have a single unsaturated bond. Such an unsaturated bond acts as a kink in the hydrocarbon chain, which has the important consequence that the lipid will have some part of one (or both) of its tails stick out in a random (and variable) orientation. If we build a membrane out of a single species of lipids which has unsaturated tails, we get a structure which is different from a membrane consisting of lipids with saturated tails. The difference can be characterized by looking at the correlation of tail orientations. For unsaturated tails, with parts sticking out in random directions,

these correlations are small; such a membrane is said to be in a liquid disordered (L_d) phase. Saturated tails on the other hand are not as free to choose their orientation and the correlations are much stronger, resulting in what is known as a liquid ordered (L_o) phase. Both phases are fluid, which means that there is no long-range order between the positions of the lipids themselves; the difference is in the ordering of the tails. Especially for saturated-tail lipids it is possible to make a transition to a gel phase, in which also the lipid positions are ordered; however this only occurs at low temperatures and is not a phase that has been observed in living cells.

In a membrane containing both lipids with saturated and unsaturated tails, it is experimentally found that these lipids do not mix well. Especially in the presence of the much smaller cholesterol as a third component, the membrane exhibits demixing into separate L_d and L_o domains below a critical temperature [2–7] (see figures 1.2 and 1.3). The cholesterol is mostly found in the L_o phase (which is rich in saturated-tail lipids), where it 'fills up the gaps' between the straight tails. In chapter 3 we study the properties of the phase diagrams of such ternary systems.

Typically lipids with fully saturated tails are effectively slightly longer than those with unsaturated tails. To keep a closed front of hydrophilic head groups lipids will therefore have to be stretched or compressed close to a domain boundary (see figure 1.2d), resulting in an energy penalty associated with the presence of such a boundary [8–10]. A membrane consisting of multiple lipid types will therefore want to minimize the total domain boundary length, which is the driving force for the separation into domains and the growth of such domains. In chapter 4 we study the effects of this segregation into domains on the vesicle shape.

Biological membranes do not only contain lipids, but also many kinds of proteins. Like lipids, most proteins have both hydrophilic and hydrophobic parts, and in order to shield the hydrophobic parts from the water in a cell's cytoplasm they are embedded in a membrane. Proteins are typically much larger than lipids, and a recent study shows that up to approximately half the mass of the plasma membranes is concentrated in proteins [11]. Proteins which are not cylindrical in shape will locally deform the membrane, and communicate with each other through such membrane deformations. A well-known example is the clathrin-coated pit, where clathrin proteins get recruited to a part of the membrane that is to be budded off. Because of their conical shape the clathrins force the membrane to assume a strongly bent shape, which is subsequently pinched off by another protein called dynamin, creating a small membrane vesicle [12, 13]. Individual proteins are too small to be observed in light microscopes, but lipid domains are not, and we will use them as a probe to study membrane-mediated interactions in detail in chapters 5 and 6.

Although the biomimetic vesicles we study clearly exhibit separation into domains, it is not known whether similar processes also occur in biological membranes in living cells [1]. Simons and Ikonen [14] proposed the existence

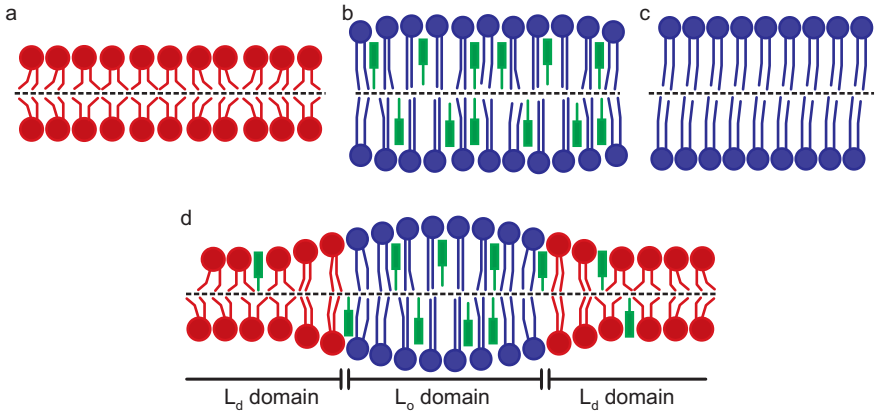

Figure 1.2: Structures of lipid bilayer membranes exhibiting different phases. (a) Liquid disordered (L_d) phase, mostly found in lipids which have one or more unsaturated carbon bonds in their tails. (b) Liquid ordered (L_o) phase, a combination of lipids with saturated tails (blue, two tails) and cholesterol (green, one tail). (c) Gel phase, found for all lipids below their critical temperature. (d) Lipid bilayer with coexisting L_d and L_o domains. Please note that cholesterol is present in both phases, although its concentration in the L_o phase is higher than in the L_d phase.

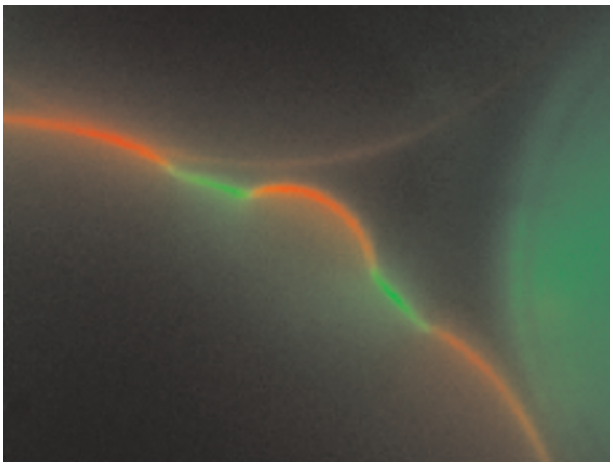

Figure 1.3: Image of a tricomponent membrane exhibiting coexistence of a L_d phase (green) and an L_o phase (red). The line tension between the domains of the two coexisting phases causes the membrane to deform locally, resulting in different curvatures for the different domains. The line tension arises as an energy penalty for phase coexistence within a single membrane. In section 3.4 we calculate the value of the line tension from an expression of the Gibbs free energy for ternary mixtures. In chapter 4, we study the effect the line tension has on the membrane shape.

of such functional domains (or 'rafts') in the plasma membrane as an alternative to the existing fluid mosaic model. The fluid mosaic model [15] states that the plasma membrane is essentially a uniform mixture of many types of lipids and numerous transmembrane and membrane-associated proteins. In the picture sketched by Simons and Ikonen a raft would be an environment enriched in certain types of lipids, creating a preferential environment for some proteins whilst effectively excluding others. Rafts have not been directly observed to date, which means their maximal size is limited to the maximal resolution of optical microscopy, about $100\,\mathrm{nm}$ [16]. Based on the measurement of certain membrane parameters in biomimetic vesicles, and models for domain growth and membrane recycling in living cells, we predict in chapter 4 that rafts in fact can only have a size of about $10\,\mathrm{nm}$. Such small rafts would still be able to organize proteins, but only in very small numbers. Moreover, in this scenario one should ask the question whether the rafts recruit the proteins or the proteins organize their local environment into lipid rafts. For a more thorough introduction into that discussion, see the recent reviews by Lee [17] and Sackmann [18].

1.3 Molecular motors

Molecular motors are the workers of the cell. They convert chemical energy into mechanical work. Because they use energy, motors are able to perform such tasks as creating directed motion and producing concentration gradients. There is a rich variety of types of motors. Examples are the dynamin that pinches off membrane vesicles, DNA and RNA polymerase that read DNA and produce DNA copies or RNA transcriptions, ion pumps that transport sodium or potassium ions across a membrane, and cytoskeletal motors that transport materials through the cell. Molecular motors are proteins, more specifically mechanoenzymes, and depending on their function can have transmembrane or membrane-associated domains. Their fuel is typically ATP (though motors that run on GTP also exist), molecules produced by the mitochondria from the oxidation of sugar, and containing three phosphate groups (indicated by T for three and P for phosphate). Hydrolization of such a molecule (in which it reacts with water and releases one of its phosphate groups, producing ADP and phosphate) releases energy [12]. Motor proteins act as catalysts for this reaction, and during a single cycle (in which they for instance transcribe a single DNA-base) they have different configurations in their free, ATP-bound, and ADP-bound states. The combination of an energy consuming step with a polar polymer to walk on, ensures unidirectionality in the motion of molecular motors.

The motors we study in chapter 7 are microtubule-walkers, which transport membrane vesicles through the cell along the microtubule network. Microtubules are part of the cytoskeleton, and as such already introduced in section 1.1. Microtubules are hollow tubes, made of many copies of polar tubulin dimers, which consist of an α and a β tubulin protein. Typically a microtubule has thirteen subfilaments, in which case the filaments are straight within the microtubule tube. Microtubules with less or more than 13 subfilaments also exist, resulting in a tube with winding subunits. In living cells microtubules constantly grow and shrink at their plus end, and sometimes dissociate from the centrosome and subsequently also shrink from the minus end [19]. They are extremely stiff, with a persistence length of the order of millimeters [20], much larger than the size of a typical cell ($10 - 100\ \mu\mathrm{m}$). Apart from their role as structural components within cells, microtubules are also involved in many dynamic processes, such as mitosis, cytokinesis, and vesicular transport.

Molecular motors occur in two types: processive and nonprocessive ones. Processive motors can take many steps on the polymer they walk on before detaching. Nonprocessive motors can only take a single step. Both types occur frequently: DNA and RNA polymerase are examples of processive motors with high processivity, whereas the myosin motors in muscle cells are strictly nonprocessive. We study both types of motors, and particularly focus on the differences between them.

The motors we study walk on microtubules using one or two active parts,

which are usually called heads. The precise dynamics of walking are subject of intensive study. Recent results show that processive motors walk in a head-over-head fashion: when both heads are bound to the microtubule, the trailing one unbinds, then the leading one makes a power stroke, putting the now free second head in a position such that it can bind in front of the bound motor [21]. Nonprocessive motors can have only one head (as is the case for some actin-walking Myosin motors, *e.g.* Myosin-I), or two heads of which one is either disfunctional or unable to reach the polymer due to structural constraints. Nonprocessive motors can still bind their active head to their associated polymer, and the head can also make a power stroke to push the entire motor forward, but it has to release afterwards because there is no second head that can bind [22, 23]. Nonprocessive motors therefore necessarily need to work cooperatively to exert a continuous force. Processive motors also often exhibit collective behavior, because the force generated by an individual motor is not large enough to perform a required task, and both efficiency and processivity can be increased in a system containing multiple motors. The collective effects of molecular motors have therefore been studied intensively in recent years [24–32], and are the main subject of chapter 7.

CHAPTER 2

DIFFERENTIAL GEOMETRY

Differential geometry is the branch of mathematics that studies geometrical objects in an analytical way, using differential and integral calculus. In this chapter we introduce the differential geometry of curves and surfaces, and apply them to biopolymers and biomembranes. We discuss Gauss's Theorema Egregium and the Gauss-Bonnet Theorem and their implications. We also introduce the Canham-Helfrich free energy which will allow us to calculate the minimal-energy shapes of biomembranes.

2.1 Manifolds

Differential geometry is the branch of mathematics that studies geometrical objects in an analytical way, using differential and integral calculus. Its techniques and results are applicable to many problems in biophysics, and it is particularly suited to describe the behavior of polymers and membranes in three-dimensional space. In the language of differential geometry, we will consider these as one- and two-dimensional manifolds embedded in two- or three-dimensional flat Euclidean space. A manifold is a mathematical object that has the property that around any of its points it is locally flat, although it may be curved and close upon itself on large scales. Locally, an n-dimensional manifold therefore looks like $\mathbb{R}^n$, and we can parametrize it in a local coordinate system $\{x_i\}_{i=1,\ldots,n}$. If there is another point nearby, with another coordinate system $\{y_i\}_{i=1,\ldots,n}$, then there is a continuous bijection between the two in the region where they overlap. On a smooth manifold all such bijections are smooth maps (*i.e.*, if both the map itself and its inverse are infinitely differentiable).

In this chapter we will introduce the differential geometry of curves and surfaces. Both biopolymers and biomembranes have a sufficiently large aspect ratio that they can effectively be described as one- and two-dimensional objects respectively. Unlike for example a soap film, another example of an effectively two-dimensional object, the molecular structure of the polymers and lipid bilayers does have an effect on the total energy of the manifolds. In particular there will be effects on the bending of the manifolds, which are reflected in the curvature energy. It is not known whether biological membranes are smooth or not, or in other words whether nature 'allows kinks' or not. However, there are clearly possibilities to induce kinks, for example by the inclusion of wedge-shaped proteins. Boundaries within the membrane where the physical parameters change are another example. We will consider the membrane to be a smooth manifold within any region for which the physical parameters are the same, and pay particular attention to such boundaries and inclusions.

Although manifolds are mathematical objects by themselves that can exist and be described without the need of any embedding space, in our three-dimensional reality the embedding space does play a role. Some properties of the manifold are intrinsic and therefore the same whichever embedding space we choose, but unfortunately the curvature does not satisfy that condition. We need to make explicit reference to the space in which we see the manifold, and therefore we distinguish between curves in $\mathbb{R}^2$ and curves in $\mathbb{R}^3$. In the case of the membrane there are two different curvatures, one of which is intrinsic, but the other one is not. As we will see in section 2.3.5, for creatures like cells living in the embedding space, the most important curvature in terms of energy contributions will be the extrinsic one, defined only in the larger Euclidean space that is its home.

There is a vast literature on differential geometry, both in the context of

pure mathematics and in the connection with physics. For a thorough introduction into manifolds, including proofs of the theorems in sections 2.3.3 and 2.3.4, see *e.g.* Millman and Parker [33], Spivak [34] or Do Carmo [35]. For an excellent overview of applications of differential geometry to biopolymers and biomembranes, of which many results are used in this chapter, see Kamien [36].

2.2 Differential geometry of curves

2.2.1 Curves in the plane

Since a curve is a one-dimensional object, we can label its points by a single parameter t, running over a real interval $[a, b]$. If we choose a coordinate system for the embedding space $\mathbb{R}^2$, the coordinates of the point labelled by a given value of t can be written as $\vec{r}(t)$. If our curve represents a polymer, and we are interested in the spatial conformation of that polymer, we will want to associate an energy with every possible conformation. As mentioned above, that requires that we consider the curvature of the polymer. In principle we could do that with the description in terms of $\vec{r}(t)$, but our calculations will be significantly simplified by choosing the arc length s as the parameter to measure the length along the curve. The arc length will run from 0 at $\vec{r}(a)$ to L, the length of the curve, at $\vec{r}(b)$. To find an expression for the arc length, we therefore first need to calculate the total length L of the curve. For an infinitesimal parameter step dt, the length of the curve between t and $t + dt$ is given by

$$\left|\left| \lim_{dt\to 0} \frac{\vec{r}(t+dt) - \vec{r}(t)}{dt} \right|\right| = \left|\left| \frac{\mathrm{d}\vec{r}(t)}{\mathrm{d}t} \right|\right|, \tag{2.1}$$

so we can find L by integrating the norm of the tangent vector $\frac{d\vec{r}(t)}{dt}$ to the curve over the interval $[a, b]$:

$$L = \int_a^b \sqrt{\frac{\mathrm{d}\vec{r}(t)}{\mathrm{d}t} \cdot \frac{\mathrm{d}\vec{r}(t)}{\mathrm{d}t}}\, \mathrm{d}t. \tag{2.2}$$

Since the arc length measures distance along the curve, we can simply calculate it from the arbitrary parametrization $\vec{r}(t)$ by calculating the distance from the starting point:

$$s(t) = \int_a^t \sqrt{\frac{\mathrm{d}\vec{r}(u)}{\mathrm{d}u} \cdot \frac{\mathrm{d}\vec{r}(u)}{\mathrm{d}u}}\, \mathrm{d}u. \tag{2.3}$$

Alternatively, by invoking the fundamental theorem of calculus, we also have the relation

$$\frac{\mathrm{d}s}{\mathrm{d}t} = \left|\left| \frac{\mathrm{d}\vec{r}(t)}{\mathrm{d}t} \right|\right|. \tag{2.4}$$

One reason why the arc length is an easy measure to work with, is that the tangent vector expressed in units of arc length becomes a unit vector. To see that this is true, we rewrite the expression (2.2) for the length of the curve in terms of the arc length:

$$L = \int_0^L \sqrt{\frac{\mathrm{d}\vec{r}(s)}{\mathrm{d}s} \cdot \frac{\mathrm{d}\vec{r}(s)}{\mathrm{d}s}}\, \mathrm{d}s. \tag{2.5}$$

Differentiating both sides of (2.5) with respect to L we find

$$\left|\left| \frac{\mathrm{d}\vec{r}(s)}{\mathrm{d}s} \right|\right| = 1. \tag{2.6}$$

The tangent vector is a useful enough quantity to give it its own symbol:

$$\hat{e}_s = \frac{\mathrm{d}\vec{r}(s)}{\mathrm{d}s}, \tag{2.7}$$

where we use the hat to indicate that $\hat{e}_s$ is a unit vector. By associating a tangent vector to every point of the curve we obtain a direction field on the curve. Intuitively it makes sense to associate the curvature of the curve with the rate of change of that direction field as we travel along the curve. A straight line then has zero curvature, whereas the curvature of a sharp bend is large. Splitting that rate of change in a magnitude and direction factor, we can write

$$\frac{\mathrm{d}\hat{e}_s}{\mathrm{d}s} = \kappa(s)\hat{n}(s), \tag{2.8}$$

where $\hat{n}$ is another unit vector. In fact, $\hat{n}(s)$ is perpendicular to $\hat{e}_s$, because the derivative of any unit vector $\hat{x}(s)$ is perpendicular to itself:

$$\begin{aligned} \frac{\mathrm{d}}{\mathrm{d}s}\left[\hat{x}(s) \cdot \hat{x}(s)\right] &= \frac{\mathrm{d}}{\mathrm{d}s}\left[1\right] \\ 2\hat{x}(s) \cdot \frac{\mathrm{d}\hat{x}(s)}{\mathrm{d}s} &= 0. \end{aligned} \tag{2.9}$$

The vector $\hat{n}(s)$ is called the unit normal of the curve and $\kappa(s)$ the curvature. By taking $\hat{n}(s)$ to be positive, the sign of $\kappa(s)$ tells us in which direction the curve is bent, whereas its magnitude tells us how sharp the bend is. Any energy functional we want to construct on the curve when relating it to a polymer should be independent of the direction in which we bend, and therefore can contain only even powers of κ. The most commonly used curvature energy is just the lowest (quadratic) power of κ integrated over the entire curve:

$$\mathcal{E}_{\text{curv}} = \frac{A}{2} \int_0^L \kappa(s)^2\, \mathrm{d}s. \tag{2.10}$$

Here A is a physical parameter, known as the bending modulus of the curve. Based on the energy (2.10) we can apply the toolbox of statistical physics on the ensemble of possible curves. Later on, we will develop a similar expression for the curvature energy of membranes.

Before we continue, there are two more observations to make about more intuitive definitions of the curvature. In colloquial talks and elementary courses the curvature is often defined as the inverse radius of the osculating circle at any point along the curve. That definition is completely equivalent to the one given here, although one loses the information stored in the sign of κ. To see that this is true, we express the magnitude of κ in terms of the original parametrization $\vec{r}(t)$:

$$|\kappa(t)| = \frac{||\vec{r}'(t) \times \vec{r}''(t)||}{||\vec{r}'(t)||^3}, \tag{2.11}$$

where primes denote derivatives with respect to t. If the osculating circle at $\vec{r}(t)$ has radius a, it is parametrized by $a(\cos t, \sin t)$. From equation (2.11), we immediately find that its curvature, and therefore that of the curve, is indeed $1/a$.

The other more intuitive definition is related to a quadratic expansion of the curve around a local minimum. Since our choice of coordinates of the embedding space $\mathbb{R}^2$ is arbitrary, we can always choose coordinates such that the origin is at the point of interest on the curve and that this point is also a local minimum in the coordinates chosen. Moreover, we can locally parametrize the curve by $\vec{r}(t) = (t, y(t))$. Since $\vec{r}(t)$ is a local minimum, the lowest order in the expansion of $y(t)$ is quadratic, and given by $\frac{1}{2}\kappa t^2$. The factor κ that multiplies the quadratic term is indeed the curvature as defined in equation (2.8), as is readily found by substituting the local expression for $\vec{r}(t)$ in equation (2.11) or alternatively equations (2.7) and (2.8). The interpretation of the curvature as the coefficient of the quadratic term in an expansion around a local minimum will be quite helpful later on when we consider the curvature of surfaces.

2.2.2 Curves in space

Curves in $\mathbb{R}^3$ enjoy an additional degree of freedom compared to their counterparts in $\mathbb{R}^2$. That means that at any point along the curve we now need three vectors as a basis for the space in which it lives, and that we can no longer describe the curve in that basis with a single parameter $\kappa(s)$. Instead we will need two parameters, the curvature $\kappa(s)$ (defined analogously to the two-dimensional case) and the torsion $\tau(s)$, which is related to the curve's chirality.

Like in two dimensions, we can parametrize a space curve using the arc length s and describe it in an arbitrary coordinate system by a vector $\vec{r}(s)$. The unit tangent vector $\hat{e}_s$ and normal $\hat{n}(s)$ now are three-dimensional vectors, but still defined by equations (2.7) and (2.8). The definition of the curvature $\kappa(s)$

is still given by equation (2.8) as well. Moreover, since the result (2.9) on the derivative of a unit vector holds in any number of dimensions, the unit tangent and unit normal vector are still orthonormal. To construct a basis for $\mathbb{R}^3$ at $\vec{r}(s)$ all we need to do is find a third vector which is perpendicular to both. That vector is given by their cross product and is known as the binormal

$$\hat{b}(s) = \hat{e}_s(s) \times \hat{n}(s). \tag{2.12}$$

Analogously to the definition of the curvature (2.8), we express the derivative of $\hat{n}(s)$ in terms of the basis $(\hat{e}_s, \hat{n}, \hat{b})$:

$$\frac{\mathrm{d}\hat{n}(s)}{\mathrm{d}s} = \alpha(s)\hat{e}_s + \tau(s)\hat{b}(s). \tag{2.13}$$

The quantity $\tau(s)$ is the torsion of the curve. The geometrical interpretation of the torsion is the rate of change of the osculating plane, the plane spanned by $\hat{e}_s$ and $\hat{n}$. The sign of the torsion is related to the curve's chirality: a left-handed curve has negative torsion, and the torsion of a right-handed curve is positive. The quantity $\alpha(s)$ in equation (2.16) is just the negative of $\kappa(s)$; to see that this is true we differentiate the relation $\hat{e}_s \cdot \hat{n} = 0$ expressing the orthogonality of $\hat{e}_s$ and $\hat{n}$:

$$0 = \frac{\mathrm{d}\hat{e}_s}{\mathrm{d}s} \cdot \hat{n} + \hat{e}_s \cdot \frac{\mathrm{d}\hat{n}}{\mathrm{d}s} = \kappa(s) + \alpha(s). \tag{2.14}$$

By also considering the derivative of $\hat{b}(s)$ we can find an easier expression for the torsion. We have

$$\begin{aligned} \frac{\mathrm{d}\hat{b}(s)}{\mathrm{d}s} &= \frac{\mathrm{d}\hat{e}_s}{\mathrm{d}s} \times \hat{n} + \hat{e}_s \times \frac{\mathrm{d}\hat{n}}{\mathrm{d}s} \\ &= \kappa\hat{n} \times \hat{n} + \hat{e}_s \times (-\kappa\hat{e}_s + \tau\hat{b}) \\ &= -\tau\hat{n}(s) \end{aligned} \tag{2.15}$$

so

$$\tau(s) = -\frac{\mathrm{d}\hat{b}(s)}{\mathrm{d}s} \cdot \hat{n}(s). \tag{2.16}$$

Like the curvature in the two-dimensional case, the combination of the curvature and the torsion at any point along the curve tells us the trajectory of the curve through space. That statement can be neatly summarized by combining the three-dimensional versions of equations (2.8), (2.13), and (2.15) into a single expression

$$\frac{\mathrm{d}}{\mathrm{d}s}\begin{pmatrix} \hat{e}_s(s) \\ \hat{n}(s) \\ \hat{b}(s) \end{pmatrix} = \begin{pmatrix} 0 & \kappa(s) & 0 \\ -\kappa(s) & 0 & \tau(s) \\ 0 & -\tau(s) & 0 \end{pmatrix} \begin{pmatrix} \hat{e}_s(s) \\ \hat{n}(s) \\ \hat{b}(s) \end{pmatrix}. \tag{2.17}$$

Equations (2.17) are known as the Frenet-Serret equations. They beautifully illustrate the symmetry between κ and τ: $\kappa(s)$ is the rate of rotation of $\hat{e}_s(s)$ around $\hat{b}(s)$ and $\tau(s)$ that of $\hat{n}(s)$ around $\hat{e}_s(s)$.

Much of the biophysical theory of polymers relies on the differential geometry of curves introduced in this section. Since our main focus is on membranes, those theories lie outside the scope of this text. For a further introduction see *e.g.* De Gennes [37] and Kamien [36].

2.3 Differential geometry of surfaces

2.3.1 Coordinate system and area element

Just like the curves in the previous section, a surface in three-dimensional space can be described in terms of the coordinates of that embedding space. Because the surface itself is two-dimensional, we will need two local coordinates to parametrize it. As was already alluded to in the introduction of this chapter, a particular choice of these coordinates may be valid only locally and not cover the entire surface, however, there will always a continuous bijection to another set of coordinates with which we can carry on. We will make use of this freedom of coordinate choice to choose a system best adapted to the particular problem at hand later on. For now we will take a set of two arbitrary coordinates (x_1, x_2) and write our mathematics in terms of them, making sure along the way that the results are independent of the particular choice we make here.

The first major difference with the curve is that on a surface there is no natural choice of coordinates like the arc length. Moreover, not only do we now need two numbers to characterize the curvature, there will actually be two ways of defining a proper coordinate independent curvature on the surface. One of them, the Gaussian curvature, will turn out to be intrinsic, which means it is not only independent of the coordinates chosen but also of the space in which we embed the surface. Moreover, the Gaussian curvature will be related to the topology of the surface. The other (extrinsic) curvature, known as the mean curvature, will play a role very similar to the curvature of the curve in the previous section.

Having chosen a coordinate system on the surface, we can associate a point in $\mathbb{R}^3$ with every point of the surface $\mathcal{M}$ and write

$$\mathcal{M} = \{\vec{r}(x_1, x_2) \,|\, x_1, x_2 \in \mathcal{U}\}, \tag{2.18}$$

where $\mathcal{U} \subset \mathbb{R}^2$ is the set of points over which x_1 and x_2 run. Similarly to the case of the curve, we can define tangent vectors to the surface by taking derivatives with respect to the parameters:

$$\vec{e}_1 = \frac{\partial \vec{r}(x_1, x_2)}{\partial x_1}, \tag{2.19}$$

$$\vec{e}_2 = \frac{\partial \vec{r}(x_1, x_2)}{\partial x_2}. \tag{2.20}$$

Lacking a natural length scale, we get tangent vectors which are neither necessarily normalized nor necessarily perpendicular to each other. Nonetheless, they do span a two-dimensional plane which is tangent to the surface at $\vec{r}(x_1, x_2)$. In order to construct a third vector which is perpendicular to both tangent vectors (so that the three of them span $\mathbb{R}^3$) we only need to calculate their cross product

$$\hat{n} = \frac{\vec{e}_1 \times \vec{e}_2}{||\vec{e}_1 \times \vec{e}_2||}, \tag{2.21}$$

where we have normalized this time to get a proper surface normal. By introducing the surface normal field on $\mathcal{M}$ (*i.e.*, by assigning a surface normal to each point of $\mathcal{M}$), we can classify the manifold as being *orientable* or *non-orientable*. The surface is orientable if at every point of the manifold we can consistently orient the tangent vectors $\vec{e}_1$ and $\vec{e}_2$ with respect to the normal $\hat{n}$, *e.g.* in such a way that using the right hand rule we can define a clockwise direction for every loop in the surface. For a surface which is both orientable and closed, we can use the normal vector field to define an inside and an outside of the manifold. Well-known examples of orientable, closed manifolds are the two-dimensional sphere and torus embedded in $\mathbb{R}^3$, and an example of a closed but non-orientable manifold is the Klein bottle. We will assume our manifolds to be closed and orientable from now on, and choose the direction of the normal vector such that it points outwards. We will also typically choose the coordinate system on $\mathbb{R}^3$ which we use to describe $\mathcal{M}$ such that its origin lies inside the space enclosed by the surface.

Using the tangent vectors defined above, we can calculate the infinitesimal area element at each point of the surface, and by integrating over $\mathcal{U}$ find the total surface area. The infinitesimal area element at $\vec{r}(x_1, x_2)$ is simply the area of the parallelogram spanned by the two tangent vectors, which in turn is given by the magnitude of their cross product:

$$\begin{aligned} \Delta S &= ||\vec{e}_1 \times \vec{e}_2|| \\ &= \sqrt{(\vec{e}_1 \times \vec{e}_2)^2} \\ &= \sqrt{||\vec{e}_1||^2||\vec{e}_2||^2 - (\vec{e}_1 \cdot \vec{e}_2)^2}. \end{aligned}$$

By putting back in the definitions of the tangent vectors we find the differential area element to be

$$\mathrm{d}S = \sqrt{(\partial_1\vec{r}(x_1,x_2))^2(\partial_2\vec{r}(x_1,x_2))^2 - (\partial_1\vec{r}(x_1,x_2)\cdot\partial_2\vec{r}(x_1,x_2))^2}\,\mathrm{d}x_1\,\mathrm{d}x_2, \tag{2.22}$$

where $\partial_i = \frac{\partial}{\partial x_i}$. The expression under the square root in equation (2.22) is exactly the determinant of the *induced metric* (or *first fundamental form*). The induced metric of an n-dimensional manifold with tangent vectors $\vec{e}_i$ is an (n, n) tensor given in component form by $g_{ij} = \vec{e}_i \cdot \vec{e}_j$; for our two-dimensional

manifold $\mathcal{M}$ it is given by

$$g(x_1,x_2) = \begin{pmatrix} \vec{e}_1(x_1,x_2)\cdot\vec{e}_1(x_1,x_2) & \vec{e}_1(x_1,x_2)\cdot\vec{e}_2(x_1,x_2) \\ \vec{e}_2(x_1,x_2)\cdot\vec{e}_1(x_1,x_2) & \vec{e}_2(x_1,x_2)\cdot\vec{e}_2(x_1,x_2) \end{pmatrix}. \tag{2.23}$$

For the total area of the manifold we can now write the elegant formula

$$\mathcal{A} = \int_{\mathcal{U}} \sqrt{\det g(x_1,x_2)}\,\mathrm{d}x_1\,\mathrm{d}x_2. \tag{2.24}$$

Although the expression (2.24) for $\mathcal{A}$ makes explicit use of a parametrization $\mathcal{U}$ of $\mathcal{M}$, the resulting area is independent of the parametrization chosen. To prove that statement, we consider a change of parametrization from a set of coordinates (x_1,x_2) that runs over $\mathcal{U}$ to another set (y_1,y_2) that runs over $\mathcal{V}$. Applying the chain rule, we find

$$\vec{e}_{x_i} = \frac{\partial\vec{r}}{\partial x_i} = \frac{\partial\vec{r}}{\partial y_k}\frac{\partial y_k}{\partial x_i} = \frac{\partial y_k}{\partial x_i}\vec{e}_{y_k}, \tag{2.25}$$

where we implicitly sum over the repeated index k. Applying the transformation (2.25) to the metric, we find

$$g_{ij}(x_1,x_2) = \frac{\partial y_k}{\partial x_i}\frac{\partial y_m}{\partial x_j}\tilde{g}_{km}(y_1,y_2), \tag{2.26}$$

where $\tilde{g}$ is the metric in the coordinate system (y_1,y_2). If we now define the transformation matrix X by $X_{ik} = \frac{\partial y_k}{\partial x_i}$, then we can rewrite equation (2.26) in matrix form as $g = X^T\tilde{g}X$. Returning to the expression (2.24) for the total membrane area, we find that a parameter transform does indeed not change the value of $\mathcal{A}$:

$$\begin{aligned} \mathcal{A} &= \int_{\mathcal{U}} \sqrt{\det g(x_1,x_2)}\,\mathrm{d}x_1\,\mathrm{d}x_2 \\ &= \int_{\mathcal{U}} \sqrt{\det(X^T\tilde{g}(x_1,x_2)X)}\,\mathrm{d}x_1\,\mathrm{d}x_2 \\ &= \int_{\mathcal{U}} \sqrt{\det\tilde{g}(x_1,x_2)}|\det X|\,\mathrm{d}x_1\,\mathrm{d}x_2 \\ &= \int_{\mathcal{V}} \sqrt{\det\tilde{g}(y_1,y_2)}\,\mathrm{d}y_1\,\mathrm{d}y_2, \end{aligned}$$

where the last equality holds because $|\det X|$ is exactly the Jacobian for the coordinate transformation from (x_1,x_2) to (y_1,y_2).

A parametrization that is often used is the *Monge gauge*, in which the membrane surface $\mathcal{S}$ is described as a height function $h(x,y)$ above $\mathbb{R}^2$ (parametrized by x and y). In that case we have $\vec{r} = (x,y,h(x,y))$ and the expression for

the total area reduces to

$$\mathcal{A} = \int_{\mathcal{U}} \sqrt{1 + \left(\frac{\partial h}{\partial x}\right)^2 + \left(\frac{\partial h}{\partial y}\right)^2}\, \mathrm{d}x\, \mathrm{d}y. \tag{2.27}$$

For objects such as soap films, which have no bending resistance, the only contribution to the total energy scales with the surface area

$$\mathcal{E}_{\text{area}} = \sigma \mathcal{A}, \tag{2.28}$$

where σ is the surface tension. A well-known example of a surface which minimizes the 'area energy' (2.28) is the shape of a soap film in between two rings, called a catenoid.

2.3.2 Curvature of surfaces

Even though biomembranes are fluid in their lateral direction and therefore, like the soap film, do not have any internal structure in that direction, their energy is not given by the simple expression (2.28). The membrane does have a characteristic bilayer structure in the direction normal to its surface, which means that bending the membrane will deform that structure and therefore carry an energy penalty. To construct a proper energy functional that describes the membrane shape we should therefore include curvature contributions.

As observed above, we will need two numbers at each point of the surface to characterize the curvature at that point. There is a straightforward way of getting two such numbers using the machinery we have already developed. Each of the combinations $(\vec{e}_1, \hat{n})$ and $(\vec{e}_2, \hat{n})$ of a tangent vector and the surface normal spans a plane which intersects $\mathcal{S}$ at our point of interest. The intersections are curves in $\mathbb{R}^2$, and the curvature of these curves in those planes are given by equation (2.8). Clearly these two curvatures of intersection lines depend on the particular choice of coordinates (x_1, x_2) we made. We get different values by rotating our coordinate axes, where any orientation (except parallel) of them with respect to each other is valid. By virtue of the surface being smooth these rotations will give us a maximum c_1 and minimum c_2 value of the intersection line curvatures. The numbers c_1 and c_2 are called the principal curvatures of the surface at (x_1, x_2), and their associated directions the principal directions (see figure 2.1a). By construction, the principal curvatures are independent of the choice of coordinates. They are however not the easiest quantities to work with. Instead, we use two combinations of them, known as the mean and Gaussian curvatures, which are defined as the average and product of the principal curvatures:

$$H = \frac{1}{2}(c_1 + c_2), \tag{2.29}$$

$$K = c_1 c_2. \tag{2.30}$$

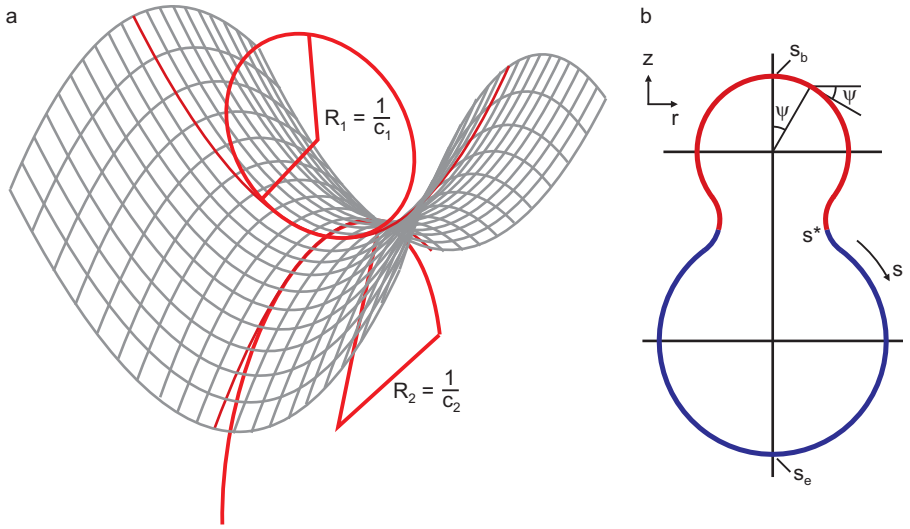

Figure 2.1: Curved surfaces. (a) A saddle point on a two-dimensional surface embedded in $\mathbb{R}^3$. The thick red lines indicate the principal directions. If the positive and negative curvatures are equal, the mean curvature at the saddle point is zero. If the surface extends to infinity, its Gaussian curvature is negative. (b) Coordinate system on an axisymmetric vesicle. The z-axis coincides with the axis of symmetry. The vesicle is parametrized using the arc length s along the contour. The radial coordinate r gives the distance from the symmetry axis and the coordinate z the distance along that axis. The shape of the vesicle be given as $r(z)$, $r(s)$, or in terms of the contact angle ψ of the contour as a function of either s or r. The geometric relations between r, z and ψ are given in equations (2.88) and (2.89).

Similar to the case of curves in $\mathbb{R}^2$, the principal curvatures c_1 and c_2 are the inverse of the radii of the osculating circles along their respective intersection curves. The definitions given in equations (2.29) and (2.30) are thus consistent with the intuitive, colloquial definitions of the previous section, but they are not easy to handle. Both in order to prove that H and K are indeed coordinate-independent, and for easier use in calculations involving the curvature energy later on, we will first formalize the definitions (2.29) and (2.30). In order to do that, we make use of the other, colloquial interpretation of curvature at the end of section 2.2.1. We choose a coordinate system on the embedding space $\mathbb{R}^3$ such that the origin is located at the point of interest $\vec{r}(x_1, x_2)$ and is a stationary point in the coordinates chosen. We can then express $\vec{r}(x_1, x_2)$ in the Monge gauge introduced at the end of section 2.3.1, and write $\vec{r}(x_1, x_2) = (x_1, x_2, z(x_1, x_2))$. Proceeding as before, we expand $z(x_1, x_2)$ around the minimum and find that the lowest-order term is quadratic in the coordinates:

$$z(x_1, x_2) - z_{\min} = \frac{1}{2}\vec{x}^T C \vec{x} + \text{h.o.t.} \tag{2.31}$$

where $\vec{x} = (x_1, x_2)^T$ and C is a symmetric matrix which is called the curvature matrix. Not surprisingly, we will find that c_1 and c_2 are the eigenvalues of C, and the corresponding eigenvectors are the principal directions.

Comparing equation (2.31) with the Taylor expansion of $z(x_1, x_2)$, we find for the coefficients of C ($i, j \in \{1, 2\}$):

$$C_{ij} = \frac{\partial^2 z(x_1, x_2)}{\partial x_i \partial x_j} = \frac{\partial^2 \vec{r}(x_1, x_2)}{\partial x_i \partial x_j} \cdot \hat{n}(x_1, x_2), \tag{2.32}$$

so the components of C are the projections of the second derivatives of $\vec{r}$ onto the surface normal $\hat{n}$. There are two (coordinate) invariants we can construct from the curvature matrix C: its trace and its determinant. They are directly related to the mean and Gaussian curvatures:

$$H = \frac{1}{2}\text{Tr}\, C = \frac{1}{2} g^{ij} C_{ij}, \tag{2.33}$$

$$K = \frac{\det C}{\det g}. \tag{2.34}$$

Here the g^{ij} are elements of the inverse of the metric tensor g and we once again sum over repeated indices.

It remains to show that the definitions (2.33) and (2.34) indeed are identical to the colloquial definitions (2.29) and (2.30) and that they are coordinate independent. To do so, we observe that since the matrix C is symmetric, it is diagonalizable by a orthonormal transformation T, $C = TDT^{-1}$, where $D = \text{diag}(d_1, d_2)$ with d_1 and d_2 the real eigenvalues of C. Moreover, if $d_1 \neq d_2$, then the corresponding eigenvectors are orthonormal, *i.e.*, they are unit vectors and perpendicular [38, Proposition 6.2]. If $d_1 = d_2$ then all directions are

principal directions, and we can choose any set of two orthonormal vectors that span the tangent plane. We denote these orthonormal vectors by $\hat{e}_1$ and $\hat{e}_2$ and, because D is just C expressed in the new basis $(\hat{e}_1, \hat{e}_2)$, we have

$$d_i = \big(\partial_i \hat{e}_i\big) \cdot \hat{n} \qquad (i = 1, 2), \tag{2.35}$$

where ∂_i as usual denotes the derivative along $\hat{e}_i$, and the unit vector $\hat{n}$ has not changed. In the new orthonormal basis, the metric is given by the identity matrix, so we find

$$H = \frac{1}{2}\big((\partial_1 \hat{e}_1) \cdot \hat{n} + (\partial_2 \hat{e}_2) \cdot \hat{n}\big). \tag{2.36}$$

Invoking equation (2.8) for the curvature of a line, this reduces to

$$H = \frac{1}{2}(\kappa_1 + \kappa_2) \tag{2.37}$$

with κ_i the curvature along $\hat{e}_i$. Since these were the principal directions, equation (2.37) is identical to equation (2.29).

There is an alternative expression for H in terms of the gradient of the surface normal, which immediately shows that it is coordinate-independent. Making use of the orthonormality of the basis $(\hat{e}_1, \hat{e}_2, \hat{n})$ and the Weingarten equations (2.55) derived in the next section, we can rewrite each of the terms of equation (2.36) in terms of derivatives of the unit normal:

$$(\partial_i \hat{e}_j) \cdot \hat{n} = \hat{e}_j \cdot -\partial_i \hat{n}. \tag{2.38}$$

For the mean curvature we then find:

$$H = -\frac{1}{2}\big(\hat{e}_1 \cdot \partial_1 \hat{n} + \hat{e}_2 \cdot \partial_2 \hat{n}\big) = -\frac{1}{2}\vec{\nabla} \cdot \hat{n}. \tag{2.39}$$

Equation (2.39) agrees with our intuitive understanding of curvature like equation (2.8) did: for a flat surface, the unit normal is constant and the mean curvature is zero. Once the surface gets bent, the unit normal changes and the absolute value of the mean curvature increases. Moreover, the expression given for H in equation (2.39) is indeed coordinate independent.

Relating the Gaussian curvature to the principle curvatures goes completely analogous to the mean curvature:

$$K = \frac{\det C}{\det g} = \frac{\det D}{1} = d_1 d_2 = \kappa_1 \kappa_2. \tag{2.40}$$

To show that the Gaussian curvature is coordinate independent, it is easiest to use the definition in terms of the ratio of determinants given by (2.34). Applying a coordinate transformation (2.25) which we again write in matrix form as X, we have $C = X^T \tilde{C} X$, $g = X^T \tilde{g} X$ and readily obtain:

$$K = \frac{\det C}{\det g} = \frac{\det(X^T \tilde{C} X)}{\det(X^T \tilde{g} X)} = \frac{\det X^T}{\det X^T} \frac{\det \tilde{C}}{\det \tilde{g}} \frac{\det X}{\det X} = \frac{\det \tilde{C}}{\det \tilde{g}}. \tag{2.41}$$

Alternatively, as we will see in section 2.3.4, the Gaussian curvature can be expressed as the inner product of the surface normal $\hat{n}$ with the curl of a vector field (equation (2.70), a form which is clearly coordinate independent.

2.3.3 Gauss's Theorema Egregium

The mean and Gaussian curvatures defined in the previous section are the invariants we will use to construct an energy functional for the membrane shape later on. To do so, there is no need to further develop the mathematical apparatus of surfaces. However, after we have defined that energy functional, we will make use of the Gauss-Bonnet theorem, which relates the integral of the Gaussian curvature to a topological boundary term, to simplify the expression significantly. In this section we will prove the earlier claim that the Gaussian curvature is an intrinsic property of the surface and in the next section we will derive the Gauss-Bonnet theorem. Before we can do that, we need to take a closer look at the metric and curvatures, and derive several useful identities. The proving technique for each of them is indicated here, but not always written out explicitly. For more details see *e.g.* Millman and Parker [33], Spivak [34] or Do Carmo [35].

In section 2.3.1, we defined the metric using the tangent vectors $\vec{e}_i$, which span the tangent plane $T_p\mathcal{M}$ to the point $p \in M$. We already used the metric to calculate the area of our manifold in equation (2.24), and here we will show that we can use it to calculate lengths and angles as well. Lines in the manifold have tangent vectors that lie in the tangent plane to the membrane at the point of interest. For an observer restricted to the manifold, components of vectors which lie along the manifold's surface normal $\hat{n}$ can not be measured, but components in the tangent plane can, because the manifold is locally flat. Quantities that can be expressed in terms of the tangent plane are therefore intrinsic to the manifold, the restricted observer can measure them without being aware of any embedding space. Due to the fact that the Gaussian curvature is intrinsic, this will allow the observer to determine that curvature from measurements that can be made within the manifold. To show that the earth is a sphere, it is therefore not necessary to go into space and take pictures from outside the manifold that is earth's surface; we could in principle prove this statement from ground measurements alone.

If we have a vector $\vec{v}$ tangent to $\mathcal{M}$ at p, we can express it in terms of the basis $(\vec{e}_1, \vec{e}_2)$ and write:

$$\vec{v} = v^i \vec{e}_i, \tag{2.42}$$

where once again we sum over repeated indices (which we continue to do throughout this chapter). The length of $\vec{v}$, and the angle θ between $\vec{v}$ and another vector $\vec{w} \in T_p\mathcal{M}$ can now be expressed in terms of the components of

the metric:

$$||\vec{v}||^2 = \vec{v}\cdot\vec{v} = v^i\vec{e}_i\cdot v^j\vec{e}_j = v^iv^jg_{ij} \tag{2.43}$$

$$||\vec{v}||\cdot||\vec{w}||\cos\theta = \vec{v}\cdot\vec{w} = v^iw^jg_{ij} \tag{2.44}$$

From measurements of lengths and angles of vectors within the manifold, we can determine the components of metric tensor g using equations (2.43) and (2.44). The metric is therefore an intrinsic property of the manifold, and any quantity that can be expressed in terms of the components of the metric is intrinsic as well.

In section 2.3.1 we introduced not only the metric, with components g_{ij}, but also its inverse, with components g^{ij}. The inverse metric has a geometrical interpretation of its own, due to the fact that there is an alternative way to define a basis for the tangent space $T_p\mathcal{M}$ at a point $p\in M$. We defined the basis vectors $\vec{e}_i$ as the derivatives of the manifold parametrization $\vec{r}(x_1,x_2)$ along the parameter x_i. We could equally well have taken the normals within $T_p\mathcal{M}$ to curves of constant x_i in the parametrization $\vec{r}(x_1,x_2)$ of $\mathcal{M}$. We choose the positive direction along that of increasing x_i, and denote these basis vectors by $\vec{e}^i$. By construction, we have

$$\vec{e}_1\cdot\vec{e}^2 = \vec{e}_2\cdot\vec{e}^1 = 0. \tag{2.45}$$

We now fix the length of the basis vectors $\vec{e}^i$ by imposing

$$\vec{e}_1\cdot\vec{e}^1 = \vec{e}_2\cdot\vec{e}^2 = 1. \tag{2.46}$$

Combining equations (2.45) and (2.46) we have $\vec{e}_i\cdot\vec{e}^j = \delta_i^j$. The metric with respect to the basis $(\vec{e}^1,\vec{e}^2)$ now has components $g^{ij} = \vec{e}^i\cdot\vec{e}^j$. To prove the claim that g^{ij} is the inverse of g_{ij}, we rewrite the vector $\vec{v}\in T_p\mathcal{M}$ of equation (2.42) in terms of the basis $(\vec{e}^1,\vec{e}^2)$:

$$\vec{v} = v_i\vec{e}^i. \tag{2.47}$$

The numbers v^i are called the contravariant components of $\vec{v}$ (with respect to the contravariant basis $(\vec{e}_1,\vec{e}_2)$) and the v_i are the covariant components (and $(\vec{e}^1,\vec{e}^2)$ the covariant basis). Analogously to (2.44) we can express the inner product of two vectors $\vec{v},\vec{w}\in T_p\mathcal{M}$ in terms of their covariant components and the covariant metric as $\vec{v}\cdot\vec{w} = g^{ij}v_iw_j$. Moreover, we can also mix the two bases and write

$$\vec{v}\cdot\vec{w} = v_i\vec{e}^i\cdot w^j\vec{e}_j = v_iw^j\delta_i^j = v_iw^j \tag{2.48}$$

so we now have four equivalent ways to write the inner product:

$$\vec{v}\cdot\vec{w} = g_{ij}v^iw^j = g^{ij}v_iw_j = v_iw^i = v^iw_i. \tag{2.49}$$

Equation (2.49) tells us that we can use g_{ij} and g^{ij} to translate between the two basis representations. Because $\vec{w}$ is arbitrary, we get from equality of respectively the second and fourth and third and fifth expressions in (2.49):

$$g_{ij}v^i = v_j \qquad \text{and} \qquad g^{ij}v_i = v^j \tag{2.50}$$

Colloquially we say that we can use the metric to raise and lower indices. Combining the two equalities in (2.50) we find for any vector $\vec{v} \in T_p\mathcal{M}$:

$$v_i = g_{ij}v^j = g_{ij}g^{jk}v_k \tag{2.51}$$

so by uniqueness of the representation of $\vec{v}$ in any basis

$$g_{ij}g^{jk} = \delta_i^k \tag{2.52}$$

and the metric of the contravariant and covariant representations are indeed each others inverse.

From the metric or first fundamental form, we now turn to the curvature matrix, which is also known as the second fundamental form or Weingarten map. Most differential geometry texts do not introduce it using the curvature of a paraboloid around a stationary point on the surface, but just define it using equation (2.32). This form is therefore a 2×2 matrix whose components are given by

$$L_{ij} = (\partial_i\vec{e}_j)\cdot\hat{n}, \tag{2.53}$$

where we follow convention and use the symbol L from now on. The components of the second fundamental form are thus the projections of the derivatives of the tangent vectors on the surface normals. Likewise, the Christoffel symbols are defined to be the projections on the surface tangents, and given by the equations

$$\partial_i\vec{e}_j = \Gamma_{ij}^k\vec{e}_k + L_{ij}\hat{n}. \tag{2.54}$$

Because $\hat{n}$ is a unit vector, we know that its derivative must be perpendicular to $\hat{n}$ (equation (2.9)). We can therefore write $\partial_i\hat{n}$ as a linear combination of the two tangent vectors. A straightforward calculation gives:

$$\partial_i\hat{n} = -L_{ij}g^{jk}\vec{e}_k. \tag{2.55}$$

Equations (2.55) are known as the Weingarten equations. We can use them to derive equation (2.38):

$$\begin{aligned}
\vec{e}_m\cdot\partial_i\hat{n} &= -L_{ij}g^{jk}\vec{e}_m\cdot\vec{e}_k \\
&= -L_{ij}g^{jk}g_{mk} \\
&= -L_{ij}\delta_m^j \\
&= -L_{im} \\
&= -(\partial_i\vec{e}_m)\cdot\hat{n}.
\end{aligned}$$

From equation (2.54) we can also find explicit expressions for the Christoffel symbols. By taking the dot product with $\vec{e}_l$ on both sides and subsequently multiplying with g^{lm} we find

$$\Gamma_{ij}^k = (\partial_i\vec{e}_j)\cdot\vec{e}_l g^{lk}. \tag{2.56}$$

Because $\partial_i \vec{e}_j = \frac{\partial^2 \vec{r}(x_1,x_2)}{\partial x_i \partial x_j} = \frac{\partial^2 \vec{r}(x_1,x_2)}{\partial x_j \partial x_i} = \partial_j \vec{e}_i$ we have $(\partial_i \vec{e}_j) \cdot \vec{e}_l = \frac{1}{2}\partial_i(\vec{e}_j \cdot \vec{e}_l)$ and by cyclically permutating indices in the last expression, we can rewrite Γ^k_{ij} as

$$\Gamma^k_{ij} = \frac{1}{2} g^{kl}(\partial_j g_{il} - \partial_l g_{ij} + \partial_i g_{lj}). \tag{2.57}$$

Equation (2.57) shows that the Christoffel symbols can be written in terms of the components of the metric tensors and its derivatives in the tangent plane. Hence the Christoffel symbols are intrinsic properties of the manifold.

Before we are ready to prove that the Gaussian curvature K is also intrinsic, we need one more mathematical object: the (Riemann) curvature tensor. It is defined in terms of the Christoffel symbols and thus reflects an intrinsic property of the manifold:

$$R^l_{ijk} = \partial_j \Gamma^l_{ik} - \partial_k \Gamma^l_{ij} + \Gamma^m_{ik}\Gamma^l_{mj} - \Gamma^n_{ij}\Gamma^l_{nk}. \tag{2.58}$$

Unlike the Christoffel symbols themselves, the Riemann tensor is an actual tensor, which means that under a change of coordinates it transforms as the four-parameter version of equation (2.25). We can express the Riemann curvature tensor in terms of the (extrinsic) components of the second fundamental form as

$$R^l_{ijk} = L_{ik}L_{jm}g^{ml} - L_{ij}L_{km}g^{ml}. \tag{2.59}$$

The 2^4 different equations expressed by (2.59) are known as Gauss's equations. The proof of (2.59) simultaneously provides us with another set of identities known as the Codazzi-Mainardi equations:

$$\partial_k L_{ij} - \partial_j L_{ik} = \Gamma^l_{ik}L_{jl} - \Gamma^l_{ij}L_{kl}. \tag{2.60}$$

The proof of equations (2.59) and (2.60) follows from the observation that

$$\partial_k(\partial_j \vec{e}_i) = \partial_j(\partial_k \vec{e}_i).$$

Expanding both sides using equations (2.54) and (2.55), we find that the tangential part of the resulting equality reproduces (2.59) and the normal component gives (2.60).

Gauss's equations allow us to express the Gaussian curvature

$$K = \det L / \det g$$

in terms of the Riemann curvature tensor. By equation (2.59) we have

$$g_{ln}R^l_{ijk} = (L_{ik}L_{jm}g^{ml} - L_{ij}L_{km}g^{ml})g_{ln} = L_{ik}L_{jn} - L_{ij}L_{kn}, \tag{2.61}$$

because $g^{ml}g_{ln} = \delta^m_n$. Now taking the special case that $i = k = 1, j = m = 2$, we find:

$$g_{l2}R^l_{121} = (L_{11}L_{22} - L_{12}L_{12}) = \det L = K \det g \tag{2.62}$$

so we can express K in terms of the intrinsic tensors R and g, which means that K itself is intrinsic. We have therefore proven what is known as Gauss's Theorema Egregium:

Theorem 2.1 (Theorema Egregium) *The Gaussian curvature K of a manifold $\mathcal{M}$ is an intrinsic property of that manifold.*

Theorem 2.1 tells us that we can measure the curvature of the manifold we live in without having to refer to a larger embedding space. That means we can establish the fact that the earth is an object with positive curvature without having to go to space - we could suffice with measuring the local metric coefficients. Similarly, the theory of general relativity uses this technique to determine the local curvature of the four-dimensional spacetime manifold on which the universe lives [39]. The fact that this is possible lead Gauss to label this theorem 'egregium', or remarkable. Originally, it was actually not this exact statement that Gauss called the theorema egregium, but an equivalent one, which relates the Gaussian curvature of two different surfaces if they are locally isometric.

Two two-dimensional manifolds (or surfaces) $\mathcal{M}$ and $\mathcal{N}$ are called isometric if there is an isometry between them. An isometry between $\mathcal{M}$ and $\mathcal{N}$ is a function $f : \mathcal{M} \to \mathcal{N}$ which is bijective, differentiable and preserves lengths, *i.e.*, for any curve $\gamma : [c,d] \subset \mathbb{R} \to \mathcal{M}$ the length of γ equals that of $f \circ \gamma$. The weaker condition that $\mathcal{M}$ and $\mathcal{N}$ are locally isometric is that for each point $p \in \mathcal{M}$ there exists an open subset $\mathcal{M}' \subset \mathcal{M}$ for which there is an isometry with an open subset $\mathcal{N}' \subset \mathcal{N}$. By considering the behavior of coordinate curves (curves obtained from a parametrization $\vec{r}(x_1, x_2)$ of $\mathcal{M}$ by keeping all except one of the coordinates fixed), it readily follows that if a local isometry exists, then the components of the metric in the open subsets $\mathcal{M}'$ and $\mathcal{N}'$ are identical (for a written out version of the proof of that statement, see [33, Proposition 10.5]). Because by Theorem 2.1 the Gaussian curvature K is completely determined by the components of the metric, we have the following corollary:

Corollary 2.2 *If two surfaces are locally isometric, then their Gaussian curvatures at corresponding points are equal.*

2.3.4 The Gauss-Bonnet Theorem

The Theorema Egregium tells us that the Gaussian curvature can be measured using only the intrinsic properties of the surface it is defined on. The Gauss-Bonnet theorem will give us an easy method to do just that. Moreover, it will relate two properties of the surface which do not seem to have any connection at all: its geometry and its topology. In fact, we will find that the integrated Gaussian curvature over a closed surface is a constant dependent only on the genus of the surface, and that the Gaussian curvature of a patch of surface is related to the in-surface (or geodesic) curvature of its boundary. Boundaries of patches of surfaces are curves in the embedding space $\mathbb{R}^3$, which we have already studied in section 2.2.2. For a curve constrained to a surface we can of

course use the properties of both, and will indeed do so. To avoid confusion, we need to distinguish between the basis vectors defined using the surface and those defined using the curve. We will keep the notation of this section and denote the basis vectors of the surface by $(\vec{e}_1, \vec{e}_2, \hat{n})$. The tangent, normal and binormal vectors defined on the three-dimensional space curve we will denote using capital letters: $(\hat{T}(s) = \hat{e}_s, \hat{N}(s), \hat{B}(s))$, where s is the arc length along the curve. By construction $\hat{T}$ is tangent to both the curve and the surface, but in general $\hat{N}$ and $\hat{B}$ have components both tangent and normal to the surface.

For simplicity we make a change of basis from $(\vec{e}_1, \vec{e}_2, \hat{n})$ to an orthonormal system, for example by taking by taking $\hat{e}_1 = \vec{e}_1/||\vec{e}_1||$ and $\hat{e}_2 = \frac{\vec{e}_2 - (\vec{e}_2 \cdot \hat{e}_1)\hat{e}_1}{||\vec{e}_2 - (\vec{e}_2 \cdot \hat{e}_1)\hat{e}_1||}$. We consider a curve γ on the surface $\mathcal{M} \subset \mathbb{R}^3$, and denote these basis vectors at the point $\gamma(s) = \vec{r}(x_1, x_2) \in \mathcal{M}$ by $(\hat{e}_1(s), \hat{e}_2(s), \hat{n}(s))$. Because the tangent vector $\hat{T}(s)$ to γ is tangent to $\mathcal{M}$ as well, we can write

$$\hat{T}(s) = \cos(\theta(s))\hat{e}_1(s) + \sin(\theta(s))\hat{e}_2(s). \tag{2.63}$$

As we travel along γ, the basis $(\hat{e}_1(s), \hat{e}_2(s), \hat{n}(s))$ changes orientation in space, and γ itself may change orientation within $\mathcal{M}$. Both effects are accounted for in equation (2.63), but it will be useful to separate the two. To do so, we consider a vector field $\vec{P}(s)$ defined on γ with the conditions that $\vec{P}(s)$ lies in the plane spanned by $(\hat{e}_1, \hat{e}_2)$ and all vectors $\vec{P}$ are parallel in the embedding space $\mathbb{R}^3$, or $d\vec{P}/ds = 0$. By expressing $\vec{P}$ in terms of $(\hat{e}_1, \hat{e}_2)$ like in equation (2.63), we will be able to determine the effect of the change of orientation of the basis alone. However, we first need to verify that such a vector field $\vec{P}$ indeed exists. A straightforward expansion of the condition $\frac{\mathrm{d}\vec{P}}{\mathrm{d}s} \cdot \hat{e}_j = 0$ in contravariant components P^k of $\vec{P}$ shows that they satisfy the coupled differential equations

$$\frac{\mathrm{d}P^k}{\mathrm{d}s} = -\Gamma^k_{ij} P^i \frac{\mathrm{d}\gamma^j}{\mathrm{d}s}. \tag{2.64}$$

By the Picard-Lindelöf Theorem (see *e.g.* [40]), the system of ordinary differential equations (2.64) has a unique solution for a given initial condition $\vec{P}(s = 0) = \vec{P}_0$, so the vector field we need does indeed exist. Using the fact that $s = s(\vec{x}) = s(x_1, x_2)$ and expressing $\vec{P}$ in the basis $(\hat{e}_1, \hat{e}_2)$, we have

$$\vec{P}(\vec{x}) = \cos(\theta_0(\vec{x}))\hat{e}_1(\vec{x}) + \sin(\theta_0(\vec{x}))\hat{e}_2(\vec{x}). \tag{2.65}$$

Taking derivatives of $\vec{P}$ along $\hat{e}_1$ and $\hat{e}_2$, we can relate variations of the basis to variations of θ_0:

$$\begin{aligned} 0 = \hat{e}_1(\vec{x}) \cdot \partial_i \vec{P}(\vec{x}) &= -\sin(\theta_0(\vec{x}))\big(\partial_i \theta_0(\vec{x}) - \hat{e}_1(\vec{x}) \cdot \partial_i \hat{e}_2(\vec{x})\big) && (2.66) \\ 0 = \hat{e}_2(\vec{x}) \cdot \partial_i \vec{P}(\vec{x}) &= \cos(\theta_0(\vec{x}))\big(\partial_i \theta_0(\vec{x}) + \hat{e}_2(\vec{x}) \cdot \partial_i \hat{e}_1(\vec{x})\big) \\ &= \cos(\theta_0(\vec{x}))\big(\partial_i \theta_0(\vec{x}) - \hat{e}_1(\vec{x}) \cdot \partial_i \hat{e}_2(\vec{x})\big) && (2.67) \end{aligned}$$

where we used the orthogonality of $\hat{e}_1$ and $\hat{e}_2$ in the final equality. We can combine equations (2.66) and (2.67) in a single expression:

$$\vec{\nabla}\theta_0(\vec{x}) = \hat{e}_1(\vec{x}) \cdot \vec{\nabla}\hat{e}_2(\vec{x}) \equiv \vec{\Omega}(\vec{x}), \tag{2.68}$$

where the vector field $\vec{\Omega}$ is known as the spin connection. Equation (2.68) tells us how the basis $(\hat{e}_1(s), \hat{e}_2(s))$ changes as we move along γ; to find the change of $\hat{T}$ due to changes in orientation of γ, we should look at the gradient of $\theta(\vec{x}) - \theta_0(\vec{x})$. The 'true change' in $\hat{T}$ is therefore given by the covariant derivative of $\theta(\vec{x})$:

$$\vec{D}\theta(\vec{x}) \equiv \vec{\nabla}\theta(x) - \vec{\Omega}(\vec{x}). \tag{2.69}$$

The spin connection $\vec{\Omega}$ is defined using gradients of the basis vectors $\hat{e}_i$. We encountered those before, in the definition of the Gaussian curvature K, using the determinant of the second fundamental form L. The components of that form were the projections of the derivatives of the basis vectors $\vec{e}_i$ on the surface normal $\hat{n}$. Not surprisingly, the spin connection and Gaussian curvature are related. Expanding the curl of $\vec{\Omega}$ and the determinant of L in components of the basis $(\hat{e}_1, \hat{e}_2, \hat{n})$, we readily obtain the identity [36]

$$K = \hat{n} \cdot (\vec{\nabla} \times \vec{\Omega}). \tag{2.70}$$

We are now ready to face the task set at the beginning of this section: the calculation of the integral of the Gaussian curvature over a surface patch $\mathcal{M}$ with boundary $\gamma = \partial\mathcal{M}$. As observed before, the tangent vector $\hat{T}(s)$ to γ is also tangent to $\mathcal{M}$, but the curve normal $\hat{N}(s)$ is not necessarily tangent to $\mathcal{M}$ as well. An observer living on the surface $\mathcal{M}$ can therefore not measure the curvature $\kappa(s)$ of γ, since by equation (2.8) that requires knowledge of the component of $\hat{N}$ normal to $\mathcal{M}$. However, the component of the curvature of γ in $\mathcal{M}$ can be measured. This component is known as the geodesic curvature[1] and is given by the projection of $\hat{T}'(s)$ on the tangent plane of $\mathcal{M}$:

$$\begin{aligned} \kappa_g(s) &= \hat{T}'(s) \cdot \big(\hat{n}(s) \times \hat{T}(s)\big) \\ &= \hat{n}(s) \cdot \big(\hat{T}(s) \times \hat{T}'(s)\big) \\ &= \partial_s\theta(s) - \hat{e}_1(s) \cdot \partial_s\hat{e}_2(s) \end{aligned} \tag{2.71}$$

where we expressed $\hat{T}$ in terms of the basis $(\hat{e}_1, \hat{e}_2)$ using (2.63) again. Rewriting equation (2.71) in terms of the parametrization (x_1, x_2), we find that we can express the geodesic curvature as the projection of the covariant derivative of θ on the tangent $\hat{T}$:

$$\kappa_g(s(\vec{x})) = \big(\vec{D}(\theta(\vec{x}))\big) \cdot \hat{T}(\vec{x}). \tag{2.72}$$

[1] The projection of $\hat{T}'(s)$ on $\hat{n}(s)$ is known as the normal curvature $\kappa_n(s)$, and the total curvature satisfies $\kappa^2 = \kappa_g^2 + \kappa_n^2$.

Using Stokes' Theorem to relate the surface integral over the curl of $\vec{\Omega}$ to the line integral over the surface boundary of Ω, we have:

$$\int_{\mathcal{M}} \left(\vec{\nabla} \times \vec{\Omega}(\vec{x})\right) \cdot \mathrm{d}\vec{S} = \oint_{\partial\mathcal{M}} \vec{\Omega}(\vec{x}) \cdot \mathrm{d}\vec{r}, \tag{2.73}$$

where $\mathrm{d}\vec{S} = \hat{n}\,\mathrm{d}S$ and $\mathrm{d}\vec{r} = \hat{T}\,\mathrm{d}s$. The surface integral over the Gaussian curvature K and the line integral over the geodesic curvature κ_g thus add up to a simple expression:

$$\begin{aligned} \int_{\mathcal{M}} K\,\mathrm{d}S + \oint_{\partial\mathcal{M}} \kappa_g(s)\,\mathrm{d}s &= \int_{\mathcal{M}} \vec{\nabla} \times \vec{\Omega}(\vec{x}) \cdot \mathrm{d}\vec{S} \\ &\qquad + \oint_{\partial\mathcal{M}} \left(\vec{\nabla}\theta(\vec{x}) - \vec{\Omega}(\vec{x})\right) \cdot \mathrm{d}\vec{r} \\ &= \oint_{\partial\mathcal{M}} \frac{\mathrm{d}\theta(s)}{\mathrm{d}s}\,\mathrm{d}s. \end{aligned} \tag{2.74}$$

If the boundary curve is smooth and does not intersect itself, it makes a single closed loop, and the tangent vector $\hat{T}$ rotates around the surface normal $\hat{n}$ exactly once, so the integral over $d\theta/ds$ equals 2π. There could be kinks in the boundary curve $\gamma = \partial\mathcal{M}$, in which case we get $2\pi - \sum_i(\pi - \Delta\theta_i)$, with $\Delta\theta_i$ the interior angle of the i^{th} kink. Equation (2.74) is known as the Gauss-Bonnet formula. It allows us to calculate the integral over K for a closed surface of any genus (*i.e.*, with any number of holes), by cutting it up into regular patches for which equation (2.74) holds. Using such a decomposition, it readily follows that for any region $\mathcal{R}$ on an oriented surface $\mathcal{M}$ the following theorem is true.

Theorem 2.3 (Gauss-Bonnet) *Let $\mathcal{R}$ be a region on an oriented surface $\mathcal{M} \subset \mathbb{R}^3$ with piecewise continuous boundary γ. Then*

$$\int_{\mathcal{R}} K\,\mathrm{d}S + \oint_{\gamma} \kappa_g\,\mathrm{d}s + \sum_i (\pi - \Delta\theta_i) = 2\pi\chi(\mathcal{R}), \tag{2.75}$$

where the $\Delta\theta_i$ are the interior angles of γ and $\chi(\mathcal{R})$ is the Euler characteristic of $\mathcal{R}$. In particular, for a closed compact surface $\mathcal{M}$ of genus g we have

$$\int_{\mathcal{M}} K\,\mathrm{d}S = 2\pi\chi = 4\pi(1-g). \tag{2.76}$$

The proof of Theorem 2.3 sketched here is from Kamien [36]. An alternative proof using geodesic coordinate patches can be found in Millman and Parker [33].

2.3.5 The Canham-Helfrich free energy functional

In this final section we return to the biological membrane and apply the results of this chapter to find a mathematical description for them. We derive

an expression for the energy of a membrane and evaluate it for a few special cases. We also give the general shape equation for a uniform membrane. For nonuniform membranes, we apply the formalism to find both the equations for uniform domains as well as their boundary conditions.

The Canham-Helfrich free energy functional describes the contribution to the total free energy of a membrane due to the curvature of that membrane. A special case was introduced by Canham in 1970 when studying the biconcave shape of red blood cells [41]. The general expression was given by Helfrich in 1973 [42]. Of course the curvature energy must be coordinate invariant, which means it must be expressed in terms of the principal curvatures introduced in section 2.3.2, or equivalently in terms of the mean H and Gaussian K curvatures. The Canham-Helfrich curvature energy contains all possible linear and quadratic terms in the principal curvatures, and is given by

$$\mathcal{E}_{\text{curv}} = \int_{\mathcal{M}} \left(\frac{\kappa}{2}(2H - C_0)^2 + \bar{\kappa} K \right) \mathrm{d}S. \tag{2.77}$$

Here the physical parameters κ and $\bar{\kappa}$ are the bending and Gaussian moduli respectively. For a biological or biomimetic membrane consisting of various types of lipids, they can be uniform throughout the membrane if the lipids are well mixed, but they can also vary if the lipids separate into domains. The parameter C_0 is the *spontaneous curvature*. The only term in (2.77) which is linear in the principle curvatures scales with C_0. The spontaneous curvature reflects the possibility of an asymmetry between the two leaflets of the membrane. For $C_0 = 0$, all terms in (2.77) are quadratic in the principal curvatures and the energy of a membrane patch is symmetric under reflections. Putting $C_0 \neq 0$ breaks this symmetry. We assume the spontaneous curvature to vanish in our description of the experiments involving phase separation in biomimetic vesicles, because there is no reason to assume an asymmetry between the leaflets is introduced when making these vesicles by means of electroformation (see appendix 4.A and [43] for details on the experimental procedures). Moreover, in the experiments we use the membrane leaflets have had ample time to relax any asymmetries that may still have formed by flipping lipids from one leaflet to the other. Finally, the descriptions of the membrane shapes we obtain with $C_0 = 0$ give accurate fits to the experimental data, confirming that assuming the spontaneous curvature to vanish in this case is justified. In contrast, when the membrane contains proteins which have a nonsymmetric (typically cone-like) shape, spontaneous curvature plays an important role and should be included.

For vanishing C_0, the Canham-Helfrich curvature energy (2.77) takes on the simple form

$$\mathcal{E}_{\text{curv}} = \int_{\mathcal{M}} \left(\frac{\kappa}{2}(2H)^2 + \bar{\kappa} K \right) \mathrm{d}S. \tag{2.78}$$

In the case of a uniform and closed membrane without holes (*i.e.*, with the topology of a sphere), like that of a red blood cell, the Gauss-Bonnet theorem

tells us that the integral over K is a constant, which we can simply subtract from the total energy. In many papers, including the original one by Canham, this term is therefore left out. For a membrane with piecewise constant composition (*i.e.*, with patches in which the physical parameters are uniform), the Gauss-Bonnet theorem tells us that the integral of K over such a uniform patch of membrane is related to a boundary term. Within the patch the only contribution to the curvature energy is therefore given by the mean curvature H.

Of course a membrane still has an area energy (2.28) like the soap films in section 2.3.1 did. We can consider the area energy from two viewpoints: either we take the total area of the membrane to be fixed (in which case we have a constraint on the shape, and the area energy $\mathcal{E}_{\text{area}}$ is constant) or we use the surface tension σ as a Lagrange multiplier for the membrane area $\mathcal{A}$. In the latter case, the total energy of a closed, single-component membrane without holes can be written as

$$\mathcal{E} = \mathcal{E}_{\text{curv}} + \mathcal{E}_{\text{area}} = \int_{\mathcal{M}} \left(\frac{\kappa}{2}(2H)^2 + \sigma \right) \mathrm{d}S, \tag{2.79}$$

where we have left out the constant contribution of the Gaussian curvature. The shape that minimizes (2.79) for a given membrane surface area $\mathcal{A}$ is the one that minimizes the overall mean curvature. It is a straightforward result that that shape is the most regular one possible, namely the sphere of radius $R = \sqrt{\mathcal{A}/4\pi}$. Interestingly, the curvature energy of such a sphere is independent of its radius:

$$\mathcal{E}_{\text{curv}} = \frac{\kappa}{2} \int_{\mathcal{M}} (2H)^2 \, \mathrm{d}S = \frac{\kappa}{2} \int_{\mathcal{M}} \left(\frac{1}{R} + \frac{1}{R} \right)^2 R^2 \, \mathrm{d}\Omega = 8\pi\kappa. \tag{2.80}$$

To get more interesting shapes, we should apply additional conditions. One such condition is to actively perturb the membrane by exerting a point force on a large spherical membrane vesicle. Experimental results show that applying such a force on a 'giant' unilamellar vesicle (or GUV, with a radius of $10-50\ \mu\mathrm{m}$) results in the extraction of a cylindrical membrane tube with uniform cross section [45]. In this case the total energy of the system is given by

$$\mathcal{E} = \int_{\mathcal{M}} \left(\frac{\kappa}{2}(2H)^2 + \sigma \right) \mathrm{d}S - fL, \tag{2.81}$$

where f is the applied force and L is the displacement of the point where the force is attached in the direction of that force. Specifically, for a cylindrical tube of radius R and length L equation (2.81) reads

$$\mathcal{E}_{\text{tube}} = \left(\frac{\kappa}{2} \frac{1}{R^2} + \sigma \right) 2\pi RL - fL. \tag{2.82}$$

Equation (2.82) shows a competition between two effects: the bending rigidity term tries to increase the tube radius, whereas the surface tension term tries to

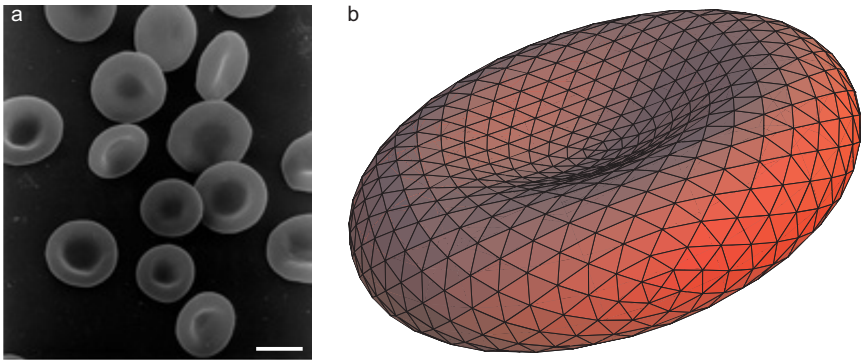

Figure 2.2: Shape of red blood cells. (a) Micrograph of human red blood cells, showing their distinct biconcave shape. Image courtesy of the National Institutes of Health (U.S.A.), scalebar $5\ \mu\mathrm{m}$. (b) Numerically obtained shape of a red blood cell, from the minimization of the bending energy (2.78), for a fixed enclosed volume and membrane area. The calculations were performed using the Surface Evolver software package by Brakke [44].

reduce it. A stable solution for an applied force f_0 can be obtained by choosing the proper radius R_0 such that the two effects exactly cancel. The values of f_0 and R_0 for given κ and σ are found from the stability condition that the derivatives of $\mathcal{E}_{\text{tube}}$ with respect to R and L should vanish. They give [46, 47]:

$$R_0 = \sqrt{\frac{\kappa}{2\sigma}}, \tag{2.83}$$

$$f_0 = 2\pi\sqrt{2\kappa\sigma}. \tag{2.84}$$

For typical values of $\kappa \approx 40\ \mathrm{pN\ nm}$ and $\sigma = 0.05\ \mathrm{pN/nm}$ we get $R_0 \approx 20\ \mathrm{nm}$ and $f_0 \approx 13\ \mathrm{pN}$. The tube radius is thus several orders of magnitude smaller than that of an experimental vesicle, which means that the implicit assumptions that any surface and volume constraints on the tube could be ignored, were justified. In chapter 7 we study such tubes as they are extracted not by an experimentally applied force, but by molecular motors.

An alternative additional condition is to fix the volume enclosed by the membrane. The sphere is the shape that encloses the maximal volume given its area; by forcing the volume to be less than that of a sphere we therefore create some 'excess area'. One particular such shape is the biconcave one of the red blood cell, where the enclosed volume is about half that of the sphere with the same area. Analytical expressions for such shapes are not easy to obtain, but numerically minimizing the curvature energy of a uniform closed membrane given an enclosed volume and total membrane area is a tractable task.

The software package Surface Evolver by Brakke [44] does just that. Figure 2.2 shows an example numerical result, where we begin with an arbitrary shape with the set amount of enclosed volume and surface area, and allow the curvature energy to relax. In our numerical calculations, independent of the original shape, we invariably retrieved the biconcave shape of the red blood cell.

In general, a differential equation for the mean curvature of a closed uniform vesicle with specified area and enclosed volume can be obtained through variation analysis. The energy is in this case given by the (mean) curvature energy with two Lagrange multiplier terms, one for the area (where the multiplier is the surface tension) and one for the volume (where the multiplier is the pressure difference across the membrane):

$$\mathcal{E} = \int_{\mathcal{M}} \left(\frac{\kappa}{2}(2H)^2 + \sigma \right) \mathrm{d}S + p \int \mathrm{d}V \tag{2.85}$$

The calculation of the first variation of this energy is lengthy but straightforward and was first performed by Ou-Yang and Helfrich [48]. The condition that this variation should vanish for an equilibrium shape results in the shape equation

$$p - 2\sigma H + 4\kappa H(H^2 - K) + 2\kappa \Delta H = 0, \tag{2.86}$$

where

$$\Delta = \frac{1}{\sqrt{\det g}} \partial_i \left(g^{ij} \sqrt{\det g} \partial_j \right) \tag{2.87}$$

is the Laplace-Beltrami differential operator on the membrane surface $\mathcal{M}$.

Equation (2.86) becomes a lot more tractable if we apply it to axisymmetric vesicles. Such vesicles are completely specified by giving the contour shape in a plane which contains the axis of rotation. Typically the axes of this plane are labelled r (horizontal) and z (vertical), where the z-axis is the axis of rotation. Because the contour is a curve in $\mathbb{R}^2$ we can parametrize it using the arc length along the contour from an arbitrary starting point, typically the topmost point of the contour. The coordinates $r(s)$ and $z(s)$ of any point on the contour are then related via the contact angle $\psi(s)$ on any point of the contour (see figure 2.1b):

$$\dot{r} = \frac{\mathrm{d}r}{\mathrm{d}s} = \cos\psi(s), \tag{2.88}$$

$$\dot{z} = \frac{\mathrm{d}z}{\mathrm{d}s} = -\sin\psi(s). \tag{2.89}$$

We can also express the mean and Gaussian curvatures and the Laplace-Bel-

trami operator in terms of $\psi(s)$ and $r(s)$:

$$H = -\frac{1}{2}\left(\dot{\psi} + \frac{\sin\psi(s)}{r(s)}\right) \tag{2.90}$$

$$K = \frac{\sin\psi(s)}{r(s)}\dot{\psi} \tag{2.91}$$

$$\Delta = \frac{\partial^2}{\partial s^2} + \frac{\dot{r}}{r}\frac{\partial}{\partial s} + \frac{1}{r^2}\frac{\partial^2}{\partial\phi^2} - \frac{\dot{r}}{r^3}\frac{\partial}{\partial\phi} \tag{2.92}$$

where ϕ is the polar angle, which runs from 0 to 2π. Substituting the axisymmetric expressions in the shape equation (2.86) we obtain the third-order differential equation for $\psi(s)$ [49]:

$$\begin{aligned}\dddot{\psi} = &-\frac{2\cos\psi}{r}\ddot{\psi} - \frac{1}{2}\dot{\psi}^3 + \frac{3\sin\psi}{2r}\dot{\psi}^2 + \frac{3\cos^2\psi - 1}{2r^2}\dot{\psi} \\ &+\frac{\sigma}{\kappa}\dot{\psi} - \frac{\cos^2\psi + 1}{2r^3}\sin\psi + \frac{\sigma}{\kappa}\frac{\sin\psi}{r} - \frac{p}{\kappa}.\end{aligned} \tag{2.93}$$

As was shown by Zheng and Liu [50], equation (2.93) can be written as a total derivative, which can be integrated to give an equivalent second order differential equation for $\psi(s)$:

$$\begin{aligned}\ddot{\psi}\cos\psi = &-\frac{1}{2}\sin\psi\dot{\psi}^2 - \frac{\cos^2\psi}{r}\dot{\psi} \\ &+\frac{\cos^2\psi + 1}{2r^2}\sin\psi + \frac{\sigma}{\kappa}\sin\psi - \frac{p}{\kappa}r.\end{aligned} \tag{2.94}$$

There is an alternative way of deriving the differential equations (2.93) and (2.94), by writing the energy (2.85) as an action, or an integral over a Lagrangian $\mathcal{L} = \mathcal{L}(\psi, \dot{\psi}, r, \dot{r}, z, \dot{z})$. This approach has the advantage that it gives us the proper differential equation for each axisymmetric patch of the vesicle surface, and also the conditions at their boundaries [51, 52]. For a patch that runs from $s = s_1$ to $s = s_2$ we have

$$\mathcal{E} = 2\pi\kappa\int_{s_1}^{s_2}\mathcal{L}\,\mathrm{d}s, \tag{2.95}$$

with

$$\begin{aligned}\mathcal{L} = &\frac{r}{2}\left(\dot{\psi} + \frac{\sin\psi}{r}\right)^2 + \frac{\sigma}{\kappa}r + \frac{p}{2\kappa}r^2\sin\psi \\ &+\gamma(\dot{r} - \cos\psi) + \eta(\dot{z} + \sin\psi).\end{aligned} \tag{2.96}$$

In equation (2.96) we used (2.90) to express H in terms of ψ and added two additional Lagrange multipliers γ and η to enforce the geometrical relations

(2.88) and (2.89). Variation of the functional $\mathcal{E}$ with respect to the variables ψ, r, z, γ and η gives their respective Euler-Lagrange equations, which for any variable x read

$$\frac{\mathrm{d}}{\mathrm{d}s}\frac{\partial \mathcal{L}}{\partial \dot{x}} - \frac{\partial \mathcal{L}}{\partial x} = 0. \tag{2.97}$$

From the variations with respect to the Lagrange multipliers γ and η we recover (2.88) and (2.89). The other three Euler-Lagrange equations give the following equations for the bulk of the patch:

$$\begin{aligned}
\ddot{\psi} &= \frac{\cos\psi\sin\psi}{r^2} - \frac{\cos\psi}{r}\dot{\psi} + \frac{p}{2\kappa}r\cos\psi \\
&\quad \frac{\gamma}{r}\sin\psi + \frac{\eta}{r}\cos\psi, && (2.98)\\
\dot{\gamma} &= \frac{1}{2}\dot{\psi}^2 - \frac{\sin^2\psi}{2r^2} + \frac{\sigma}{\kappa} + \frac{p}{\kappa}r\sin\psi, && (2.99)\\
\dot{\eta} &= 0. && (2.100)
\end{aligned}$$

There is an additional constraint which has to be taken into account, namely that the variation of $\mathcal{E}$ with respect to variations in the contour length, or equivalently the endpoints s_1 and s_2, should vanish. This condition is accounted for by demanding that the Hamiltonian $\mathcal{H}$ (defined below) should satisfy $\mathcal{H}(s_1) = \mathcal{H}(s_2) = 0$. Because the Lagrangian $\mathcal{L}$ does not depend directly on the arc length s, this implies that $\mathcal{H}$ should vanish everywhere. We therefore get an additional equation:

$$\begin{aligned}
\mathcal{H} &\equiv -\mathcal{L} + \dot{\psi}\frac{\partial \mathcal{L}}{\partial \dot{\psi}} + \dot{r}\frac{\partial \mathcal{L}}{\partial \dot{r}} + \dot{z}\frac{\partial \mathcal{L}}{\partial \dot{z}} \\
&= \frac{r}{2}\left[\dot{\psi}^2 - \left(\frac{\sin\psi}{r}\right)^2\right] - \frac{\sigma}{\kappa}r - \frac{p}{2\kappa}r^2\sin\psi \qquad (2.101)\\
&\quad +\gamma\cos\psi - \eta\sin\psi \\
&= 0.
\end{aligned}$$

We can combine equations (2.98, 2.99, 2.100) and (2.101) to reproduce equation (2.93). First we rewrite (2.101) to obtain η, which we substitute in (2.98) to get an expression for γ in terms of ψ. Differentiating that expression with respect to s and relating it to (2.99) we find (2.93).

A large part of this thesis is dedicated to vesicles with multiple domains. For such a vesicle, the energy given by equation (2.85) is incorrect, since it ignores the Gaussian curvature, which by the Gauss-Bonnet theorem will give a contribution at the domain boundary. The description of a phase separated (*i.e.*, containing multiple domains) vesicle is therefore more difficult but also more interesting than that of a uniform vesicle. Moreover, as we study in detail in chapter 3, phase separation into domains within the lipid membrane results

in a line tension on the boundaries of those domains. We therefore add an additional energy term which penalizes domain boundaries. The total energy of an axisymmetric vesicle with two domains is then given by

$$\mathcal{E} = \sum_{i=1}^{2} \int_{\mathcal{M}_i} \left(\frac{\kappa_i}{2}(2H)^2 + \bar{\kappa}_i K + \sigma_i \right) \mathrm{d}S + p \int \mathrm{d}V + \tau \oint_{\partial \mathcal{M}} \mathrm{d}l, \tag{2.102}$$

where the line tension τ on the boundary line between $\mathcal{M}_1$ and $\mathcal{M}_2$ plays a role similar to that of the surface tension σ on the membrane area. Together, $\mathcal{M}_1$ and $\mathcal{M}_2$ still form a closed surface. If we locate the boundary at $s = 0$, the energy of each of the bulk parts is given by equation (2.95), but we get additional contributions at the boundary due to the presence of a line tension and a difference in Gaussian modulus. Using the Lagrangian formulation and translating the Gaussian modulus term into a constant contribution (which we ignore) plus a boundary term, we find

$$\mathcal{E} = 2\pi \left[\kappa_1 \int_{-s_b}^{0} \mathcal{L}_1 \, \mathrm{d}s + \kappa_2 \int_{0}^{s_e} \mathcal{L}_2 \, \mathrm{d}s + \tau r_0 + \Delta\bar{\kappa} \cos\psi_0 \right]. \tag{2.103}$$

Here r_0 and ψ_0 are the vesicle radius and tangent angle at the domain boundary ($s = 0$) respectively, $\Delta\bar{\kappa} = \bar{\kappa}_2 - \bar{\kappa}_1$ and the two domains run over $(-s_b, 0)$ and $(0, s_e)$. Colloquially we can refer to the domain boundary as the vesicle's equator and the extrema (at $s = -s_b$ and $s = s_e$) as its poles. The differential equation describing the vesicle shape in each of the bulk domains is still given by (2.94), as follows again readily from the Euler-Lagrange equations. Variation of the free energy (2.103) also gives us the boundary conditions at the domain boundary. By stationarity of $\mathcal{E}$ with respect to variations in r_0 and ψ_0 we obtain the conditions [52]:

$$\lim_{\varepsilon \downarrow 0} \frac{\partial \mathcal{L}_2}{\partial r}(\varepsilon) - \lim_{\varepsilon \uparrow 0} \frac{\partial \mathcal{L}_1}{\partial r}(\varepsilon) = \tau, \tag{2.104}$$

$$\lim_{\varepsilon \downarrow 0} \frac{\partial \mathcal{L}_2}{\partial \psi}(\varepsilon) - \lim_{\varepsilon \uparrow 0} \frac{\partial \mathcal{L}_1}{\partial \psi}(\varepsilon) = -\Delta\bar{\kappa} \sin\psi_0, \tag{2.105}$$

which translate into

$$\lim_{\varepsilon \downarrow 0} (\gamma(\varepsilon) - \gamma(-\varepsilon)) = \tau, \tag{2.106}$$

$$\lim_{\varepsilon \downarrow 0} (\kappa_2 \dot{\psi}(\varepsilon) - \kappa_1 \dot{\psi}(-\varepsilon)) = -(\Delta\kappa + \Delta\bar{\kappa}) \frac{\sin\psi_0}{r_0}, \tag{2.107}$$

where $\Delta\kappa = \kappa_2 - \kappa_1$. The boundary condition (2.106) combines with equation (2.98) to give a condition on the second derivative of ψ:

$$\lim_{\varepsilon \downarrow 0} \left(\kappa_2 \ddot{\psi}(\varepsilon) - \kappa_1 \ddot{\psi}(-\varepsilon) \right) = \left(2\Delta\kappa + \Delta\bar{\kappa} \right) \frac{\cos\psi_0 \sin\psi_0}{r_0^2} + \frac{\sin\psi_0}{r_0} \tau. \tag{2.108}$$

Alternatively, these boundary conditions can be derived by considering force and torque balance [53]. Equations (2.107) and (2.108) tell us that there can be discontinuities in $\ddot{\psi}$ and even $\dot{\psi}$ at a membrane domain boundary if there is a line tension τ between the domains or the bending or Gaussian moduli are not equal in the different domains. These boundary conditions will play a vital role in determining the shape of completely phase-separated membrane vesicles in chapter 4. Their influence on the vesicle shape will provide us with a tool with which we can measure the physical parameters τ and $\Delta\bar{\kappa}$.

Apart from the possibly discontinuous boundary conditions on $\dot{\psi}$ and $\ddot{\psi}$, there are also conditions on $r(s^*)$ and $\psi(s^*)$. Both should be continuous. If $r(s)$ is not continuous at s^* there is a hole in the membrane; if $\psi(s)$ is not continuous there is a sharp kink which carries infinite curvature and therefore infinite energy.

CHAPTER 3

GIBBS PHASE DIAGRAMS OF TERNARY SYSTEMS

In this chapter we study the phase diagrams of ternary lipid mixtures. In particular we focus on the mixture of cholesterol, a saturated lipid and an unsaturated one. The phase diagram of such a lipid mixture exhibits a rich phase behavior with multiple phase coexistence regimes. Remarkably, phase separation even occurs when each of the three binary systems consisting of two of the three components is a uniform mixture. In the model we present here, we interpret the phase separation of the ternary system as a consequence of an interaction between all three components. For vanishing values of any of the three concentrations, the model reduces to the well-known Flory-Huggins model that describes the phase behavior of a binary system. From the associated Gibbs free energy we calculate phase diagrams, spinodals and critical points. Moreover, we use a Van der Waals / Cahn-Hilliard like construction to derive an expression for the line tension between coexisting phases. We show how the line tension depends on the position in the phase diagram, and give an explicit expression for the concentration profile at the phase boundary.

3.1 Introduction

Like any large collection of particles, lipids in a bilayer membrane have different levels of ordering dependent on thermodynamic parameters such as the temperature, and hence exhibit different phases. These phases are not only a function of thermodynamic variables such as the temperature, but also of the amount of ordering in the system. As introduced in section 1.2, the most common phases in which lipids can exist are a liquid-ordered (L_o), a liquid-disordered (L_d), and a gel phase. A membrane vesicle can have a uniform phase, but also exhibit coexistence of multiple phases, dependent on its lipid composition. In this chapter we introduce and review phase coexistence in lipid membranes with multiple components. We focus in particular on ternary membranes, which are the main subject of chapters 4, 5 and 6. In recent years, the phase diagrams of several ternary lipid systems have been determined experimentally [54, 55]. We use a simple extension of the Flory-Huggins model, which describes binary systems, to give a qualitative description of the different phase diagrams found in ternary lipid systems. Using the expression for the Gibbs free energy of this model, we can use a Van der Waals / Cahn-Hilliard like construction to derive an expression for the line tension between coexisting lipid phases as a function of membrane composition. This construction allows us to link experimental results on the phase diagrams to experimentally determined values of the line tension, and get new insights into how those two properties of the membrane are related to each other. Moreover, the line tension plays a critical role in the following chapters, as it is a key factor in determining the overall membrane shape.

3.1.1 Phase coexistence and the Gibbs phase triangle

In general, a phase diagram shows the conditions at which thermodynamically-distinct phases can occur at equilibrium, as a function of certain macroscopic variables like temperature, pressure, and composition. For a simple, one-component system, any point in a (p, T) phase diagram corresponds to a possible realization, and setting the pressure and temperature we obtain a uniform state for the entire system. Already for a bicomponent system this no longer needs to be the case, and apart from uniform phases we can also get coexistence of two distinct thermodynamic phases. The maximum number of phases P that can coexist in a given system is determined by the Gibbs phase rule [56, Chapter 9]

$$P = C - F + 2. \tag{3.1}$$

Here C is the number of components and F denotes the number of degrees of freedom, *i.e.*, the number of intensive variables which are independent of other intensive variables. For a two-component system in which temperature and pressure are the independent variables, two-phase coexistence is al-

lowed by equation (3.1). Figure 3.1 shows some schematic phase diagrams for a binary system as a function of the molar fraction x of one of the components and temperature, for a given pressure (please note that the complete phase diagrams are three-dimensional, with the pressure on the third axis, and the two-dimensional figures shown are slices through this complete diagram). Quenching the system below the phase boundary produces phase coexistence. For two thermodynamically different phases to coexist within one system, the values of the intrinsic variables must be equal. Here these are the temperature T, pressure p and the chemical potentials μ_A and μ_B of the two components A and B. Therefore the tie lines, which connect the two coexisting phases in the phase diagram, are in the plane of the figure (same pressure) and horizontal (same temperature) in figure 3.1.

The proper thermodynamic potential to use for describing this system is the Gibbs free energy $\mathcal{G}$, which has p, T and μ as its independent variables, and is given by

$$\mathcal{G} = E - TS + pV. \tag{3.2}$$

If we know $\mathcal{G}$ for our binary system, we can find the phase boundary by the condition that the chemical potentials must be equal in the coexisting phases. They are given as derivatives of $\mathcal{G}$ with respect to the number N_i of particles of type i (with $N_1 = xN$, $N_2 = (1-x)N$ and N the total number of particles in the system):

$$\mu_1 = \left(\frac{\partial \mathcal{G}}{\partial N_1}\right)_{p,T,N_2}, \qquad \mu_2 = \left(\frac{\partial \mathcal{G}}{\partial N_2}\right)_{p,T,N_1}. \tag{3.3}$$

The Flory-Huggins model (section 3.1.2) gives a phenomenological expression for $\mathcal{G}(p,T,x)$ of a binary system which consists of a mixture of two polymers.

In the case of ternary systems, the Gibbs phase rule allows for coexistence of up to three different phases. Drawing the full phase diagram as a function of the two independent molar fractions, temperature and pressure would require four dimensions, limiting us to two- and three-dimensional slices. Two-dimensional slices for which both the temperature and pressure are given are known as Gibbs triangles. In these, each of the corners of the equilateral triangle corresponds to a system consisting solely of the associated component, the sides correspond to binary systems and the interior points to ternary systems. Because in an equilateral triangle the sum of the distances from any interior point to the three sides is equal, any point uniquely corresponds to a composition given by three molar fractions x, y and z, which sum to unity, see figure 3.2.

3.1.2 The Flory-Huggins model for a bicomponent system

Flory-Huggins theory is a mean-field, phenomenological model which describes the mixing properties of a system containing two types of polymers. Here we give a short sketch of the 2-component theory, where we assume that the

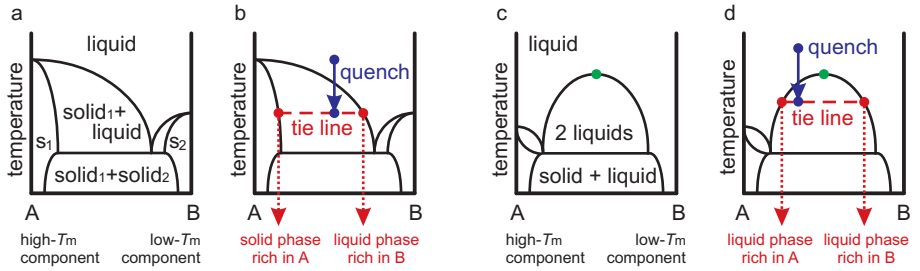

Figure 3.1: Schematic two-component phase diagrams, in terms of molar fraction x of component A and temperature T, for a given pressure. For high temperature, the system is in a uniform state. When we quench the system below the phase boundary (blue arrow) we obtain a system which exhibits coexistence of two thermodynamically different phases at the same temperature and pressure, but different compositions. The two coexisting phases are found at the intersections of the tie line with the phase boundary. Figures (a) and (b) show the situation in case we have coexistence of a solid and a liquid phase. Figures (c) and (d) show the coexistence of two liquid phases, which has a critical point (green dot).

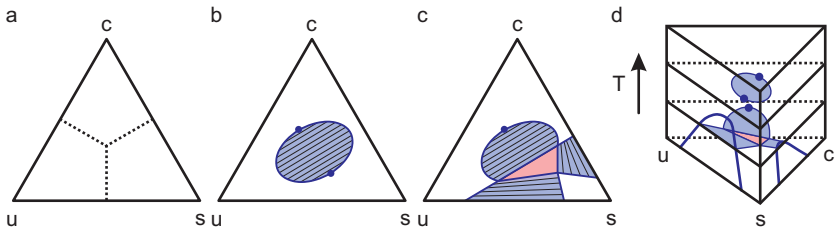

Figure 3.2: Gibbs phase triangle for a ternary system. The triangle represents a slice through the phase diagram at a given pressure and temperature. (a) The sum of the distances from any point in the equilateral triangle to the three edges equals 1. Every point in the Gibbs triangle corresponds to a composition of the ternary system with the concentrations corresponding to these distances to the edges. (b) Example of a phase diagram with a closed-loop miscibility gap. The two-phase coexistence region in the center has two critical points (blue dots). (c) Example of a phase diagram with multiple two-phase (blue) and a single three-phase (pink) coexistence regimes. (d) Possible Gibbs prism combining several Gibbs triangles.

monomers of the two species considered are equal in size. A more complete introduction can be found in many textbooks, *e.g.* Strobl [57, Chapter 3].

Suppose we prepare a system of polymers of type A and B such that the two are initially completely demixed and therefore effectively contained in separate volumes V_A and V_B. In the Flory-Huggins model, there are two contributions to the change in Gibbs free energy due to the mixing of this system. The first is an increase in entropy due to the larger total volume available to a single monomer of either type. The second contribution is due to individual monomer-monomer interactions. For uncharged monomers, the dominant interaction is Van der Waals attraction. Typically equal monomers will attract each other more strongly than unequal ones, in which case the second contribution to the free energy will oppose mixing.

The change in translational entropy is given by

$$\Delta\mathcal{S} = k_{\text{B}}\left[N_A \log\frac{N}{N_A} + N_B \log\frac{N}{N_B}\right] = -k_{\text{B}}N\left[x\log x + y\log y\right]. \tag{3.4}$$

Here $x = N_A/N$ and $y = N_B/N$ are the number fractions of species A and B respectively, $N = N_A + N_B$ is the total number of monomers, and k_{B} Boltzmann's constant. Because of the assumption that the monomers are equal in size, x and y are also the volume fractions of species A and B.

In a mean-field approach, the probability that a monomer of species A gets located next to one of species B is given by the product xy. We associate a free energy penalty $\chi k_{\text{B}}T$ to such a configuration and write for the monomer-monomer interaction contribution to the Gibbs free energy:

$$\Delta\mathcal{G}_{\text{loc}} = k_{\text{B}}T\chi N x y. \tag{3.5}$$

A negative value of the dimensionless Flory-Huggins parameter χ corresponds to an attractive interaction between monomers of species A and B and drives mixing, while a positive value of χ, which is the typical case, opposes it.

The total change in Gibbs free energy due to mixing is given by

$$\mathcal{G} = -T\Delta\mathcal{S} + \Delta\mathcal{G}_{\text{loc}} = k_{\text{B}}TN\left[x\log x + y\log y + \chi x y\right]. \tag{3.6}$$

Moreover, by construction, x and y add up to unity

$$x + y = 1, \tag{3.7}$$

which leaves us with a single-parameter minimization problem. In figure 3.3 we plot $\mathcal{G}$ as a function of x for different values of χ.

From figure 3.3 it is clear that there are two possible scenarios. For small values of χ, $\mathcal{G}$ has a single minimum and the system mixes for all values of x, the single freely adjustable parameter. For larger values of χ, $\mathcal{G}$ has two minima, and although it can still be negative for all values of x, we do not get complete mixing in all cases. This is due to the fact that the system can reduce its Gibbs

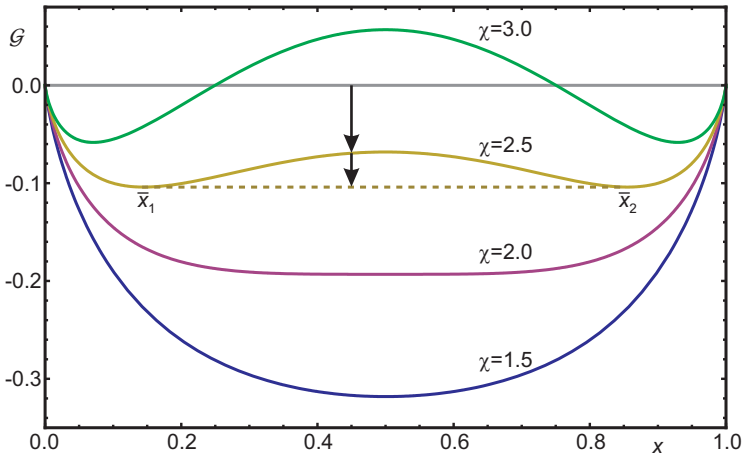

Figure 3.3: Change in Gibbs free energy due to mixing for various values of the Flory-Huggins parameter χ. For $\chi > \chi_{\text{crit}} = 2.0$, a miscibility gap opens: the free energy can be lowered by demixing, as illustrated by the two arrows for $\chi = 2.5$.

free energy with respect to the uniform mixture (corresponding to the local maximum) by segregating into two partially mixed fractions, corresponding to the two minima. This process is represented by the two arrows in figure 3.3 at $x = 0.45$ and $\chi = 2.5$. The long arrow, going down from $\mathcal{G} = 0$ to the graph of $\mathcal{G}$, represents the free energy gained by mixing the system. The short arrow going down from the graph to the line connecting the two minima, represents the additional free energy gain by segregating the system into domains with fractions $\bar{x}_1$ and $\bar{x}_2$ of species A. This process will occur for any initial value of x between $\bar{x}_1$ and $\bar{x}_2$. This region is called the miscibility gap and its extremal values $\bar{x}_1$ and $\bar{x}_2$ are found by equating the chemical potentials (see section 3.2).

The critical value χ_c of the Flory-Huggins parameter, which determines whether or not the system mixes, is given by the point at which the curvature of $\mathcal{G}$ vanishes at $x = 0.5$ (see section 3.2). A straightforward calculation shows that this condition holds for $\chi_c = 2$.

3.1.3 Ternary systems

In a ternary system, we have $C = 3$ and $F = 2$ (temperature and pressure) and hence the Gibbs phase rule (3.1) gives $P = 3$, so we can have up to three coexisting phases. In recent years several experimentally determined Gibbs phase triangles for ternary systems have been published, showing two- and three-phase coexistence regions [54]. As introduced in section 1.2, the three

phases that can coexist in ternary lipid membranes are two liquid phases (L_o and L_d) and a gel phase. Remarkably, there are also ternary systems for which each of the three limit binary systems is completely mixed, but for which the ternary system shows a two-phase coexistence region [55]. The boundary of the coexistence region in such a system is a closed loop inside the Gibbs phase triangle. Since phase coexistence is understood to be a consequence of what is known as a miscibility gap (as explained in section 3.1.2), such phase diagrams are said to contain a closed-loop miscibility gap.

A number of models for ternary lipid systems have been proposed by several groups in recent years. In a 2004 paper, Komura *et al.* [58] combined a Flory-Huggins like approach for liquid-liquid phase coexistence with an order parameter description for the liquid-gel phase transition and presented phase diagrams for two of the three limiting binary systems of the ternary system considered here. In a follow-up paper in 2005 [59] they extend this model to the ternary system, introducing three independent Flory-Huggins parameters for the three binary interactions and keeping the order parameter description for the gel phase. This model allows for a qualitative description of some of the experimentally observed phase diagrams, but fails to reproduce the one with the closed-loop miscibility gap. In an alternative approach, Radhakrishnan and McConnell [60] and McConnell [61] proposed a model in which two of the three components form a complex which interacts with the third component. The resulting phase diagram has some qualitative features which also appear in the closed-loop experimental one of Veatch *et al.* [55], but does not allow for three coexisting phases. Recently Putzel and Schick [62] presented a refined version of the model of Komura *et al.* They use two different models for the system with a closed-loop miscibility gap and the three-phase coexistence region, both depending on a combination of a Flory-Huggins model and an order-parameter description. Using these models, Putzel and Schick also studied the effect crosslinking molecules have on the phase diagram [63].

In section 3.3 we present a model for the ternary system based solely on an extension of the Flory-Huggins model of the binary system, and reducing to the binary models in each of the limit cases. In this model, we supplement the binary interactions with an interaction between all three components. This approach to model a ternary system is well known in the fields of alloys and of polymer mixtures [64–68], but thus far has not been applied to lipid mixtures. We show that the extension with a ternary term is necessary to explain the phase triangle with a closed-loop miscibility gap found experimentally by Veatch *et al.* [55] when the binary interactions are repulsive. The model can also reproduce the phase triangle with coexisting liquid and gel phases, as well as a three-phase coexistence region. We use our model to determine the linear stability of the system and explicitly find the critical points. Using the expression for the Gibbs free energy given by our model, we can calculate the energy associated with a boundary between two coexisting phases as a function of membrane composition (section 3.4). This boundary energy is a line ten-

sion in two-dimensional lipid membranes, and a key factor for determining the membrane shape [6, 10, 69–71].

3.2 Thermodynamics of mixtures

The appropriate characteristic function for describing phase equilibria in mixtures is the Gibbs free energy, which is a function of the particle numbers N_i, pressure p and temperature T

$$\mathcal{G} = \mathcal{G}(N_1, \ldots, N_n, p, T). \tag{3.8}$$

The requirement for two phases to coexist is that all chemical potentials are equal in both phases, as well as the temperature and pressure (which is why $\mathcal{G}$ is such a useful function for mixtures). The chemical potentials associated with each of the components are given by:

$$\mu_i = \frac{\partial \mathcal{G}}{\partial N_i}, \tag{3.9}$$

where the partial derivatives are taken with all the other variables constant. The total number of particles $N = N_1 + \cdots + N_n$ is constant and taken as the extensive variable, and we define

$$\mathcal{G}/N = g(x_1, \ldots, x_n) \quad \text{with} \quad x_i = N_i/N. \tag{3.10}$$

The number fractions x_i have a redundancy, and obey the condition

$$x_1 + \cdots + x_n = 1, \tag{3.11}$$

which will allow us to eliminate one of them below. We can write the chemical potentials explicitly as functions of g and its derivatives to the x_i's, showing that they are intensive

$$\mu_i = g + \frac{\partial g}{\partial x_i} - \sum_{j=1}^{n} x_j \frac{\partial g}{\partial x_j}. \tag{3.12}$$

These derivatives are unrestricted, in the sense that only the other particle numbers N_k are kept fixed, not *e.g.* the total particle number N. Summing all the μ_i's, we find that we also have the relation

$$g = \sum_{i=1}^{n} x_i \, \mu_i. \tag{3.13}$$

Because our system is restricted to the subspace defined by equation (3.11), we can eliminate one of the number fractions (which we take to be x_n) from

the problem. Within this subspace, equation (3.12) reads

$$\mu_i = g + \frac{\partial g}{\partial x_i} - \sum_{j=1}^{n-1} x_j \frac{\partial g}{\partial x_j} \qquad i = 1, \ldots, n-1 \tag{3.14}$$

$$\mu_n = g - \sum_{j=1}^{n-1} x_j \frac{\partial g}{\partial x_j} \tag{3.15}$$

where g and its derivatives are now functions of $x_1, \ldots, x_{n-1}$.

The formalism given above applies to a system with any number of components. For simplicity we will restrict ourselves to ternary systems below. We will indicate the concentrations of the three components by x, y and z instead of x_1, x_2 and x_3. In order to have phase coexistence the chemical potentials of all three components must be equal in both phases. In our ternary system we find that phases with number fractions $(\bar{x}_1, \bar{y}_1)$ and $(\bar{x}_2, \bar{y}_2)$ can coexist if

$$\begin{aligned} \mu_1(\bar{x}_1, \bar{y}_1) &= \mu_1(\bar{x}_2, \bar{y}_2), \\ \mu_2(\bar{x}_1, \bar{y}_1) &= \mu_2(\bar{x}_2, \bar{y}_2), \\ \mu_3(\bar{x}_1, \bar{y}_1) &= \mu_3(\bar{x}_2, \bar{y}_2). \end{aligned} \tag{3.16}$$

The system (3.16) gives us three equations for the four unknowns ($\bar{x}_1$, $\bar{y}_1$, $\bar{x}_2$, $\bar{y}_2$), which means that in the Gibbs phase triangle there can be a coexistence region, in accordance with the Gibbs phase rule (3.1). The boundary of the phase coexistence regime (which consists of pairs of points that satisfy (3.16)) is called the binodal. The phase coexistence region is thus an open subset of the Gibbs phase triangle. Any point inside this region is connected to two points on the binodal by a tie line. A system prepared in a composition corresponding to such a point will demix into two phases corresponding to the two endpoints of the tie line it lies on. If the binodal forms a closed loop, the system has a closed-loop miscibility gap.

Using the identities (3.14, 3.15), we find that there is an equivalent system of conditions for phase coexistence given by

$$\begin{aligned} g_x(\bar{x}_1, \bar{y}_1) &= g_x(\bar{x}_2, \bar{y}_2), \\ g_y(\bar{x}_1, \bar{y}_1) &= g_y(\bar{x}_2, \bar{y}_2), \\ g(\bar{x}_1, \bar{y}_1) - \bar{x}_1 g_x(\bar{x}_1, \bar{y}_1) - \bar{y}_1 g_y(\bar{x}_1, \bar{y}_1) &= g(\bar{x}_2, \bar{y}_2) - \bar{x}_2 g_x(\bar{x}_2, \bar{y}_2) - \bar{y}_2 g_y(\bar{x}_2, \bar{y}_2), \end{aligned} \tag{3.17}$$

where subscripts x and y on $g(x, y)$ denote derivatives with respect to x and y. The first equation of (3.17) is found by subtracting μ_3 from μ_1, the second by subtracting μ_3 from μ_2 and the third is identical to the third of (3.16).

The binodal separates the region in the phase diagrams in which our system is in a homogeneous phase from those in which it separates into two or three coexisting phases. However, in this simple Van der Waals type of phase

coexistence, the appearance of an unstable regime in the Gibbs phase triangle is a prerequisite. We therefore study the linear stability of our system at such a point (x, y) in a ternary system. We can vary both number fractions independently, and find for the variation in Gibbs free energy per particle

$$\delta g = \frac{1}{2}(\delta x, \delta y) \begin{pmatrix} g_{xx} & g_{xy} \\ g_{xy} & g_{yy} \end{pmatrix} \begin{pmatrix} \delta x \\ \delta y \end{pmatrix} + \mathcal{O}(3) \tag{3.18}$$

where $\mathcal{O}(3)$ refers to third order terms in δx and δy. For the second order term in (3.18) to vanish the determinant of the matrix (g_{ij}) of second order derivatives of g must be equal to zero. This condition also holds for systems with more than three components, and in general we find that the system becomes linearly unstable when

$$\det(g_{ij}) = 0. \tag{3.19}$$

We call the set of solutions of (3.19) the spinodal, because it marks the boundary between two types of demixing. Linearly stable systems demix by nucleation and growth and linearly unstable ones by spinodal decomposition [57, 72]. They are qualitatively different: in the case of nucleation and growth there is a nucleation barrier for the system to overcome before phase separation can take place, which is absent in the case of spinodal decomposition. Binary polymer systems, described by similar two-component Flory-Huggins models, also exhibit distinctly different patterning in the binodal (nucleated) and spinodal regimes [57, Chapter 3].

Equation (3.19) is equivalent with the condition that (g_{ij}) must have a zero eigenvalue, and if (3.19) holds the eigenvalue equation

$$\sum_{j=1}^{2} g_{ij}\, r_j = 0, \tag{3.20}$$

has a solution in spinodal points. The eigenvector $\vec{r} = (r_1, r_2)$, belonging to the eigenvalue 0, is a direction in which all the thermodynamic potentials are stationary. To prove this statement, we consider a small displacement $(dx, dy) = (r_1, r_2)ds$ along $\vec{r}$ from a point on the spinodal. Taking the derivative of the chemical potential μ_i along $\vec{r}$ we find

$$\begin{aligned} \frac{\partial \mu_i}{\partial s} &= \frac{\partial \mu_i}{\partial x}\frac{\partial x}{\partial s} + \frac{\partial \mu_i}{\partial y}\frac{\partial y}{\partial s} \\ &= (g_{i1} - x g_{11} - y g_{21}) r_1 + (g_{i2} - x g_{12} - y g_{22}) r_2 \\ &= (g_{i1} r_1 + g_{i2} r_2) - (g_{11} r_1 + g_{12} r_2) x - (g_{21} r_1 + g_{22} r_2) y \\ &= 0 \end{aligned} \tag{3.21}$$

where the expressions in brackets in the third line of (3.21) all vanish because of (3.20). In general the direction (r_1, r_2) will intersect with the spinodal. In

special (critical) points the direction (r_1, r_2) will be tangent to the spinodal. There two neighboring points will have the same thermodynamic potentials according to (3.21) and are thus also coexisting. In the critical points the spinodal and binodal therefore touch, and the length of the tie lines goes to zero. Critical points are hence the limiting points of coexistence.

We can use equation (3.20) to find the critical points in a ternary system. We first note that equation (3.20) implies that the second derivative of g in the direction (r_1, r_2) vanishes:

$$\sum_{i,j=1}^{2} g_{ij}\, r_i r_j = 0. \tag{3.22}$$

Equation (3.22) follows from (3.20) by multiplication with r_i and summing over i as well as j. In the critical point, where $\vec{r} = (r_1, r_2)$ is tangent to the spinodal, the determinant is stationary (remaining zero), so we have

$$\sum_{i,j,k=1}^{2} g_{ijk}\, r_i r_j r_k = 0, \tag{3.23}$$

which means that the third derivative of g in the direction of $\vec{r}$ vanishes. Combined, equations (3.22) and (3.23) give the conditions for a critical point.

A final question concerns the disappearance of the instability region from composition space. Then the derivative of the determinant will be zero in all directions. Equivalently, using equation (3.23) for the independent x and y directions, we have

$$g_{xxx} = g_{yyy} = 0. \tag{3.24}$$

Together with equation (3.19), equation (3.24) determines what we will call a ternary critical point, or the onset of phase separation. Such a ternary critical point usually does not occur in a Gibbs phase triangle, but if we add an additional axis (*e.g.* for temperature), the resulting three-dimensional phase prism will have such a point.

3.3 Model for ternary lipid mixtures

We denote the volume fractions of the saturated lipids, unsaturated lipids and cholesterol by x, y and z respectively. Analogously to the Flory-Huggins model, we take the fully demixed state as our reference state, and consider the change in Gibbs free energy due to mixing

$$\mathcal{G} = -T\Delta\mathcal{S} + \Delta\mathcal{G}_{\text{loc}}. \tag{3.25}$$

The change in entropy by the increase in available volume when going from a demixed state to a mixed state is $-k_{\text{B}} N_i \log x_i$ for each of the three components (where $\log$ indicates the natural logarithm, x_i as before the number fraction

of the ith component and N_i its total number of molecules). In our ternary system we have

$$\Delta\mathcal{S} = -k_{\text{B}}N\left[x\log x + y\log y + z\log z\right]. \tag{3.26}$$

For each of the three binary mixtures we introduce a Flory-Huggins like local energy term. We assume that the volume is extensive, *i.e.*, scales linearly with the total number of particles N in the system, and therefore x_i is also the volume fraction of the ith component. The probability for two different molecules to encounter each other scales with both their volume fractions. The difference in interaction energy between two identical and two different nearest-neighbor molecules is given by the dimensionless parameter χ [57]. The local interaction term for a mixture of x and y is therefore given by $k_{\text{B}}TN\chi xy$. Below we will show that a model with just three binary interaction terms can not reproduce the experimentally observed phase diagrams. We therefore add another term, which depends on all three volume fractions [64, 68]. This addition supposes a significant contribution from a third-order term to the total free energy. There are two reasons why such a third-order term may occur. The first is if one of the components (here the cholesterol) acts as a line active agent for the phase separation of the other two [73, 74]. In that case all three need to come together at a single point in space, and hence a third-order term emerges. The second option is essentially the one suggested by Radhakrishnan and McConnell [60, 61], which is supported both by numerical studies [75–77] as well as some tentative experimental data [78, 79]. It supposes that the saturated lipids and the cholesterol form complexes, which subsequently interact with the unsaturated lipids. The difference between the model of Radhakrishnan and McConnell and the one proposed here, is that we simply look at the individual components, reflecting the fact that binary complexes are short-lived and continually form and dissociate, as is also seen in simulations [80]. A third order term emerges by combining the probabilities of a two-component complex to form and it meeting up with the third component.

Combining all contributions, we postulate for the local interaction term

$$\Delta\mathcal{G}_{\text{loc}} = k_{\text{B}}TN\left[\chi_{xy}xy + \chi_{xz}xz + \chi_{yz}yz + \bar{\chi}xyz\right], \tag{3.27}$$

and for the total change in Gibbs free energy we have

$$\frac{1}{Nk_{\text{B}}T}\mathcal{G} = x\log x + y\log y + z\log z + \chi_{xy}xy + \chi_{xz}xz + \chi_{yz}yz + \bar{\chi}xyz, \tag{3.28}$$

with (as before, by definition)

$$x + y + z = 1. \tag{3.29}$$

Putting one of the three number fractions equal to zero in equation (3.28), we get the Flory-Huggins model for a binary system, as given by equation (3.6).

A straightforward calculation which can be found in many textbooks (see for example Strobl [57]), tells us that if the corresponding Flory-Huggins parameter χ is less than 2 the entropy term wins and the system is in a single homogeneous phase. If $\chi > 2$ a miscibility gap opens up and the free energy can be lowered by demixing into two coexisting phases.

The ternary term in (3.27) is the only ternary term we can add without changing the underlying binary systems, which is why we do not add any other ternary terms (*e.g.* an xxy term). As we will show below, the ternary term is necessary to explain the existence of a closed loop miscibility gap in systems where the interactions between any pair of the three components are repulsive (*i.e.*, their χ parameters are positive). If there are attractive interactions instead (*e.g.* because one of the components is a solvent for one or both of the others), a closed loop miscibility gap can be described in a system with just the binary interactions [64]. In that case, the closed-loop immiscibility gap results from an asymmetry in the interaction parameters between the three pairs, which is called a $\Delta\chi$-effect [66].

Substituting the free energy given by equation (3.28) in the equations of section 3.2, we can calculate Gibbs phase triangles for given values of χ_{xy}, χ_{xz}, χ_{yz}, and $\bar{\chi}$, and find the binodals, spinodals and critical points. If χ_{xy}, χ_{xz} and χ_{yz} are all less than 2, the corresponding binary systems are homogeneous, but for $\bar{\chi}$ above a critical value the ternary system can still exhibit phase coexistence. An example of a phase diagram with such a closed-loop miscibility gap is given in figure 3.4. The figure shows the binodal and tie lines, which we determine by numerically solving the system given by (3.16). It also shows the spinodal (the solution of equation (3.19)), which in the model given by (3.28) is an algebraic expression in x and y, and the two critical points. We find both the spinodal and the critical points by numerically solving their respective algebraic expressions.

Of course, we can also set the Flory-Huggins parameter of one of the binary mixtures above its critical value 2. If we do so with only one of them, we get a phase diagram with only one critical point, because the immiscibility region continues all the way to the edge of the Gibbs triangle (figure 3.7). In the case that two of the binary parameters allow for binary demixing, we can get more interesting phase diagrams. For certain combinations of the four parameters $\chi_{xy}, \chi_{xz}, \chi_{yz}$ and $\bar{\chi}$ there are three points in the phase triangle for which the chemical potentials match. These points are the vertices of a three-phase coexistence region. Inside there are no tie lines: any system corresponding to any of the points in the three-phase coexistence region will demix in the same fashion. The three-phase coexistence region is bordered by three two-phase coexistence regions, which we can identify as either liquid-liquid or liquid-gel by their densities. An example of such a phase diagram is shown in figure 3.5.

Finally, we use equations (3.19) and (3.24) to find the conditions for having a ternary critical point. Differentiating $g(x, y)$ three times, we find (reintroduc-

ing z to show the symmetry)

$$g_{xxx}(x,y) = \frac{1}{z^2} - \frac{1}{x^2} = 0, \tag{3.30}$$

$$g_{yyy}(x,y) = \frac{1}{z^2} - \frac{1}{y^2} = 0. \tag{3.31}$$

The system consisting of equations (3.29), (3.30) and (3.31) has a single solution: $x = y = z = 1/3$, which means that in our third-order theory a ternary critical point can only occur in the center of the Gibbs phase triangle. Substituting this point into equation (3.19), we find a condition on the parameters χ_{xy}, χ_{xz}, χ_{yz} and $\bar{\chi}$ for a ternary critical point to exist

$$\begin{aligned} 27 - 6(\chi_{xy} + \chi_{xz} + \chi_{yz}) \; + \; & 2(\chi_{xy}\chi_{xz} + \chi_{xy}\chi_{yz} + \chi_{xz}\chi_{yz}) - \chi_{xy}^2 - \chi_{xz}^2 - \chi_{yz}^2 \\ & = \bar{\chi}\left(6 - \frac{2}{3}(\chi_{xy} + \chi_{xz} + \chi_{yz}) - \frac{1}{3}\bar{\chi}\right). \end{aligned} \tag{3.32}$$

If we do not include the third order interaction term in (3.28), the right hand side of equation (3.32) vanishes. In that case there are no solutions for χ_{xy}, χ_{xz} and χ_{yz} all in the interval $[0,2]$. Hence a ternary critical point can only exist if at least one of the underlying binary systems exhibits demixing (with $\chi > 2$) or has an attractive interaction between its components ($\chi < 0$). A system with repulsive interactions between all components can therefore only exhibit a closed loop miscibility gap if $\bar{\chi} > 0$. Given $\chi_{xy}(T)$, $\chi_{xz}(T)$ and $\chi_{yz}(T)$ from the underlying binary systems, equation (3.32) gives us the critical value of $\bar{\chi}$, or equivalently the critical temperature of our ternary system.

3.4 Phase boundary and line tension

Invoking Van der Waals / Cahn-Hilliard theory, we can use our explicit form of the free energy (3.28) to calculate the energy penalty for having a phase boundary. In our two-dimensional membrane system this boundary energy translates to a line tension between domains of different phases. For a detailed introduction into the scheme used here to derive an expression for the line tension, in particular equations (3.35) and (3.36) for a general Gibbs free energy, see Fisk and Widom [81].

We consider two coexisting liquid phases with compositions $(\bar{x}_1, \bar{y}_1, \bar{z}_1)$ and $(\bar{x}_2, \bar{y}_2, \bar{z}_2)$, where we eliminate z as usual. The concentrations do not make a jump at the domain boundary but rather have a smooth transition when we go from one domain to the other. We introduce a new variable s, which we use to parametrize the 'position' between the two phases: for $s \to -\infty$ we are in phase 1 and for $s \to \infty$ we are in phase 2. The origin $s = 0$ is determined as the

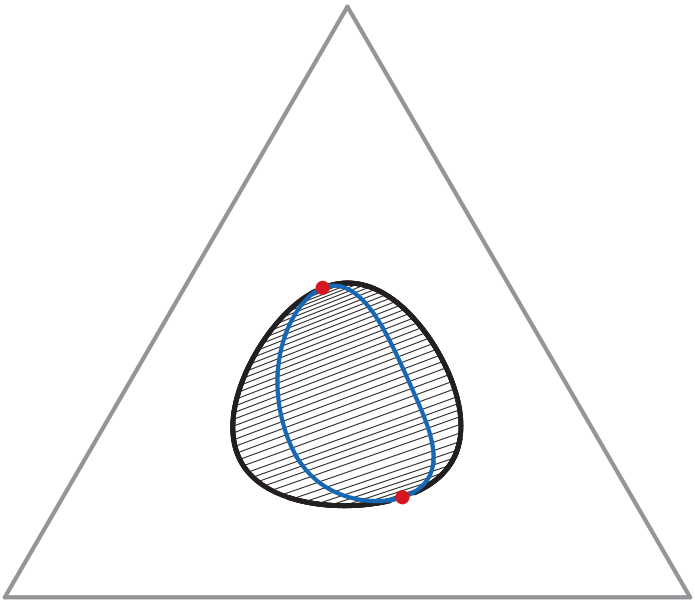

Figure 3.4: Gibbs phase triangle showing phase separation in the ternary system when there is none in any of the binary ones. The thick black line is the binodal, which marks the boundary of the immiscibility region. Any composition corresponding to a point inside the immiscibility region will result in demixing into two states, which are at the ends of the corresponding tie lines (thin black lines). The gray line inside the immiscibility region is the linear instability line (sometimes called the spinodal): points inside the region bordered by the gray line correspond to compositions that will demix by spinodal decomposition, points outside it will demix by nucleation and growth. The thick gray dots indicate the critical points. Parameters used: $\chi_{xy} = 1.5$, $\chi_{yz} = 1.25$, $\chi_{xz} = 0.75$, $\bar{\chi} = 5.0$.

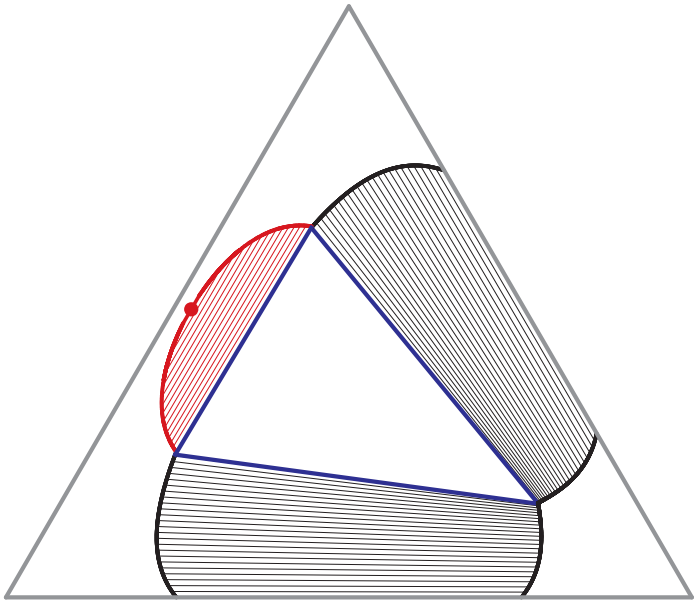

Figure 3.5: Gibbs phase triangle showing separation into two phases (the regions with the thin black and gray lines, which represent tie lines) and three phases (inside the black triangle; the compositions of the three phases correspond to the vertices of the triangle). The regions with black tie lines correspond to the coexistence of a gel and a liquid phase; the region with the gray tie lines corresponds to liquid-liquid coexistence, with a critical point indicated by the thick gray dot. The system is in a homogeneous gel phase in the lower right-hand region and in a homogeneous liquid phase in the left-hand region. Parameters used: $\chi_{xy} = 2.2$, $\chi_{xz} = 1.95$, $\chi_{yz} = 2.15$, $\bar{\chi} = 4.0$.

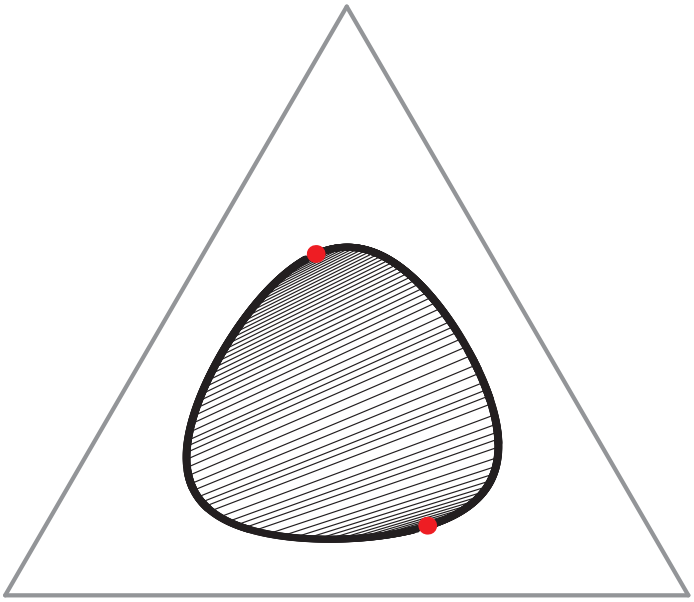

Figure 3.6: Gibbs phase triangle showing phase separation in the ternary system when there is none in any of the binary ones, but one of the binary interactions is attractive. The thick black line is the binodal, which marks the boundary of the immiscibility region. Any composition corresponding to a point inside the immiscibility region will result in demixing into two states, which are at the ends of the corresponding tie lines (thin black lines). The thick gray dots indicate the critical points. In this case, we find numerically that the coexistence region vanishes if the value of the ternary interaction parameter $\bar{\chi}$ is set to 0. Parameters used: $\chi_{xy} = 1.5$, $\chi_{yz} = 1.0$, $\chi_{xz} = -0.5$, $\bar{\chi} = 5.0$.

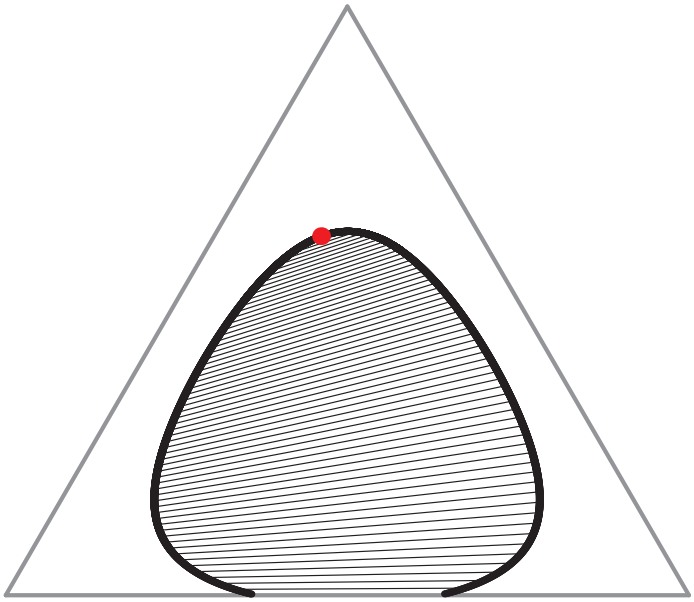

Figure 3.7: Gibbs phase triangle showing phase separation in the ternary system, when one of the underlying binary systems also exhibits phase separation. The thick black line is the binodal, which marks the boundary of the immiscibility region. Any composition corresponding to a point inside the immiscibility region will result in demixing into two states, which are at the ends of the corresponding tie lines (thin black lines). The thick gray dot indicates the critical point. Parameters used: $\chi_{xy} = 2.05$, $\chi_{yz} = 1.25$, $\chi_{xz} = 0.75$, $\bar{\chi} = 5.0$.

location of the Gibbs dividing surface

$$0 = \int_{-\infty}^{0} \Big[\lambda_x(x(s)-\bar{x}_1)+\lambda_y(y(s)-\bar{y}_1)\Big]\,\mathrm{d}s + \int_{0}^{\infty} \Big[\lambda_x(x(s)-\bar{x}_2)+\lambda_y(y(s)-\bar{y}_2)\Big]\,\mathrm{d}s, \quad (3.33)$$

with λ_x and λ_y to be determined. The line tension is then given by the integral of the free energy density $\Psi(x,y)$ (to be defined below):

$$\tau = \int_{-\infty}^{0} \Big[\Psi(x(s),y(s))-\Psi(\bar{x}_1,\bar{y}_1)\Big]\,\mathrm{d}s + \int_{0}^{\infty} \Big[\Psi(x(s),y(s))-\Psi(\bar{x}_2,\bar{y}_2)\Big]\,\mathrm{d}s. \quad (3.34)$$

The key assumption of the Van der Waals / Cahn-Hilliard theory is that Ψ exists for all values of s, and is given by the Gibbs free energy per particle $g(x,y)$ plus a quadratic gradient that accounts for the inhomogeneity in the transition region:

$$\Psi(x(s),y(s)) = g(x(s),y(s)) + \frac{A}{2}\left(\dot{x}^2+\dot{y}^2\right), \quad (3.35)$$

where dots denote derivatives with respect to s. Here we make the simplifying assumption that the y-component of the 'kinetic energy' term has the same 'mass' A as the x-component. We can combine the expression for the line tension with the condition (3.33) into a single functional, where λ_x and λ_y play the role of Lagrange multipliers:

$$\tau = \int_{-\infty}^{\infty} \Big[g(x(s),y(s))-\bar{g}_{12}+\frac{A}{2}\left(\dot{x}^2+\dot{y}^2\right) -\lambda_x(x(s)-\bar{x}_{12})-\lambda_y(y(s)-\bar{y}_{12})\Big]\,\mathrm{d}s, \quad (3.36)$$

where $\bar{g}_{12}$ means $g(\bar{x}_1,\bar{y}_1)$ for $s\le 0$ and $g(\bar{x}_2,\bar{y}_2)$ for $s\ge 0$ with corresponding definitions for $\bar{x}_{12}$ and $\bar{y}_{12}$. Considering the integrand of (3.36) as a Lagrangian, we can invoke the Euler-Lagrange equations and find that for a stable interface ($\delta\tau = 0$) we must have

$$0 = A\ddot{x} - g_x(x(s),y(s)) + \lambda_x, \quad (3.37)$$

$$0 = A\ddot{y} - g_y(x(s),y(s)) + \lambda_y. \quad (3.38)$$

Because the derivatives of $x(s)$ and $y(s)$ must vanish for $s\to\pm\infty$, we find from equations (3.37) and (3.38) for the values of λ_x and λ_y:

$$\lambda_x = g_x(\bar{x}_1,\bar{y}_1) = g_x(\bar{x}_2,\bar{y}_2), \quad (3.39)$$

$$\lambda_y = g_y(\bar{x}_1,\bar{y}_1) = g_y(\bar{x}_2,\bar{y}_2). \quad (3.40)$$

Equations (3.39) and (3.40) are identical to the first and second condition of system (3.17) which determines the binodal. Equations (3.37) and (3.38) are the equations giving Newton's law of motion in the x and y direction of a particle with mass A that experiences a potential $V(x,y)$ given by

$$V(x,y) = -g(x,y) + \lambda_x x + \lambda_y y. \tag{3.41}$$

Moreover, since s does not explicitly appear in the Lagrangian, there is a conserved quantity. In mechanics, this property corresponds to translational invariance, and the conserved quantity is equivalent to the energy of the particle system:

$$E = \frac{A}{2}(\dot{x}^2 + \dot{y}^2) + V(x,y). \tag{3.42}$$

Again taking the limits $s \to \pm\infty$ we find for E:

$$\begin{aligned} E &= -g(\bar{x}_1,\bar{y}_1) + g_x(\bar{x}_1,\bar{y}_1)\bar{x}_1 + g_y(\bar{x}_1,\bar{y}_1)\bar{y}_1 \\ &= -g(\bar{x}_2,\bar{y}_2) + g_x(\bar{x}_2,\bar{y}_2)\bar{x}_2 + g_y(\bar{x}_2,\bar{y}_2)\bar{y}_2, \end{aligned} \tag{3.43}$$

which is identical to the third condition of (3.17).

So far we have expressed both $x(s)$ and $y(s)$ in s independently, but in order to find an expression of the line tension as an integral over the concentration x, we now express $y(s)$ in x, and write

$$E = \frac{A}{2}(1 + y'(x)^2)\dot{x}^2 + V(x,y(x)), \tag{3.44}$$

where the prime denotes a derivative with respect to x. Equation (3.44) gives us an expression for $\dot{x}$:

$$\dot{x} = \sqrt{\frac{2}{A}}\frac{\sqrt{E - V(x,y(x))}}{\sqrt{1 + y'(x)^2}}. \tag{3.45}$$

Using equations (3.41), (3.44) and (3.45) we can rewrite the expression for the line tension (3.36) as

$$\begin{aligned} \tau &= A\int_{-\infty}^{\infty}(1 + y'(x)^2)\dot{x}^2\,\mathrm{d}s \\ &= A\int_{\bar{x}_1}^{\bar{x}_2}(1 + y'(x)^2)\dot{x}\,\mathrm{d}x \\ &= \sqrt{2A}\int_{\bar{x}_1}^{\bar{x}_2}\sqrt{1 + y'(x)^2}\sqrt{E - V(x,y(x))}\,\mathrm{d}x \end{aligned} \tag{3.46}$$

Equation (3.46) again gives a functional expression for the line tension, for which we can again write down the Euler-Lagrange equations to get a differential equation for the optimal path $y(x)$. Because the integrand in (3.46) depends explicitly on x, there is no conserved quantity in this system. Performing

the variational analysis, we find after some algebra

$$y''(x) = \frac{1+y'(x)^2}{2(E-V(x,y))}\left(-\frac{\partial V(x,y)}{\partial y} + \frac{\partial V(x,y)}{\partial x}\,y'(x)\right). \tag{3.47}$$

It seems straightforward to determine the optimal path from $(\bar{x}_1, \bar{y}_1)$ to $(\bar{x}_2, \bar{y}_2)$ by direct integration of the second-order differential equation (3.47). Unfortunately, there are two complications. The first is that both endpoints are singular points because $y''(x)$ tends to diverge close to the endpoints due to the factor $E - V(x, y(x))$ in the denominator of equation (3.47). The second complication is that the integration of the entire path is highly unstable. To avoid these complications we optimize τ by making a guess for $y(x)$, and compare the guess to equation (3.47). The most obvious guess is a straight line, *i.e.*, $y(x)$ follows the tie line that connects $(\bar{x}_1, \bar{y}_1)$ with $(\bar{x}_2, \bar{y}_2)$, which gives us an upper bound for the value of τ. However, a better guess can be made by assuming a quadratic profile which has a free parameter that we can optimize (*i.e.*, tune it such that we find the lowest possible value of τ, or the 'best' solution of equation (3.47)). We notice that, according to this numerical approximation, the direction of $y(x)$ at the points at which it intersects the spinodal, coincides with that of the eigenvector $\vec{r}$ associated with the zero eigenvalue of (g_{ij}), (*i.e.*, the unstable direction, see figure 3.8). Although these quadratic profiles do not exactly solve equation (3.47), the deviation is small and only significant close to the endpoints. Because there the factor $\sqrt{E - V(x, y(x))}$ in the expression for τ vanishes, the estimate for τ using the quadratic profile is a reliable one. In appendix 3.A we show how to turn the first complication into an advantage, by which we can improve the guess, using a quartic profile. However, as we also show, the improvement of the estimate of τ using this quartic profile is negligible with respect to the optimal parabola.

3.5 Summary and discussion

In this chapter we have introduced phase diagrams of ternary mixtures. We have briefly reviewed the thermodynamics of mixtures, and the Flory-Huggins model which describes binary systems. Moreover, we have reviewed the models currently available in the literature to describe the phase diagrams at given temperature and pressure (Gibbs triangles) of ternary mixtures. None of these models succeed in capturing both the existence of a 3-phase coexistence region and (at different temperatures) a closed-loop miscibility gap. We have shown that using a simple extension of the Flory-Huggins model, namely the introduction of a third order interaction term, already well known in the fields of alloys and of polymer mixtures, is capable of capturing both effects in a single model. Moreover, we have shown that simply adding the three binary interactions without a third order term is insufficient to reproduce the closed-loop

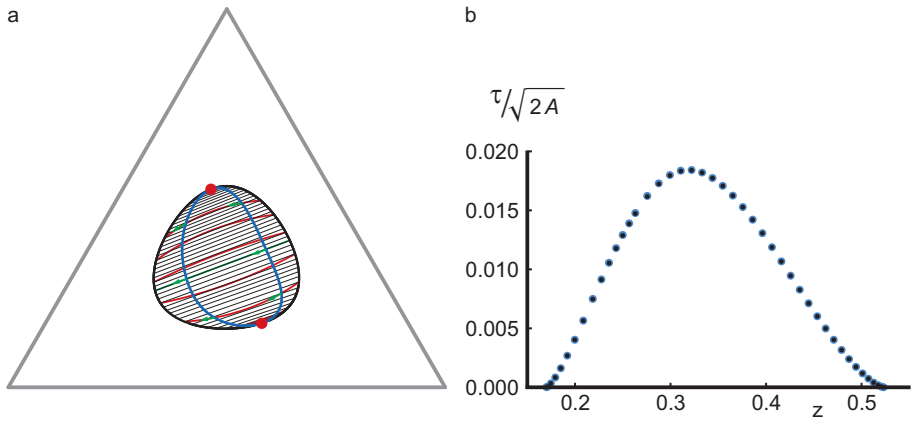

Figure 3.8: Line tension estimates using an optimized quadratic profile for $y(x)$ in equation (3.46). (a) Gibbs phase triangle showing the binodal (thick black line), tie lines (thin black lines), spinodal (blue line) and critical points (red dots). Some optimal quadratic paths connecting coexisting phases are shown (in red and green), as well as the directions of the eigenvectors of the zero eigenvalues of (g_{ij}) at the spinodal (in green). (b) Estimated values of $\tau/\sqrt{2A}$ determined using the optimal quadratic profiles shown in the left figure, as a function of 'position' between the critical points (the z-coordinate of the center of the corresponding tie line). The figure shows both the estimates determined using the optimal quadratic profiles shown in the left figure (big blue dots), as well as those determined using the optimal fourth-order profile as given in the appendix (small black dots); the positions of the points are indistinguishable in the plot. The line tension vanishes at both critical points and has a maximum when the optimal quadratic profile is a straight line, connecting the points on the binodal with the largest separation (green line in left figure). Parameters used: $\chi_{xy} = 1.5$, $\chi_{yz} = 1.25$, $\chi_{xz} = 0.75$, $\bar{\chi} = 5.0$.

miscibility gap if all binary interactions are repulsive, and even if one of them is weakly attractive.

Physically the ternary term we have added can be interpreted in at least two ways: the cholesterol may act as a line active agent at the phase boundary of the other two lipids, or alternatively, it may form a dynamic complex with one of the two other lipids which subsequently interacts with the remaining one. Since both the experimentally determined and the predicted tie-lines in the Gibbs triangles exhibiting liquid-liquid phase coexistence suggest that cholesterol is unequally distributed between the two liquid phases, we consider the second scenario to be the most probable one. However, in order to unambiguously distinguish between these two scenarios one should perform an experiment in which the cholesterol is labeled and its location determined in a (partially) phase separated lipid membrane vesicle.

In contrast to some of the other available models, the model we use does not take the effect of ordering into account. It is well known that the three different phases (L_d, L_o and gel) have different amounts of ordering, but it remains an open question whether this is a cause or a consequence of phase separation. We interpret the phase separation as the consequence of individual binary or ternary molecule-molecule interactions, but other approaches are certainly possible.

Using the ternary model given by equation (3.28) we have calculated the stability properties of the various phase diagrams, and determined the stability lines or spinodals, as well as the critical points. We have also derived an expression for the line tension between two coexisting phases in a lipid membrane system, as a function of the position in the phase diagram. This approach directly couples the line tension between coexisting domains, a key factor in the determination of the shape of lipid membrane vesicles, to the composition of the membrane.

Although the model we use qualitatively reproduces the experimentally observed features listed above, there is as yet no quantitative comparison to experiment. In principle such a comparison would be possible. The model for the Gibbs free energy has four free parameters, of which three are determined by the underlying binary systems and can be obtained from measurements on those. The fourth parameter ($\bar{\chi}$) can be determined experimentally using *e.g.* equation (3.32) for the ternary critical point. Given the values of these parameters, the value of the line tension can be calculated up to the overall proportionality factor A, which corresponds to a correlation length, and can in principle be determined independently. Experimental data with which this procedure can be carried out is currently not available. It might be possible to obtain such data with careful experiments, but they would be hard to carry out: the temperature, pressure and composition in all experimental systems should be controlled with high accuracy. Moreover, for each point in the phase diagram a new membrane has to be constructed, so the experiments would also be time-consuming. Apart from experimental difficulties, there is an impor-

tant assumption in this procedure which can not be checked directly, namely that the values of the binary interaction parameters remain unchanged in the ternary system. These parameters represent individual molecule-molecule interactions, for which we thus assume that the environment does not play an important role. Finally, in the derivation of the expression for the line tension τ, the expression for the free energy density Ψ given by (3.35) assumes that variations in the cholesterol concentration z are small, and that the scale factor A is identical for all lipids. Especially this last point is not necessarily true, and could affect estimates for τ using the calculations presented here.

In the next chapters, we will study the shape of (meta-)stable phase separated vesicles. The line tension on the boundaries will play an important role, both in the coarsening process (the merging of domains of the same phase) and in determining the shape. In chapter 4 we develop a model for the shape of a completely phase separated vesicle, based on the differential geometry techniques introduced in chapter 2, which we use to obtain the value of the line tension from experiments. In chapters 5 and 6 we study vesicles which are trapped in a kinetically arrested state. Their phase diagrams resemble the one given in figure 3.4. They are prepared at high temperature (such that their membrane is a uniform mixture), and subsequently quenched such that they end up in the liquid-liquid phase coexistence regime. They quickly nucleate domains, typically L_o domains in a L_d background. However, the domains do not all immediately merge, but remain stable for a long time, due to membrane deformations which are a result of the interplay between the line tension and the membrane's elastic bending energy. We study the patterns which emerge and sorting on the scale of the domains themselves.

3.A Optimal concentration profile

Close to the binodal, the factors $(E - V(x, y(x)))$, $\partial V(x,y)/\partial y$ and $\partial V(x,y)/\partial x$ in equation (3.47) all vanish. However, as we will show below, the first one vanishes quadratically with x, whereas the second and third only vanish linearly with x. Because the numerator and denominator of equation (3.47) should vanish equally fast as we approach the binodal in order for the second derivative of $y(x)$ to be well-defined, this allows us to find an expression for the first derivative of $y(x)$ at both ends of the interval. Those values we can use to improve our estimate of the concentration profile: since we now know both the endpoints and the derivatives at those endpoints, we have four set parameters and can optimize a fourth-order, instead of a quadratic, profile with a single optimization parameter. We will show that the fourth-order profile gives a marginal improvement in the estimate of the line tension τ, indicating that indeed the quadratic profile used in the main text gives a reliable estimate.

We rewrite equation (3.47) as an expression without fractions as

$$2(E - V(x,y))y''(x) = (1 + y'(x)^2)\left(-\frac{\partial V(x,y)}{\partial y} + \frac{\partial V(x,y)}{\partial x}\, y'(x)\right). \quad (3.48)$$

We reparametrize such that the origin is at the point around which we make our expansion (either $(\bar{x}_1, \bar{y}_1)$ or $(\bar{x}_2, \bar{y}_2)$). We expand $y(x)$ around this origin and write

$$y(x) = a_1 x + a_2 x^2 + a_3 x^3 + a_4 x^4 + \ldots \quad (3.49)$$

We also define

$$V_x = \frac{\partial V(x,y)}{\partial x}(0,0) \quad (3.50)$$

$$V_y = \frac{\partial V(x,y)}{\partial y}(0,0) \quad (3.51)$$

and likewise for higher-order derivatives. For the left-hand side of (3.48) we then find

$$2(E - V(x,y))y''(x) = a_2\left(a_1^2 V_{yy} + 2a_1 V_{xy} + V_{xx}\right)x^2 + \mathcal{O}\left(x^3\right), \quad (3.52)$$

where we have left out all terms which are zero by virtue of equations (3.39), (3.40) and (3.43). The expansion of the right-hand side of (3.48) gives (again leaving out terms which are zero):

$$\begin{aligned}(1 + y'(x)^2)\left(-\frac{\partial V(x,y)}{\partial y} + \frac{\partial V(x,y)}{\partial x}\, y'(x)\right) = \\ -(1+a_1^2)\left[(1-a_1^2)V_{xy} + a_1\left(V_{yy} - V_{xx}\right)\right]x \\ +\frac{1}{2}\Big[-2a_2\left((1+5a_1^2)V_{yy} + a_1(1-7a_1^2)V_{xy} - 2(1+3a_1^2)V_{xx}\right) \\ +(1+a_1^2)\left(-a_1^2 V_{yyy} - a_1(2-a_1^2)V_{xyy}\right. \\ \left.-(1-2a_1^2)V_{xxy} + a_1 V_{xxx}\right)\Big]x^2 + \mathcal{O}\left(x^3\right). \quad (3.53)\end{aligned}$$

The lowest-order term of the left-hand side of equation (3.48) thus goes as x^2, whereas the lowest-order term of the right-hand side goes as x. The coefficient of x should therefore vanish for equation (3.47) to be well-defined at the binodal, which gives the condition:

$$a_1^2 - \frac{V_{yy} - V_{xx}}{V_{xy}}a_1 - 1 = 0, \quad (3.54)$$

at both endpoints. Using condition (3.54) to calculate $y'(x)$ at $\bar{x}_1$ and $\bar{x}_2$, we have four conditions on $y(x)$. We use those to fix four of the five parameters in a fourth-order polynomial approximation of $y(x)$, leaving a single parameter which we use to optimize τ in the same fashion as we did with the quadratic approximation. Figure 3.8 shows the values of τ we obtain from both the quadratic and fourth-order profiles, illustrating that they are virtually the same and showing that the quadratic approximation suffices.

CHAPTER 4

MEMBRANE SHAPES

In this chapter we study the shape of biomimetic ternary membranes. We find that in their ground state, vesicles which exhibit domains of two different phases fully phase-separate. The resulting shape is a trade-off between two competing effects: an elastic term, which wants the membrane to be as smooth as possible, and a boundary term, which wants to minimize the domain boundary length. The resulting minimal shape resembles a peanut or a snowman. We study the fluctuations of the membrane around this equilibrium shape. Moreover, we derive an analytical expression for the shape of the ground state. Fitting both the fluctuation spectrum and the equilibrium shape, we can extract the membrane's elastic (bending) modulus and the energy associated to the domain boundary (the line tension). The numbers we obtain can be used to give estimates and limits for the size and stability of nanodomains in the plasma membrane of living cells.

4.1 Introduction

In chapter 3 we studied the phase separation of biomimetic ternary membranes into liquid ordered (L_o) and liquid disordered (L_d) domains. Once phase separation starts, the domains have different physical parameters due to their unequal compositions. Moreover, a line tension associated to their boundaries emerges, as studied in section 3.4. The line tension contribution to the energy causes the domains to be circular in shape, minimizing their circumference for a given area. It also drives a coarsening process, since merging domains into larger ones reduces the total domain boundary length. Not surprisingly, the ground state is therefore a complete phase separation: a vesicle containing one L_o and one L_d domain.

There is an additional mechanism by which the line tension energy can be reduced: deformation of the vesicle. A uniform vesicle typically assumes a spherical shape, because that shape minimizes its bending energy (see section 2.3.5). If the total area and enclosed volume of the vesicle are fixed, it will always remain a sphere. However, over long timescales water can permeate the lipid bilayer membrane and the enclosed volume can be reduced. Using this degree of freedom, the energy associated with the line tension on the domain boundary can be reduced as well: by contracting the boundary, the vesicle can create a neck. If the line tension is large enough, the neck can be completely contracted and the vesicle can split in two, one part containing (mostly) a L_d membrane, the other a L_o one [6, 69, 82, 83]. The reason why this does not always happen is that this budding process is countered by the bending energy: the creation of the neck increases the total curvature of the vesicle. For moderate values of the line tension, the resulting stable shape therefore is a balance between the bending energy and the line tension energy, and resembles the 'snowman' of figure 2.1b. An example of an experimentally obtained picture of such a 'snowman' vesicle is shown in figure 4.1.

In this chapter we derive an analytical expression for the shape of a fully phase-separated vesicle. We verify the expression found by comparing it to the numerical shape obtained by minimizing the full energy functional. Moreover, we fit this model to experimental data to obtain numbers for the line tension τ and difference in Gaussian moduli of the phases $\Delta\bar{\kappa}$. Finally, we compare these numbers to existing models for living systems and use them to speculate on the existence and size of domains in the plasma membrane of cells.

The results reported in this chapter again apply to ternary vesicles, containing cholesterol, a low melting temperature lipid, and a high melting temperature lipid. In the experimental data presented here the low melting temperature lipid is DOPC and the high melting temperature lipid is (brain) sphingomyelin (SM). Alternatively, several other groups have used DPPC as the high melting temperature lipid and a great variety of low melting temperature lipids in their experiments, giving qualitatively similar results, see *e.g.* [2, 4–6, 54, 55, 79, 84–87]. Typically the L_o domains are rich in both sat-

urated tail lipids and cholesterol, whereas L_d domains are rich in lipids with unsaturated tails, see chapter 3.

The experimental data presented in this chapter was obtained by S. Semrau from the Leiden experimental biophysics group, and is used with permission. The experimental setup and procedure are briefly sketched in appendix 4.A; a more detailed overview can be found in [43].

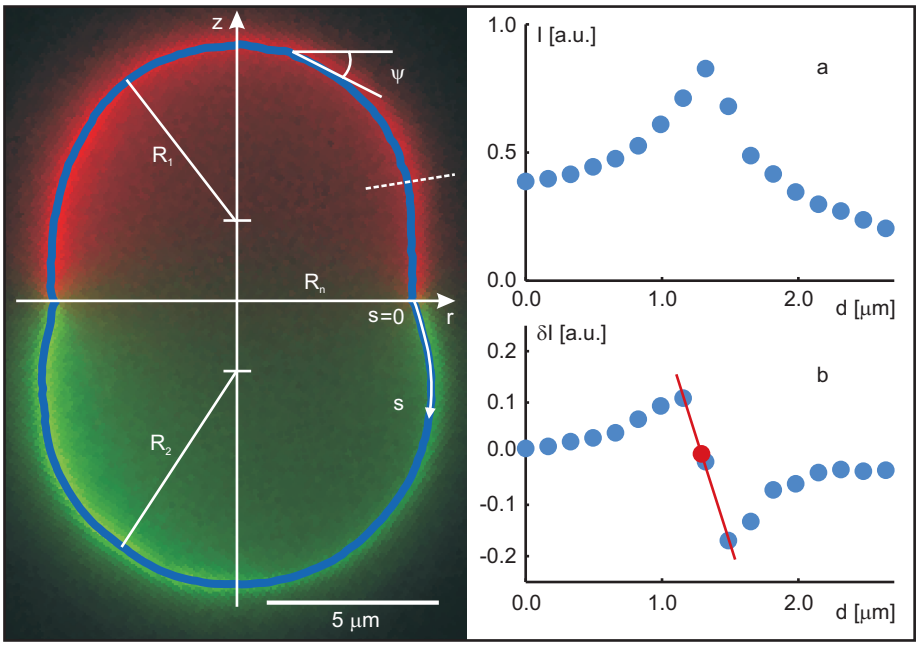

Figure 4.1: Equilibrium shape of a tricomponent vesicle which exhibits phase separation into a L_o and a L_d phase. The two phases have approximately equal surface area and the vesicle has been allowed to equilibrate for several weeks, allowing it to adjust its volume by transport of water molecules through the membrane. The resulting 'snowman' shape is the result of a balance between the bending energy and the line tension. The left figure shows the fluorescence raw data, with the L_o domain in red and the L_d domain in green; the contour is superimposed in blue. The insets on the right illustrate the principle of contour fitting. (a) Intensity profile normal to the vesicle contour (taken along the dashed line in the main image); (b) first derivative of the profile with linear fit around the vesicle edge (red line). The red point marks the vesicle edge.

4.2 Energy functional and shape equation

The free energy of the fully phase-separated vesicle with two domains (indicated by subscripts 1 and 2) is given by equation (2.102):

$$\mathcal{E} = \sum_{i=1}^{2} \int_{\mathcal{M}_i} \left(\frac{\kappa_i}{2}(2H)^2 + \bar{\kappa}_i K + \sigma_i \right) \mathrm{d}S + p \int \mathrm{d}V + \tau \oint_{\partial\mathcal{M}} \mathrm{d}l. \tag{4.1}$$

where the κ_i and $\bar{\kappa}_i$ are the bending and Gaussian moduli of the two domains, respectively, the σ_i are their surface tensions, τ is the line tension on their boundary and p is the pressure difference across the membrane. In the equilibrated shapes considered here, the force of the internal Laplace pressure is compensated by the surface tensions; consequently, both contributions drop out of the shape equations [48, 51]. As was shown in section 2.3.4, the Gauss-Bonnet Theorem allows us to integrate the Gaussian curvature term to a constant contribution on the bulk of each domain plus a boundary term. Within the bulk of each domain, the only relevant contribution to the energy is therefore giving by the bending term. Exploiting the fact that the vesicle is axisymmetric, and using the same notation as in section 2.3.5, we find that the shape of each bulk part is given by the following differential equation:

$$\ddot{\psi}\cos\psi = -\frac{1}{2}\dot{\psi}^2 \sin\psi - \frac{\cos^2\psi}{r}\dot{\psi} + \frac{\cos^2\psi + 1}{2r^2}\sin\psi. \tag{4.2}$$

where $\psi(s)$ is the tangent angle to the membrane, s the arc length measured along the vesicle contour and dots denote derivatives with respect to the arc length (see figure 2.1b). The vesicle's coordinates $r(s)$ and $z(s)$ are related to the tangent angle via the geometrical relations given by equations (2.88) and (2.89):

$$\dot{r} = \frac{\mathrm{d}r}{\mathrm{d}s} = \cos\psi(s), \tag{4.3}$$

$$\dot{z} = \frac{\mathrm{d}z}{\mathrm{d}s} = -\sin\psi(s). \tag{4.4}$$

We put the boundary between the two domains at $z = 0$ and also define $s = 0$ at this point. Of course r and ψ must be continuous at the boundary. As we derived in section 2.3.5, the variational derivation of equation (4.2) gives two more boundary conditions on $\dot{\psi}$ and $\ddot{\psi}$ [52]:

$$\lim_{\varepsilon\downarrow 0}(\kappa_2\dot{\psi}(\varepsilon) - \kappa_1\dot{\psi}(-\varepsilon)) = -(\Delta\kappa + \Delta\bar{\kappa})\frac{\sin\psi_0}{r_0}, \tag{4.5}$$

$$\lim_{\varepsilon\downarrow 0}\left(\kappa_2\ddot{\psi}(\varepsilon) - \kappa_1\ddot{\psi}(-\varepsilon)\right) = \left(2\Delta\kappa + \Delta\bar{\kappa}\right)\frac{\cos\psi_0\sin\psi_0}{r_0^2} + \frac{\sin\psi_0}{r_0}\tau, \tag{4.6}$$

where $\Delta\kappa = \kappa_2 - \kappa_1$, $\Delta\bar{\kappa} = \bar{\kappa}_2 - \bar{\kappa}_1$, and $r_0 = r(0)$ and $\psi_0 = \psi(0)$, are the radial coordinate and contact angle at the domain boundary.

4.3 Neck and bulk solutions

Far away from the domain boundary, the influence of the line tension at the boundary on the membrane shape is small. We therefore expect the membrane bending term to dominate the shape in the bulk of each domain. The optimal solution is then the least curved one, which is a sphere. Indeed the sphere is a solution of equation (4.2), and in the experimental pictures we clearly see that around the poles of the vesicle (putting the domain boundary at the equator) the shape becomes approximately spherical. We can therefore use the sphere as a first ansatz for the shape far from the domain boundary. Expanding around this ansatz, we can find corrections to the spherical shape from the shape equation (4.2). Close to the domain boundary, this approach breaks down, as the shape around the boundary is determined by the line tension, through the boundary conditions (4.5) and (4.6). We therefore split each of the domains into a bulk and a neck regime, where respectively the bending energy and the line tension dominate the shape.

As before, we put the domain boundary at $s = 0$. We denote the total arc length of the top domain by s_b and that of the bottom domain by s_e. The arc length coordinate s therefore has negative values in the top domain and positive values in the bottom domain, and runs over $(-s_b, s_e)$. The boundaries between the neck and bulk regimes in both domains are located at $s = -s_1$ and $s = s_2$ and the radii of the asymptotically approached spheres in both domains are given by R_1 and R_2.

For the bulk domains, we perform an analysis of small perturbations in $\psi(s)$ from the spherical ansatz. Due to the fact that we use an angular coordinate, there is a singularity at the poles of the vesicle, which translates into a divergence in the perturbative correction term. This divergence is unphysical and purely a consequence of the choice of coordinates. We should therefore restrict the perturbation to a region in which our chosen coordinate system has no singularities. The easiest choice is to calculate the perturbation for the region from $\psi = \pi/2$ to the domain boundary for the top domain, and analogously for the bottom domain. The details of the derivation of the bulk solution are given in appendix 4.C, the resulting shape is given by:

$$\psi_{\text{bulk}}(s) = \begin{cases} \frac{s+s_b}{R_1} & -s_b \leq s \leq -s_b + \pi R_1/2 \\ \frac{s+s_b}{R_1} + \frac{A_1 R_1^2}{2}\delta\psi\left(\frac{s+s_b}{R_1}\right) & -s_b + \pi R_1/2 \leq s \leq -s_1 \\ \pi + \frac{s-s_e}{R_2} + \frac{A_2 R_2^2}{2}\delta\psi\left(\pi + \frac{s-s_e}{R_2}\right) & s_2 \leq s \leq s_e - \pi R_2/2 \\ \pi + \frac{s-s_e}{R_2} & s_e - \pi R_2/2 \leq s \leq s_e \end{cases} \tag{4.7}$$

with

$$\delta\psi(x) = \frac{1}{\sin(x)} + x\log\left(\tan\left(\frac{x}{2}\right)\right) + i\left[\mathrm{Li}_2\left(i\tan\left(\frac{x}{2}\right)\right) - \mathrm{Li}_2\left(-i\tan\left(\frac{x}{2}\right)\right)\right] - (1-2K), \quad (4.8)$$

where A_1 and A_2 are integration constants, K is Catalan's constant, with numerical value ~ 0.91596559, and $\mathrm{Li}_n(z)$ the polylogarithm or Jonquière's function, defined as

$$\mathrm{Li}_n(z) = \sum_{k=1}^{\infty} \frac{z^k}{k^n}, \quad (4.9)$$

for $z \in \mathbb{C}$. The term containing the two polylogarithms in (4.8) is real for our region of interest ($-\pi < x < \pi$).

Near the domain boundary, ψ must have a local extremum in each of the phases and we can expand it as

$$\psi_{\mathrm{neck}}(s) = \begin{cases} \psi_0^{(1)} + \dot{\psi}_0^{(1)} s + \frac{1}{2}\ddot{\psi}_0^{(1)} s^2 & -s_1 \le s \le 0 \\ \psi_0^{(2)} + \dot{\psi}_0^{(2)} s + \frac{1}{2}\ddot{\psi}_0^{(2)} s^2 & 0 \le s \le s_2 \end{cases} \quad (4.10)$$

Because of the local extremum, the expansion for ψ_{neck} should be at least to second order. Because the boundary condition on $\ddot{\psi}$ tells us that due to the presence of a line tension at the domain boundary, $\dot{\psi}$ will be discontinuous at that boundary, so we can not go beyond second order without putting in additional information. The Canham-Helfrich energy functional (4.1) used here does not give that information; in order to refine the model we would need to use an energy functional that goes to at least fourth (instead of second) order in the local curvature (see section 2.3.5). For the model presented here, an expansion to second order for ψ_{neck} is therefore the appropriate one to use.

At the boundaries $s = -s_1$ and $s = s_2$ between the bulk and neck regimes, their respective solutions (4.7) and (4.10) should match smoothly. That means that ψ, as well as $\dot{\psi}$ and $\ddot{\psi}$ must be continuous at these points. Because we find $r(s)$ by integrating $\cos\psi(s)$, continuity of $\psi(s)$ implies continuity of $r(s)$ and no additional conditions are imposed at the regime boundaries. At the domain boundary ($s = 0$), the solution needs to satisfy the boundary conditions (4.5) and (4.6), as well as continuity of $\psi(s)$. Finally, there is a boundary condition on $r(s)$, which is that it must vanish at either pole (at $s = -s_b$ and $s = s_e$) to produce a closed vesicle. Equivalently, we can set $r(-s_b) = r(s_e) = 0$ and find $r_0 = r(0)$ by integration over each domain, giving the condition that $r(s)$ must be continuous at the domain boundary. In total, we have 10 conditions for the 10 unknowns $\{A_i, s_i, \psi_0^{(i)}, \dot{\psi}_0^{(i)}, \ddot{\psi}_0^{(i)}\}_{i=1,2}$.

Combined, the neck and bulk components of ψ give a vesicle solution for specified values of the material parameters $\{\kappa_i, \Delta\bar{\kappa}, \tau\}$. This solution compares extremely well to numerically determined shapes (obtained using the

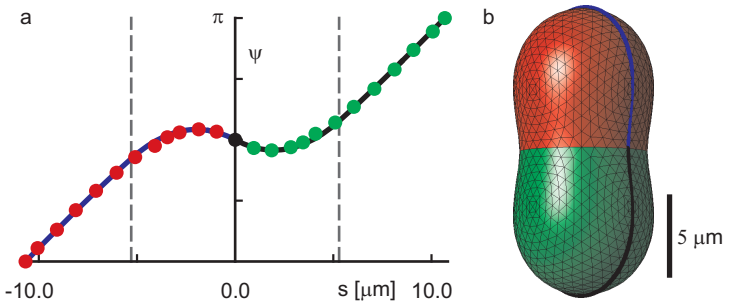

Figure 4.2: Numerically determined shape of a fully phase-separated vesicle with two domains of equal size. The shape was found by minimizing the free energy (4.1) by means of relaxation steps, using the software package Surface Evolver by Brakke [44]. The L_o phase is shown in red, the L_d phase in green. (a) Plot of contact angle ψ versus contour length s. The blue and black line shows the best fit of the model given by equations (4.7) and (4.10). The dashed lines mark the transition points between the neck and bulk regimes. (b) 3D representation of the entire vesicle. The optimal fit is again shown as a blue/black line.

Surface Evolver package [44], see figure 4.2). Moreover, for the symmetric case of domains with identical values of κ, we can compare to earlier modeling in Ref. [82]. The vesicle can then be described by a single dimensionless parameter $\lambda = R_0/\xi$, where $4\pi R_0^2$ equals the vesicle area, and $\xi = \kappa/\tau$ is known as the *invagination length*. The budding transition (where the broad neck destabilizes in favor of a small neck) is numerically found in Ref. [82] to occur at $\lambda = 4.5$ for equally sized domains; the model presented here gives a value of $\lambda = 4.63$.

4.4 Bending moduli and line tensions

The model for the shape of a fully phase-separated vesicle given by equations (4.7) and (4.10) has the bending moduli κ_i of the two domains, the line tension τ between them and the difference $\Delta\bar{\kappa}$ between their Gaussian moduli as input parameters. Moreover, the radii R_i of the two bulk spheres, and the sizes s_b and s_e of the domains, are also free parameters in the model and should be obtained from experiment. A direct fit of the model to an actual vesicle shape would therefore have many fit parameters and thus give unreliable results. Fortunately, the experimental data available provides us with more information than just the equilibrium shape of the vesicles. Using advanced detection techniques (see figure 4.1), it is possible to determine the membrane position

with an accuracy of $20\ \mathrm{nm}$, sufficient to determine the fluctuation spectrum, because thermal fluctuations occur on the scale of $50 - 100\ \mathrm{nm}$ [70]. From the vesicle shape we can directly obtain the radii and domain sizes. The bending moduli can subsequently be found from the fluctuation spectra, and the fit of the analytical model given by equations (4.7) and (4.10) finally gives the line tension and difference in Gaussian modulus.

We determined the bulk sphere radii R_i from the ensemble averaged radii of circles fitted to those parts of the contours that were nearly circular, *i.e.*, far away from the neck domain. We similarly found the domain sizes as the ensemble averaged total arc length of the equilibrium shape. We subsequently obtained spectra of the shape fluctuations for the nearly circular parts of the contour. We determined the fluctuations $u(s)$ for each single contour as the difference between the local radius r and the ensemble averaged radius R_i: $u(s) = r(s) - R_i$, with s again the arc length, see figure 4.3. Expanding fluctuations of the Canham-Helfrich free energy (2.78) in Fourier modes and invoking the Equipartition Theorem, we find an expression for the fluctuation spectrum in terms of the bending modulus κ and surface tension σ (see appendix 4.B). Taking into account the finite patch size [88] and following the spectral analysis of a closed vesicle shell developed by Pécréaux *et al.* [89], we find for the power spectrum for the vesicle fluctuation $u(s)$:

$$\overline{\langle |u_k|^2 \rangle} = \sum_{q_x} \left(\frac{\sin((k-q_x)\frac{a}{2})}{(k-q_x)\frac{a}{2}} \right)^2 \frac{k_{\mathrm{B}}T}{4\pi\eta L} \int_{-\infty}^{\infty} \mathrm{d}q_y \frac{\tau_q}{|\vec{q}|} \frac{\tau_q^2}{t^2} \left(\frac{t}{\tau_q} + e^{-t/\tau_q} - 1 \right). \tag{4.11}$$

Here $\vec{q} = (q_x, q_y) = \frac{2\pi}{L}(m,n)$ with m and n non-zero integers, $L = 2\pi R_i$, and η is the bulk viscosity of the surrounding medium. The overline indicates averaging over the illumination time, and the brackets denote the ensemble average. Fitting equation (4.11) to the measured fluctuation spectra (figure 4.3), we can extract the bending moduli and the surface tensions of both domains simultaneously. The numbers for five different vesicles of the same composition are listed in table 4.1. As can be seen from this table, the measured bending moduli $\kappa_{\mathrm{o}} = 8.0 \pm 0.7 \cdot 10^{-19}\ \mathrm{J} = 2.0 \pm 0.2 \cdot 10^2\, k_{\mathrm{B}}T$ and $\kappa_{\mathrm{d}} = 1.9 \pm 0.5 \cdot 10^{-19}\ \mathrm{J} = 50 \pm 13\, k_{\mathrm{B}}T$ of the L_{o} and L_{d} domains are the same for all five vesicles, confirming that these are a property of the membrane composition. In contrast, the values found for the surface tensions vary for the five vesicles measured, reflecting the fact that they depend on the exact preparation procedure and in particular the (small) pressure difference across the membrane. Using the values found from the fluctuation analysis, we have only two free parameters left in our model: the line tension τ and difference in Gaussian moduli $\Delta\bar{\kappa}$. We fitted the model given by equations (4.7) and (4.10) to the measured equilibrium shape in two ways to obtain the values of these parameters. The first method we used is a two-parameter fit, allowing the shape to optimize as a function of both parameters. The second method was to assume continuity of $\dot{\psi}$ across the domain boundary. This additional as-

sumption gives a direct relation between τ and $\Delta\bar{\kappa}$, leaving us with a single fit parameter. Both methods yield the same values for τ and $\Delta\bar{\kappa}$, which are listed in table 4.1 along with the bending moduli and surface tensions. As we would expect, the line tension depends on composition only, and for our specific choice has the value of 1.2 ± 0.3 pN, which is in the same range as that estimated by Baumgart *et al.* [6]. For the difference in Gaussian moduli we find $3 \pm 1 \cdot 10^{-19}$ J $= 8 \pm 3 \cdot 10^{1}\, k_B T$, in accordance with the earlier established upper bound ($\bar{\kappa} \leq -0.83\kappa$) reported by Siegel and Kozlov [90]. An example fit is given in figure 4.4.

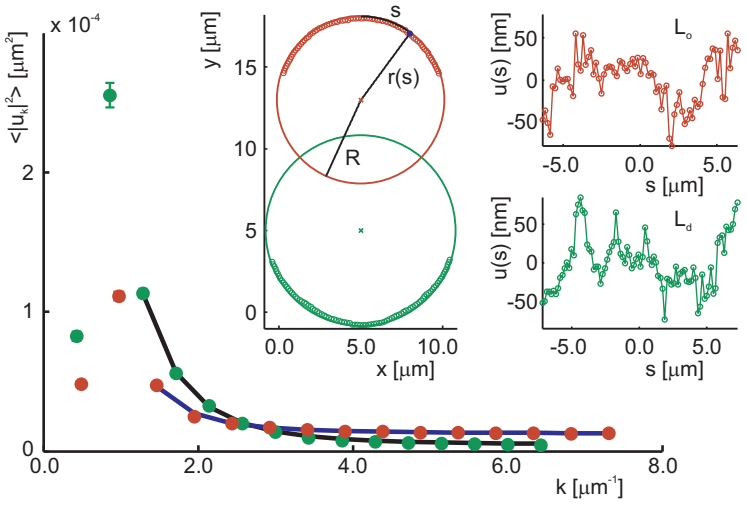

Figure 4.3: Fluctuation spectra of the ordered (red circles) and disordered (green circles) domains. The corresponding best fits of equation (4.11) are shown in blue and black respectively. Inset: Typical real-space fluctuations along the vesicle perimeter. Figure taken from [70].

4.5 Biological implications

Ultimately, we are interested in the membrane's elastic parameters because their precise magnitude has important consequences for the morphology and dynamics of cells. The literature is replete with theoretical speculations which depend strongly on, among others, the line tension. While the values we report apply to reconstituted vesicles, we can nonetheless use them in some of these models to explore possible implications for cellular membranes. The majority of the investigated vesicles finally evolved into the fully phase separated state. This finding is in agreement with previous work by Frolov *et al.* [91],

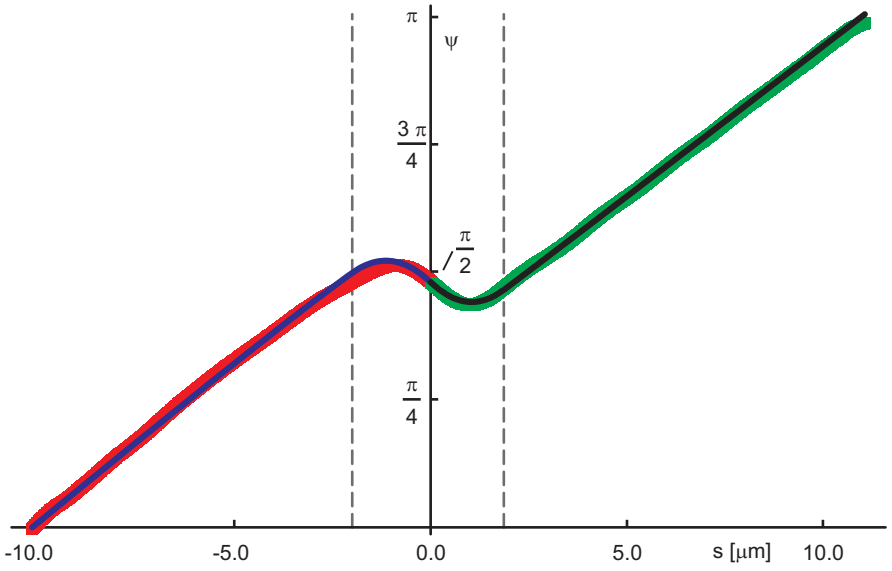

Figure 4.4: Example of an experimentally obtained $\psi(s)$ plot (red: L_o phase, green: L_d phase) together with the best fit of the model given by equations (4.7) and (4.10) in blue and black. The dashed lines mark the transition points between the neck and bulk regimes.

which predicts, for line tensions larger than $0.4\ \mathrm{pN}$, complete phase separation for systems in equilibrium. It should be noted that the line tension found is also smaller than the critical line tension leading to budding: recent results by Liu *et al.* [92] show that for endocytosis by means of membrane budding both high line tensions ($> 10\ \mathrm{pN}$) and large domains are necessary. Therefore nanodomains will be stable and will not bud off.

In cells, however, additional mechanisms must be considered. To explain the absence of large domains *in vivo*, Turner *et al.* [93] make use of a continuous membrane recycling mechanism. For the membrane parameters we have determined such a mechanism predicts asymptotic domains of $\sim 10\ \mathrm{nm}$ in diameter. Our results, in combination with active membrane recycling, therefore support a minimal physical mechanism as a stabilizer for nanodomains in cells. Domains continually nucleate and grow by coalescence, but are also continually removed from the (plasma) membrane by recycling processes.

A separate effect, purely based on the elastic properties of membranes may further stabilize smaller domains *in vivo*. Domains that are not flat within the environment of the surrounding membrane may interact via membrane deformations. Such interactions are studied in the next chapter.

	σ_{d} $(10^{-7}\,\mathrm{N/m})$	κ_{d} $(10^{-19}\,\mathrm{J})$	σ_{o} $(10^{-7}\,\mathrm{N/m})$	κ_{o} $(10^{-19}\,\mathrm{J})$	τ (pN)	$\Delta\bar{\kappa}$ $(10^{-19}\,\mathrm{J})$
1	2.8 ± 0.2	2.2 ± 0.1	0.3 ± 0.3	8.0 ± 1.3	1.5 ± 0.3	2.5 ± 2
2	5.8 ± 0.5	1.8 ± 0.2	2.1 ± 0.4	8.2 ± 1.5	1.2 ± 0.4	2.0 ± 2
3	3.5 ± 0.3	2.0 ± 0.1	2.0 ± 0.5	8.2 ± 1.4	1.2 ± 0.3	2.5 ± 2
4	2.8 ± 0.2	1.9 ± 0.1	2.5 ± 0.5	8.3 ± 1.2	1.2 ± 0.4	4.0 ± 2
5	2.3 ± 0.1	1.6 ± 0.1	0.6 ± 0.3	8.0 ± 1.6	1.1 ± 0.5	4.0 ± 3

Table 4.1: Values of the material parameters for five different vesicles. The surface tensions and bending moduli of the L_{d} and L_{o} phase are determined from the fluctuation spectrum; the line tension and difference in Gaussian moduli are subsequently determined using the analytical shape model given by equations (4.7) and (4.10).

4.A Experiments

The experimental data given in chapters 4, 5, and 6 were obtained by S. Semrau from the Leiden experimental biophysics group, and are used here with permission. In this appendix we briefly sketch the experimental procedure for obtaining the experimental data shown in figures 1.3, 4.1, 4.3, 4.4, 5.1, 5.2, 5.3, 5.6, 5.7, 5.8, 5.9 and 6.3. More details can be found in [43] and [71].

Giant unilamellar vesicles (GUVs) were produced from a mixture of $30\ \%$ DOPC, $50\ \%$ brain sphingomyelin, and $20\ \%$ cholesterol at $55°\mathrm{C}$. The L_{d} phase was stained by a small amount of Rhodamine-DOPE ($0.2\ \% - 0.4\ \%$), the L_{o} phase with a small amount ($0.2\ \% - 0.4\ \%$) of perylene. In the experimental results of chapter 4, the osmotic pressure on the inside and the outside of the GUVs was identical. In chapters 5 and 6, the partial budding of domains was stimulated by increasing the osmolarity on the outside of the vesicles by $40 - 50\ \mathrm{mM}$. In both cases, lowering the temperature to $20°\mathrm{C}$ resulted in the spontaneous nucleation of L_{o} domains in a L_{d} matrix. We observed that unbudded domains quickly merged to large ones, resulting in a vesicle exhibiting complete phase separation. An example of the raw data of such a vesicle is shown in figure 4.1. In contrast, partially budded domains posses long term stability (time scale of hours). A typical example of the dynamics of these domains is given in movie S1 of [71].

4.B Membrane fluctuations

In this appendix we use the Canham-Helfrich free energy functional (2.78) introduced in chapter 2 to derive the general expression for the fluctuations of a membrane patch based. We subsequently sketch how to obtain the expres-

sion for the fluctuation spectrum (4.11) of our phase-separated vesicle from this general expression. A detailed derivation of equation (4.11) can be found in [43, Chapter 2].

4.B.1 Fluctuations of a periodic membrane patch

From the Canham-Helfrich energy functional (2.78) introduced in chapter 2 it is a straightforward exercise to calculate the fluctuations of a flat piece of fluid membrane. This calculation is originally due to Helfrich [94] and can be found in detail in many textbooks, for instance Boal [95] or Chaikin and Lubensky [72]. We parametrize our flat piece of membrane using the Monge gauge introduced in section 2.3.1 and write $\vec{r} = (x, y, h(x, y))$, with $h(x, y)$ the height function in the z-coordinate. To lowest order in derivatives of h we can then calculate the mean curvature H and metric determinant $\det(g)$:

$$H = -\frac{1}{2}\nabla_\perp^2 h, \tag{4.12}$$

$$\det(g) = 1 + (\nabla_\perp h)^2, \tag{4.13}$$

where $\nabla_\perp$ denotes the two-dimensional gradient operator. Because we are only looking at fluctuations, the topology is constant and hence the contribution of the Gaussian curvature to the energy can be ignored. The energy of a membrane with surface tension σ and bending modulus κ to quadratic order in derivatives of h is then given by:

$$\mathcal{E} = \int_S \left(\frac{\kappa}{2}(2H)^2 + \sigma\right) \mathrm{d}A = \frac{1}{2}\int_S \left(\kappa(\nabla_\perp^2 h)^2 + \sigma(\nabla_\perp h)^2\right) \mathrm{d}x\,\mathrm{d}y. \tag{4.14}$$

We proceed by expanding h in Fourier modes, on a square piece of membrane of size $L \times L$ with periodic boundary conditions:

$$h(\vec{x}) = \sum_{\vec{q}} h_{\vec{q}}\, e^{i\vec{q}\cdot\vec{x}}, \tag{4.15}$$

where $\vec{x} = (x, y)$, $\vec{q} = (q_x, q_y) = \frac{2\pi}{L}(l_x, l_y)$ with $l_x, l_y \in \mathbb{Z}$, and

$$h_{\vec{q}} = \frac{1}{L^2}\int_{-L/2}^{L/2} \mathrm{d}x \int_{-L/2}^{L/2} \mathrm{d}y h(\vec{x}) e^{-i\vec{q}\cdot\vec{x}}. \tag{4.16}$$

Substitution of the Fourier expansion (4.15) in the expression (4.14) for the energy gives:

$$\mathcal{E} = \frac{L^2}{2}\sum_{\vec{q}} \left[\kappa(\vec{q}\cdot\vec{q})^2 + \sigma(\vec{q}\cdot\vec{q})\right] h_{\vec{q}} h_{\vec{q}}^*, \tag{4.17}$$

where the star denotes complex conjugation. Invoking the equipartition theorem we now immediately find for the static correlation function

$$\left\langle h_{\vec{q}} h^*_{\vec{q}} \right\rangle = \frac{1}{L^2} \frac{k_B T}{\kappa(\vec{q}\cdot\vec{q})^2 + \sigma(\vec{q}\cdot\vec{q})}, \tag{4.18}$$

where the brackets denote the ensemble average, k_B Boltzmann's constant and T the temperature.

4.B.2 Fluctuations of a membrane patch on a real vesicle

There are several differences between the actual situation when measuring membrane fluctuations on a real vesicle and the assumptions behind the calculation of the fluctuation spectrum (4.18). First, because with the microscope we observe an (optical) section of the membrane (the xz-plane, see figure 4.5), we cannot measure $h(x,y)$ but only $h(x,0)$.

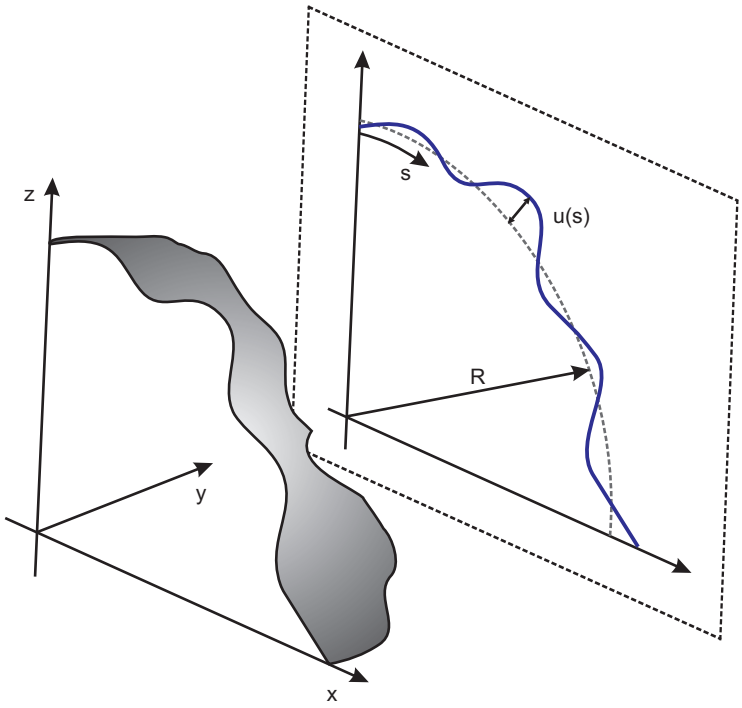

Figure 4.5: Optical section along the xz-plane, as measured in experimental observations of our vesicles. The ensemble-averaged radius is denoted by R, s is the contour length and $u(s)$ the deviation from R at s.

The Fourier components of the observable membrane profile $h(x,0)$ are given by

$$h_{q_x} = \frac{1}{L}\int_{-L/2}^{L/2} \mathrm{d}x h(x,0) e^{-iq_x\cdot x} = \sum_{q'_y} h_{(q_x,q'_y)}. \tag{4.19}$$

We can obtain the fluctuation spectrum of h_{q_x} from that of $h_{\vec{q}}$ if we convert the sum of equation (4.19) into an integral. A straightforward calculation gives:

$$\begin{aligned}\left\langle h_{q_x} h^*_{q_x}\right\rangle &= \frac{k_\mathrm{B}T}{2\pi L}\int_{-\infty}^{\infty}\mathrm{d}q_y \frac{1}{(q_x^2+q_y^2)((\sigma+\kappa q_x^2)+\kappa q_y^2)} \\ &= \frac{k_\mathrm{B}T}{2\sigma L}\left(\frac{1}{q_x} - \frac{1}{\sqrt{\frac{\sigma}{\kappa}+q_x^2}}\right).\end{aligned} \tag{4.20}$$

For tensionless membranes ($\sigma = 0$) or in the bending regime ($q_x^2 >> \sigma/\kappa$), the expression for the spectrum simplifies to

$$\left\langle h_{q_x} h^*_{q_x}\right\rangle = \frac{k_\mathrm{B}T}{4L}\frac{1}{\kappa q_x^3}. \tag{4.21}$$

The magnitude of short wavelength fluctuations thus only depends on the bending rigidity κ.

The model for the fluctuation spectrum of a flat membrane has to be adapted in two ways for the case of phase separated GUVs. We assume, as detailed above, that the vesicle is approximately spherical far away from the interface. As Pécréaux *et al.* [89] showed, for higher modes the fluctuation spectrum of a flat membrane with periodicity $L = 2\pi R$ is (numerically) the same as that of a sphere with radius R. Thus for fluctuations with short wavelengths (*i.e.*, higher modes) it does not matter that the membrane is curved on a length scale that is big compared to their wavelength. Therefore, we can in principle use the spectrum derived above, if we discard the lowest modes. However, the spherical part of the phase separated GUVs is not closed. Consequently, we have to derive the form of the spectrum for a finite membrane patch. Following [89] we choose $L = 2\pi R$ as the periodic interval and consider a patch of length a. For simplicity we choose a such that L is an integer multiple of a. We now denote the fluctuations of the contour with respect to the circle of radius R by $u(s)$, with s the arc length along the contour (see figure 4.5). Expanding $u(s)$ in Fourier modes, we have

$$u(s) = h(s,0) - R = \sum_k u_k e^{ik\cdot s}, \tag{4.22}$$

with $k = n\cdot\frac{2\pi}{a} = n\cdot m\cdot\frac{2\pi}{L}$, $n\in\mathbb{Z}$, $m\in\mathbb{N}$, and

$$u_k = \frac{1}{a}\int_{-a/2}^{a/2}\mathrm{d}s\, u(s) e^{-ik\cdot s}. \tag{4.23}$$

Following Mutz and Helfrich [88], we find for the spectrum of u_k:

$$\langle u_k u_k^* \rangle = \frac{k_B T}{2\sigma L} \sum_q \left(\frac{1}{q} - \frac{1}{\sqrt{\frac{\sigma}{\kappa} + q^2}} \right) \left[\frac{\sin\left((k-q)\frac{a}{2}\right)}{(k-q)\frac{a}{2}} \right]^2 . \tag{4.24}$$

The factor in square brackets in (4.24) goes to $\delta_{k,q}$ in the limit $a \to L$, so for $a = L$ we recover the fluctuation spectrum (4.18) of a closed sphere.

An experimental detail which further complicates the comparison of the calculated fluctuation spectrum with the experimental data, is that membrane contours are averaged over the camera integration time t (which equals the illumination time). Consequently, we observe time averaged fluctuations:

$$\overline{u(s)} = \frac{1}{t} \int_0^t \mathrm{d}t' u(s,t'). \tag{4.25}$$

To determine the influence of time averaging on the spectrum we need to know the correlation times of the fluctuation modes [89, 96]:

$$\left\langle h_{\vec{q}}(t_1) h_{\vec{q}}^*(t_2) \right\rangle = \left\langle h_{\vec{q}} h_{\vec{q}}^* \right\rangle \exp\left(-\frac{|t_1 - t_2|}{\tau_q} \right), \tag{4.26}$$

where τ_q is the correlation time, given by

$$\tau_q = \frac{4\eta|\vec{q}|}{\kappa(\vec{q}\cdot\vec{q})^2 + \sigma(\vec{q}\cdot\vec{q})}, \tag{4.27}$$

and η is the bulk viscosity of the medium surrounding the membrane. For the time-averaged spectrum we find

$$\begin{aligned} \overline{\left\langle h_{\vec{q}} h_{\vec{q}}^* \right\rangle} &= \frac{1}{t^2} \int_0^t \mathrm{d}t_1 \int_0^t \mathrm{d}t_2 \left\langle h_{\vec{q}}(t_1) h_{\vec{q}}^*(t_2) \right\rangle \\ &= \frac{k_B T}{2\eta|\vec{q}|L^2} \frac{\tau_q^3}{t^2} \left(\frac{t}{\tau_q} + e^{-t/\tau_q} - 1 \right). \end{aligned} \tag{4.28}$$

Combining equations (4.24) and (4.28), we find for the time averaged fluctuation spectrum of a finite membrane patch

$$\overline{\langle |u_k|^2 \rangle} = \sum_{q_x} \left(\frac{\sin((k-q_x)\frac{a}{2})}{(k-q_x)\frac{a}{2}} \right)^2 \frac{k_B T}{4\pi\eta L} \int_{-\infty}^{\infty} \mathrm{d}q_y \frac{\tau_q}{|\vec{q}|} \frac{\tau_q^2}{t^2} \left(\frac{t}{\tau_q} + e^{-t/\tau_q} - 1 \right). \tag{4.29}$$

4.C Finding the bulk solution

The shape of a vesicle of which the membrane is uniform in composition, and the volume is unconstrained, is given by the shape equation (4.2)

$$\ddot{\psi}\cos\psi = -\frac{1}{2}\dot{\psi}^2 \sin\psi - \frac{\cos^2\psi}{r}\dot{\psi} + \frac{\cos^2\psi + 1}{2r^2}\sin\psi. \tag{4.30}$$

If there are no boundary conditions, the solution of equation (4.30) is a sphere. Its tangent angle and radial coordinate are given by

$$\psi(s) = \frac{s}{R}, \tag{4.31}$$

$$r(s) = R\sin(\psi(s)) = R\sin\left(\frac{s}{R}\right), \tag{4.32}$$

where R is the radius of the sphere and s the arc length measured along the sphere. As explained in section 4.3, the sphere is a good approximation for those parts of a two-domain, 'snowman'-shaped vesicle which are far away from the domain boundary. However, the line tension associated with the domain boundary may cause deformations which carry into the bulk regime. To find the correct shape for the bulk part of the vesicle we should therefore allow for a perturbation of the spherical shape given by equations (4.31) and (4.32). We do so by adding a perturbation $\delta\psi$ to the tangent angle and write

$$\psi(s) = \frac{s}{R} + \delta\psi(s). \tag{4.33}$$

We assume $\delta\psi(s)$ to be small compared to ψ, and moreover, that the derivatives of $\delta\psi(s)$ with respect to s are also small, *i.e.*, of the same magnitude as $\delta\psi(s)$ itself. Because the shape equation (4.30) does not only contain derivatives of $\psi(s)$, but also its integral $r(s)$, we need to know how the perturbation affects $r(s)$ as well. To do so, we integrate the geometric relation given by (4.3): $\dot{r} = \cos\psi(s)$, and find:

$$\begin{aligned} r(s) &= R\sin(s/R) - \int_{s_0}^{s} \delta\psi(s')\sin(s'/R)\,\mathrm{d}s' + \mathcal{O}(\delta\psi^2) \\ &= R\sin(s/R) + R\Big[\delta\psi(s')\cos(s'/R)\Big]_{s'=s_0}^{s'=s} \\ &\qquad -R\int_{s_0}^{s} \delta\dot{\psi}(s')\cos(s'/R)\,\mathrm{d}s' + \mathcal{O}(\delta\psi^2) \\ &= R\sin(s/R) + R\cos(s/R)\delta\psi(s) \\ &\qquad -R\int_{s_0}^{s} \delta\dot{\psi}(s')\cos(s'/R)\,\mathrm{d}s' + \mathcal{O}(\delta\psi^2), \end{aligned} \tag{4.34}$$

where $\delta\dot{\psi}(s) = \mathrm{d}\psi(s)/\mathrm{d}s$ and s_0 is an appropriately chosen reference point. When going from the second to the third line in (4.34), we assumed $\delta\psi$ vanishes at s_0, which will set s_0 later on. Unfortunately, equation (4.34) can not be substituted directly in the shape equation (4.30) because of the integral expression. We therefore use another approach: we isolate $r(s)$ from (4.30), differentiate once with respect to s, and use (4.3) for $\dot{r}$. The resulting differential equation will give us an explicit expression for $\delta\dot{\psi}(s)$, which we can use in (4.34) to find the explicit dependence of $r(s)$ on $\delta\psi(s)$. Rewriting (4.30), and dropping

the explicit dependencies on s, we have

$$r^2(2\ddot{\psi}\cos\psi + \dot{\psi}^2\sin\psi) + r(2\cos^2\psi\dot{\psi}) - (\cos^2\psi + 1)\sin\psi = 0, \tag{4.35}$$

from which we get two solutions for $r(s)$:

$$r(s) = \frac{1}{2\ddot{\psi} + \dot{\psi}^2\tan\psi}\left(-\cos\psi\dot{\psi} \pm \sqrt{\dot{\psi}^2\sec^2\psi + 2\ddot{\psi}\tan\psi(1+\cos^2\psi)}\right). \tag{4.36}$$

We can differentiate both sides of (4.36) with respect to s. We then substitute (4.3), and expand of ψ as given in (4.31). When taking the plus sign in equation (4.36), this procedure gives:

$$\begin{aligned}
&\cos(s/R) - \sin(s/R)\delta\psi \\
&= R\frac{\mathrm{d}}{\mathrm{d}s}\Big[\sin(s/R) + \cos(s/R)\delta\psi - R\sin(s/R)\delta\dot{\psi} \\
&\qquad\qquad -R^2\sin^2(s/R)\cos(s/R)\delta\ddot{\psi}\Big] \\
&= \cos(s/R) - \sin(s/R)\delta\psi - 3R^2\sin(s/R)\cos^2(s/R)\delta\ddot{\psi} \\
&\qquad\qquad -R^3\sin^2(s/R)\cos(s/R)\delta\dddot{\psi}
\end{aligned} \tag{4.37}$$

so

$$0 = 3\cos(s/R)\delta\ddot{\psi} + R\sin(s/R)\delta\dddot{\psi}. \tag{4.38}$$

For the minus sign in (4.36), we find

$$\begin{aligned}
0 &= 2\frac{\sin(s/R)\cos(s/R)}{1+\cos^2(s/R)} - 2\sin(s/R)\delta\psi - R^2\cos^2(s/R)(4+3\sin^2(s/R))\delta\ddot{\psi} \\
&\qquad +R^3\sin(s/R)\cos(s/R)(1+\cos^2(s/R))\delta\dddot{\psi}.
\end{aligned} \tag{4.39}$$

Equation (4.39) we will not attempt to solve analytically; a numeric solution shows that the solution grows quickly and can not be considered a small perturbation to the sphere. Equation (4.38) can be integrated directly, resulting in an expression for $\delta\ddot{\psi}$:

$$\delta\ddot{\psi}(s) = A\csc^3\left(\frac{s}{R}\right), \tag{4.40}$$

with A an integration constant which has dimension $1/R^2$. Integrating again, we get

$$\delta\dot{\psi}(s) = \frac{AR}{2}\log\left[\tan\left(\frac{s}{2R}\right)\right] - \frac{AR}{2}\frac{\cos(s/R)}{\sin^2(s/R)} + b, \tag{4.41}$$

where b is another integration constant. Because the integral of b gives a term that scales with s, it gives a constant contribution to the term s/R in $\psi(s)$; we therefore set $b = 0$. A final integration gives us $\delta\psi(s)$:

$$\begin{aligned}
\delta\psi(s) &= \frac{AR^2}{2}\left[\frac{1}{\sin(s/R)} + \frac{s}{R}\log\left(\tan\left(\frac{s}{R}\right)\right)\right. \\
&\qquad \left. + i\left(\mathrm{Li}_2\left(i\tan\left(\frac{s}{2R}\right)\right) - \mathrm{Li}_2\left(-i\tan\left(\frac{s}{2R}\right)\right)\right)\right] + d,
\end{aligned} \tag{4.42}$$

with d another integration constant and $\mathrm{Li}_n(z)$ the polylogarithm (also known as Jonquière's function), defined as

$$\mathrm{Li}_n(z) = \sum_{k=1}^{\infty} \frac{z^k}{k^n}, \tag{4.43}$$

for $z \in \mathbb{C}$. The combination of the two polylogarithms in (4.42) is real for our region of interest ($-\pi R < s < \pi R$). We should choose d such that $\delta\psi(s_0) = 0$, which gives

$$d = -\frac{AR^2}{2}(1 - 2K) \tag{4.44}$$

where K is Catalan's constant, with numerical value ~ 0.91596559.

Having found expressions for $\delta\psi(s)$ and $\delta\dot{\psi}(s)$, we can use (4.34) to find $r(s)$. Using equation (4.41), the integral in (4.34) can be evaluated exactly:

$$\begin{aligned} r(s) \quad = \quad & R\sin(s/R) + R\cos(s/R)\delta\psi(s) \\ & -\frac{AR^3}{2}\left[\cot(s/R) + \log\left(\tan\left(\frac{s}{2R}\right)\right)\sin(s/R)\right]. \end{aligned} \tag{4.45}$$

Because we work with an angular coordinate, there is a coordinate singularity at the poles of the vesicle, causing a divergence in $\delta\psi(s)$. This divergence is unphysical, and can be avoided by choosing s_0 at any point away from the pole. The easiest choice is to take $\psi(s_0) = \pi/2$ (top domain), *i.e.*, at the equator of the domain, and analogously for the bottom domain. Continuity of $r(s)$, $\psi(s)$ and $\dot{\psi}(s)$ at $s = s_0$ then hold for the expressions given by (4.45), (4.42) and (4.41).

CHAPTER 5

MEMBRANE MEDIATED INTERACTIONS

The organization of the membrane in a living cell is the result of the collective effect of many driving forces. Several of these, such as electrostatic and Van der Waals forces, have been identified and studied in detail. In this chapter we investigate and quantify another force, the interaction between inclusions via deformations of the membrane shape. For electrically neutral systems, this interaction is the dominant organizing force. We use the domains in phase separated ternary vesicles as probes to study membrane mediated interactions. Once domains partially bud out from the mother vesicle, they deform their surroundings and start interacting. We show that this partial budding can only occur in a stretched membrane, where the vesicle surface is in the elastic regime. The membrane mediated interactions that appear as a consequence of this partial budding process, lead to a kinetically arrested state in which coarsening is significantly slowed down. Consequently, we find that long range order and a preferred domain size naturally appear in our system. We quantify the interactions between the domains, both in experiments and in the context of our theoretical model, and obtain the domain size distributions from Monte Carlo simulations.

5.1 Introduction

As described in chapter 3, a ternary vesicle below its critical temperature will quickly nucleate domains of one (typically L_o) liquid phase in a background of another phase (typically L_d). When there is no pressure gradient across the membrane, the vesicle as a whole is spherical and the nucleated domains can freely diffuse on its surface. They grow by coalescing, and relatively quickly all merge into one large domain. Allowing the vesicle to relax its enclosed volume (by waiting for several days or even weeks), the resulting shape is the 'snowman' we studied in chapter 4. This equilibrium shape can be understood as a trade-off between the elastic energy of the membrane and the line tension on the domain boundary.

When we put a pressure gradient across the membrane before quenching the vesicle below its critical temperature, the dynamics and resulting shape are quite different. Because the vesicle very quickly reduces its enclosed volume in order to counter the pressure gradient, there is some excess membrane area compared to the pressure-neutral case. Domains that have grown beyond a certain minimal size (set by the *invagination length* ξ [69], the ratio of the bending modulus and the line tension), can gain free energy by partially budding out from the vesicle, reducing the length of their domain boundary. The energy due to the line tension term then gets reduced, but the elastic bending energy increases, suggesting another trade-off equilibrium. However, as Lipowsky already showed [69], a model with just these two ingredients results in either no budding at all for weak line tensions, or complete budding for strong line tensions. We study this system in section 5.3 and show that partial budding can be explained by including the energy contribution due to membrane stretching.

Domains that partially bud do not only deform themselves, but also the membrane around them. Such deformations lead to an effective interaction between the domains through the differential curvature they impart. These membrane-mediated interactions have recently attracted the attention of several groups [97–104]. They turn out to be repulsive between like inclusions, and lead to the formation of kinetically arrested patterns of domains [6, 105, 106]. Vesicles with such patterns of domains are said to exhibit microphase separation: the domains are phase separated, but the vesicle as a whole is not. Microphase separation is a metastable state (the ground state is still the fully phase-separated vesicle of chapter 4), however, it persists for biologically relevant time scales. Microphase separated vesicles are moreover an ideal model system to study the interactions of other membrane inclusions such as curvature-inducing proteins [97, 99, 103, 107]. Working with domains carries two great advantages over using actual proteins. Firstly, the domains interact only through the membrane shape deformations they induce. Secondly, they are straightforward to visualize and track.

In this chapter, we study the properties of the membrane-mediated inter-

actions between many L_o domains on a L_d background in a ternary membrane vesicle. We measure the distribution of domain sizes and find a pronounced preferred length scale. By analysis of the fluctuations of domain positions we quantify the strength of membrane interactions and find a nontrivial dependence of the interaction strength on domain size. Those effects are captured qualitatively in a simple model. Our findings shed new light on intramembrane interactions between protein patches. Moreover, they also yield new information on the domain size distribution and the stability of microphase separation in multicomponent biomimetic membranes.

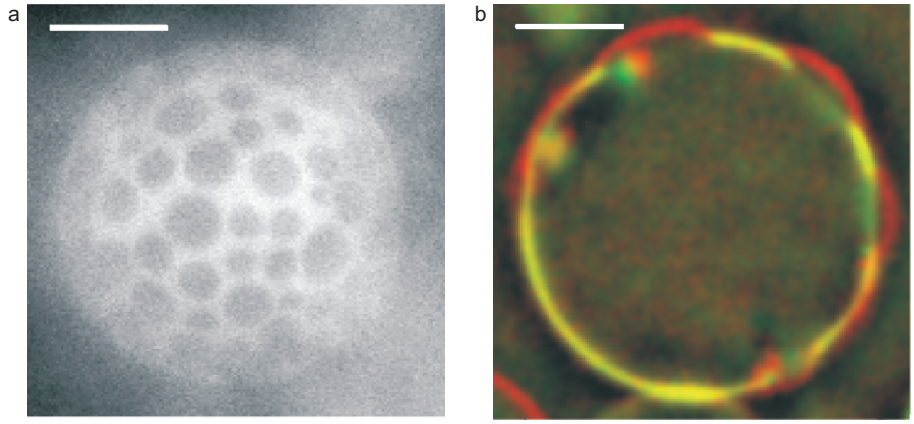

Figure 5.1: Typical example of a partially budded vesicle. (a) Complete vesicle, the L_d phase is stained and appears bright, the dark spots are L_o domains. (b) Cross-section, overlay of $405\ \mathrm{nm}$ excitation (perylene, red) and $546\ \mathrm{nm}$ excitation (rhodamine, yellow). Both scalebars: $20\ \mu\mathrm{m}$.

5.2 Evidence for interactions

The experimental data presented in this chapter is once again due to S. Semrau from the Leiden University experimental biophysics group, and used with permission; see appendix 4.A for experimental details. The experimental system considered in this chapter consists of a ternary GUV with many L_o domains in a L_d background, see figure 5.1a. After preparation by means of electroformation the vesicles have a spherical shape. By increasing the osmotic pressure outside the vesicle we produce a slight increase in surface to volume ratio. For this reason some of the vesicles show partially budded L_o domains, see figure 5.1b. Those domains posses long term stability (see Movie S1 of [71]; in experiments we observed stability on the time scale of several hours). In con-

trast, 'flat' domains, which have the same curvature as the vesicle as a whole, rapidly fuse until complete phase separation is attained [70, 106].

The stability of the vesicles with budded domains indicates that the domains experience a repulsive interaction that prevents them from merging. This interaction also affects the distribution of domain distances (radial distribution function) and domain sizes.

5.2.1 Radial distribution function

Figure 5.2 shows the radial distribution function (rdf) of the center-to-center distance of domains for a typical vesicle. The rdf gives the probability of finding a domain a distance d away from an arbitrary chosen central domain. The first (and highest) maximum in the rdf corresponds to the first coordination shell, *i.e.*, the nearest neighbors. The distance between nearest neighbors is denoted by a. On average $a = 9\ \mu\mathrm{m}$, while the radius of a domain is on average $3\ \mu\mathrm{m}$ and the vesicle radius equals $34\ \mu\mathrm{m}$ on average. Figure 5.2 clearly shows two additional maxima roughly at $2a$ and $3a$ which correspond to the second and third coordination shell. The rdf therefore indicates that the domains are not randomly distributed, but that instead their positions are correlated. Consequently the system of diffusing domains can be characterized as a two-dimensional liquid with interactions. Since a exceeds the typical domain radius by a factor of 3, this interaction is different from mere hard core repulsion between the domains.

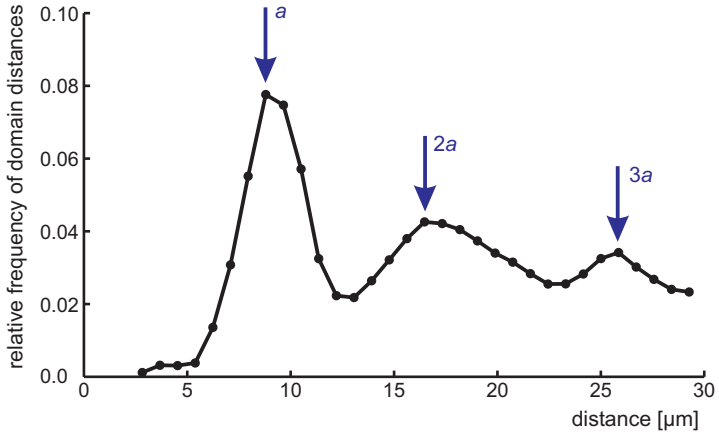

Figure 5.2: Typical radial distribution function for the center-center distances of the domains on a single vesicle. The nearest neighbor distance is denoted by a.

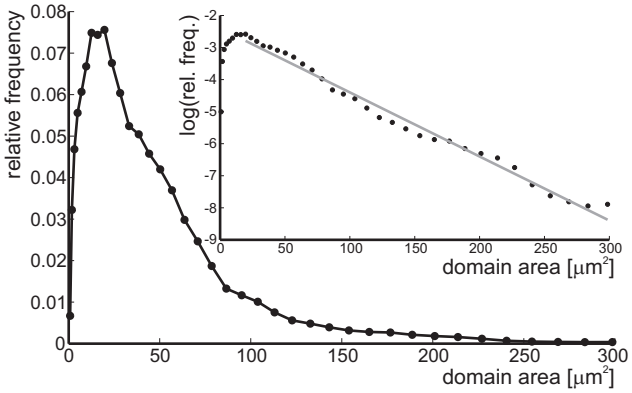

Figure 5.3: Distribution of domain sizes on all 24 vesicles. Inset: a logarithmic plot of the domain size distribution shows that it exhibits an exponential decay towards large domains (solid line).

5.2.2 Size distribution

Figure 5.3 shows the combined domain size distribution of all observed vesicles. The distribution is not uniform, but instead shows an absolute maximum, corresponding to a preferred domain size. Moreover, there is a long tail to larger domain sizes which drops off exponentially, as can be seen in a logscale plot (figure 5.3 inset). This nonuniform distribution can be understood in a picture that includes both domain fusions and domain interactions.

As was already reported by Yanagisawa *et al.* [106], we find that domains fuse when they are small. However, due to the repulsive interaction, which increases in strength when domains grow larger, the fusion of domains becomes kinetically hindered and slows down significantly with increasing domain size. When the repulsive interaction has grown to the size of the thermal energy ($k_{\mathrm{B}}T$), the fusion process has slowed down considerably and the vesicle with multiple domains enters the metastable, kinetically arrested state which we observe in the experiments.

The exponential tail we find in the domain size distribution is a direct consequence of the finite total domain area. We expect to find such a tail both with and without interactions between the domains, as can be easily seen from a simple master equation description of the system (see appendix 5.A). We note that the master equation approach breaks down when the total number of domains becomes small, but since the experimental vesicles typically have several hundreds of domains, we are well within the validity range of this description. Without interactions between the domains, we find that the distribution of domain sizes is purely exponential and decays quickly, until ultimately a

single domain remains. In the experimental data shown in figure 5.3 however, there is a distinct peak in the distribution around domains of about $25\ \mu\mathrm{m}^2$ in area, or $3\ \mu\mathrm{m}$ in radius. Moreover, the distribution remains stable on timescales much longer than it takes for flat domains to all merge. Both these observations suggest the presence of a repulsive force between the domains, hindering their fusion. To verify the claim that such a repulsion gives the observed size distribution, we performed Monte Carlo simulations of domain coalescence. The details of these simulations are given in appendix 5.B. The results of the simulations, both with and without interactions between the domains, are plotted in figure 5.4. As expected, the exponential tail in the domain size distribution is reproduced by both simulations. However, the absolute maximum in the experimental data is only reproduced in the simulations which include an interaction between the domains. Moreover, when interactions are present, we find that at $T_{\mathrm{MC}} \approx 175$ phase separation is still not complete. This relaxation time is much longer than the time we found for complete phase separation in the case without interactions ($T_{\mathrm{MC}} \approx 2$). The Monte Carlo simulations therefore show that microphase separation is a quasistatic case which can be explained by assuming a repulsive force between the domains.

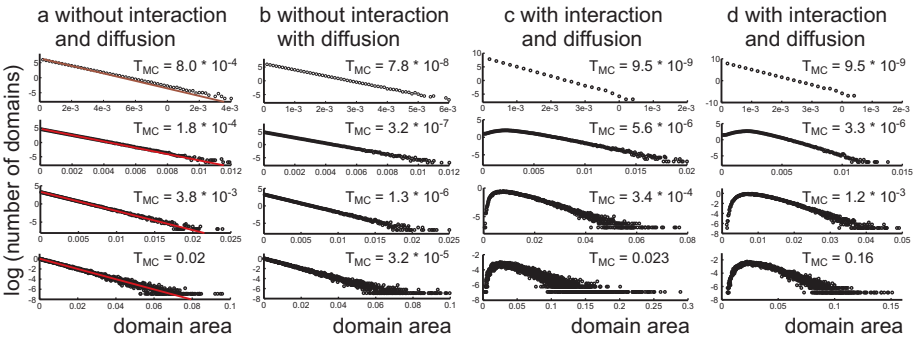

Figure 5.4: Domain size distributions determined using Monte Carlo simulations. All plots show the distribution for four different Monte Carlo times averaged over 1000 simulation runs (open circles). The initial condition is a random distribution of 10^4 domains of area $\varepsilon = 10^{-4}$. (a) Simulation without interactions and without diffusion. The gray line shows an exponential fit. (b) Simulation without interactions but including diffusion of domains. (c) Simulation including both domain diffusion and interactions; here $p_{i,j}^{\mathrm{merge}} = 10^{-6}/\sqrt{i*j}$. (d) Simulation including both domain diffusion and interactions; here $p_{i,j}^{\mathrm{merge}} = 10^{-6}/(i*j)$.

5.3 Domain budding

The experimentally observed distributions of domain distances and sizes can be explained by a repulsive membrane mediated interaction between the domains. Domains that partially bud out from the vesicle locally deform the membrane around them. Placing two budded domains close together causes this deformation to be larger, carrying a larger energy and resulting in an effective force between them. This membrane mediated force is therefore a direct consequence of the fact that the domains *partially* bud out from the vesicle. In this section we analyze the energetics of this partial budding process.

The first systematic study of domain budding was performed by Lipowsky in 1992 [69]. He modeled the domains as either circular disks in, or spherical caps on, a flat background. Domain budding is then a consequence of a tradeoff between two competing forces, which we will treat here in a coarse-grained, mean-field manner. For a more detailed view on the microscopic processes involved we refer to reviews by Lipowsky *et al.* [108] and Seifert [109]. The first force is the line tension between the L_o domain and the L_d background, which favors budding because it reduces the length of the domain boundary. On the other hand the bending energy of the L_o domain resists budding because a budded domain has a higher curvature. Lipowsky found that there is a critical domain size at which there is a transition between an unbudded state and a fully budded domain. This lengthscale is called the *invagination length*, given by $\xi = \kappa_\mathrm{o}/\tau$, with κ_o the bending modulus of the L_o phase and τ the line tension on the domain boundary; in our experimental vesicles we have $\kappa_\mathrm{o} \sim 8.0 \cdot 10^{-19}$ J and $\tau \sim 1.2$ pN, giving $\xi \sim 0.7\,\mu$m (see chapter 4). The invagination length therefore sets the length scale at which we expect to find the first occurrence of domain budding. Although we occasionally see domains splitting off from the vesicle completely, we mostly observe partially budded domains. In the model proposed by Lipowsky partial budding is not possible, suggesting that we need to consider additional constraints on, for example, the vesicle area and volume, and/or additional energy contributions. Such constraints were also studied by Jülicher and Lipowsky [52, 82]. They used numerical methods to find the minimal-energy shape of a L_d vesicle with a single L_o domain. Their results confirm the finding by Lipowsky that there is a critical domain size for budding. Moreover, they found that a constraint on the volume of the vesicle only changes the budding point but does not modify the qualitative budding behavior. In the following we show that it is not sufficient to just include area and volume constraints to explain the shape of our experimental vesicles. If we also allow for stretching of the membrane, we do get the partially budded vesicle shapes.

In general, the equilibrium shape of the membrane of a GUV is found by minimizing the associated shape energy functional under appropriate constraints on the total membrane area and enclosed volume, as explained in detail in section 2.3.5. The functional is composed of several contributions,

reflecting the energy associated with the deformation of the membrane and the effect of phase separation of the different lipids into domains. The contribution due to bending of the membrane (the bending energy) is given by the Canham-Helfrich energy functional, equation (2.78):

$$\mathcal{E}_{\text{curv}} = \mathcal{E}_{\text{mean curv}} + \mathcal{E}_{\text{Gauss}} = \int_{\mathcal{M}} \left(\frac{\kappa}{2}(2H)^2 + \bar{\kappa}K \right) \mathrm{d}S. \tag{5.1}$$

Here H and K are the mean and Gaussian curvature of the membrane respectively, and κ and $\bar{\kappa}$ the bending and Gaussian moduli. Using the Gauss-Bonnet Theorem from section 2.3.4, we find that the integral over the Gaussian curvature over a continuous patch of membrane, such as one of our L_o domains or the L_d background, yields a constant bulk contribution (which we can disregard) plus a boundary term.

For a GUV with a uniform membrane, the shape that minimizes the bending energy (5.1) is found to be a sphere. If the membrane contains domains with different bending moduli κ, the sphere is no longer the optimal solution. However, within the bulk of each domain, far away from any domain boundary, the sphere is still a good approximation of the actual membrane shape (see section 4.3). For the case at hand, where we have many small and relatively stiff domains in a more flexible background, we follow Lipowsky [69] and model the small domains as spherical caps on a vesicle which also has spherical shape itself (see figure 5.5d). Although this model has the serious shortcoming that it suggests infinite curvature at the domain edge, it remains a good approximation for the overall vesicle shape, because it corresponds to the minimal-curvature solution of the shape equation on the entire vesicle except a few special points. For the special case that all domains are equal in size, we can describe them with a curvature radius R_c and opening angle θ_c, and the background sphere with its radius R_b and opening angle θ_b (see figure 5.5d). For the mean curvature energy of a system with N domains we then have

$$\mathcal{E}_{\text{mean curv}} = 4\pi\kappa_\mathrm{o} N(1-\cos\theta_c) + 4\pi\kappa_\mathrm{d}(2 - N(1-\cos\theta_b)), \tag{5.2}$$

where κ_o and κ_d are the bending moduli of the L_o and L_d phases respectively. The Gaussian curvature contribution is given by the boundary term

$$\mathcal{E}_{\text{Gauss}} = 2\pi N \Delta\bar{\kappa} \cos\theta_c, \tag{5.3}$$

with $\Delta\bar{\kappa}$ the difference in Gaussian curvature modulus between the L_o and L_d domains. As mentioned above, we model the fact that the lipids separate into two phases by assigning a line tension to the phase boundary (equation (2.102), see also section 3.4). The energy associated with that line tension τ in the spherical cap model is given by

$$\mathcal{E}_{\text{tens}} = 2\pi\tau N R_b \sin\theta_b. \tag{5.4}$$

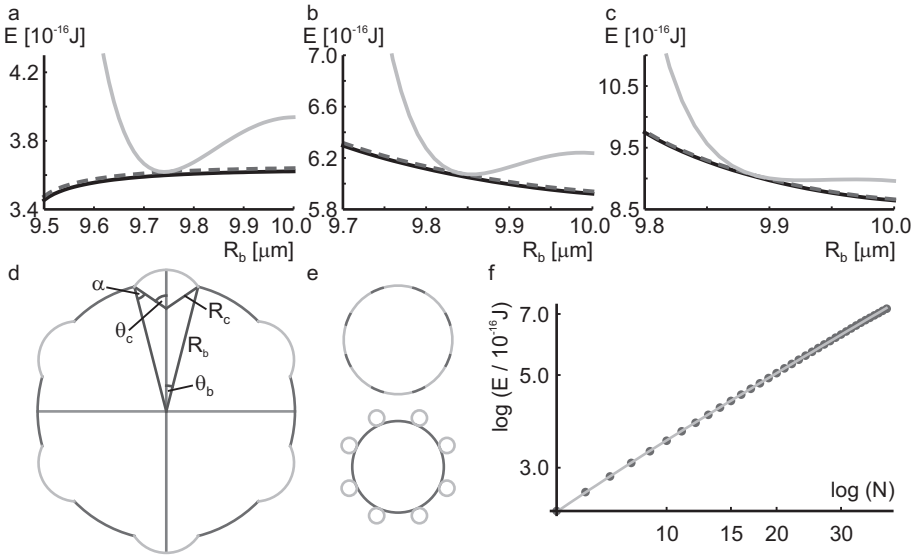

Figure 5.5: Coordinates and energy plots of the sphere-with-domains system. Energies are plotted for 10 (a), 25 (b) and 50 (c) domains as a function of the radius R_b of the background sphere. In each case the geometrical (5.5) and volume constraint (5.6) are met and the total area of the domains is fixed. The vesicles have an excess area fraction $(R_A - R_V)/R_V$ of 0.012. For the material parameters we use the values we obtained in chapter 4. The black solid line shows just the contributions of curvature and line tension; the dashed gray line those plus a surface tension term, and the gray solid line all contributions including a surface elasticity term (5.11). Without the surface elasticity term, the minimum of the energy is located at the maximum vesicle radius (figures b and c), implying flat domains (figure e top), or the minimum vesicle radius (figure a), implying full budding (figure e bottom). In the case of 50 domains the line tension energy per domain is not large enough to create buds. However, when there are only 25 domains, the line tension forces them to bud out and form spherical caps. (d) Coordinate system for the spherical caps model. (e) The two extremal situations - complete budding (bottom) and no budding at all (top). (f) Minimum of the energy (5.11) as a function of the number of domains. From the logarithmic plot shown here we find that the total energy as a function of the number of domains behaves as a power law with exponent 0.53.

If the total number N of domains is fixed, the energy given by the sum of equations (5.2), (5.3) and (5.4) is a function of four variables: R_b, R_c, θ_b, and θ_c. These variables are not independent, since they are subject to constraints. The first is that the membrane must be continuous at the domain boundary, which gives the geometric constraint

$$R_c \sin\theta_c = R_b \sin\theta_b. \tag{5.5}$$

Since the volume of the vesicle changes only over long timescales (hours) [110], we assume it is constant in our experiment (minutes), leading to a volume constraint on our system

$$\frac{4\pi}{3}\left[R_b^3 + NR_c^3(1-\cos\theta_c)^2(2+\cos\theta_c) - NR_b^3(1-\cos\theta_b)^2(2+\cos\theta_b)\right] = V_0, \tag{5.6}$$

where V_0 is the volume of the vesicle. Finally we consider the area of the vesicle. We have to treat the (total) area of the domains and that of the bulk phase separately. If we fix both of them, we obtain two additional constraints:

$$2\pi NR_c^2(1-\cos\theta_c) = A_{c,0}, \tag{5.7}$$

and

$$2\pi R_b^2(2 - N(1-\cos\theta_b)) = A_{b,0}. \tag{5.8}$$

If all four constraints given by equations (5.5)-(5.8) are imposed rigorously, the shape of the vesicle is fixed, because there were only four unknowns in the system. For an experimental system at temperature $T > 0$ however, the total area is not conserved. Thermal fluctuations cause undulations in the membrane, resulting in a larger area than the projected area given by $A_{c,0}$ and $A_{b,0}$ [111]. For $T > 0$ we should therefore not work in a fixed-area ensemble, but rather in a fixed surface-tension ensemble. We drop the constraints given by equations (5.7) and (5.8) and instead add an area energy term to the total energy

$$\mathcal{E}_{\text{area}} = 2\pi\sigma_{\text{o}}NR_c^2(1-\cos\theta_c) + 2\pi\sigma_{\text{d}}R_b^2(2 - N(1-\cos\theta_b)), \tag{5.9}$$

with σ_{o} and σ_{d} the surface tensions of the L_{o} and L_{d} phases respectively. Note that equation (5.9) can be interpreted in two ways: in the fixed area ensemble, it contains two freely adjustable Lagrange-multipliers (σ_{o} and σ_{d}) which enforce the conditions given by equations (5.7) and (5.8). In the fixed surface tension ensemble, σ_{o} and σ_{d} are set and the shape is found by minimizing the total energy with respect to the free parameters, considering the remaining geometrical and volume constraints given by equations (5.5) and (5.6). These constraints can of course be included in the total energy using Lagrange multipliers as well. This is often done for the volume constraint, and the associated Lagrange multiplier is usually identified as the pressure difference across the membrane. We stress that since we fix the total volume (*i.e.*, work in a fixed

volume ensemble), this pressure is selected by the system and is not an input parameter. The Lagrange-multiplier approach is mathematically equivalent to imposing an external volume constraint as we do here for practical purposes.

Equation (5.9) correctly gives the free energy contribution of the area energy in what is called the entropic regime, where the dominant contribution to the area term is due to the thermal fluctuations of the membrane [111]. To account for the fact that the membrane itself can be stretched or compressed away from its natural area A_0, we include a quadratic term in the area of the membrane [112]

$$\mathcal{E}_{\text{elastic}} = \gamma \left(\frac{A - A_0}{A_0} \right)^2 . \tag{5.10}$$

The elastic modulus γ is approximately 10^{-14} J in the ternary system considered here [110]. One way to understand equation (5.10) is that in the high-tension or elastic regime, the surface tension is no longer a fixed number, but itself depends linearly on the area [111]. The total shape energy is given by the sum of the five contributions given by equations (5.2), (5.3), (5.4), (5.9), and (5.10)

$$\mathcal{E} = \mathcal{E}_{\text{mean curv}} + \mathcal{E}_{\text{Gauss}} + \mathcal{E}_{\text{tens}} + \mathcal{E}_{\text{area}} + \mathcal{E}_{\text{elastic}}. \tag{5.11}$$

With the constraints (5.5) and (5.6), we are left with two independent variables for the minimization of the total energy. Since the surface tension and elastic modulus of the L_o phase are much larger than that of the L_d phase [70, 110], we further assume that the area of the L_o domains is fixed. This leaves us with a single variable minimization problem, which we solve numerically. For the material parameters we use the values we obtained in the study of the fully phase-separated vesicles in chapter 4. In order for buds to be able to form, the vesicle needs to have some excess area, which we express by the excess area fraction $(R_A - R_V)/R_V$. Here $R_A = \sqrt{A/(4\pi)}$ and $R_V = (3V/(4\pi))^{1/3}$, with A the total vesicle area and V its volume. The results of the minimization of equation (5.11) are shown in figure 5.5a-c. In the same figures we plot the energy without the membrane stretching term (5.10). In this case we find no partial budding, showing that the area elasticity term is required to reproduce the experimental results, and that our experimental vesicles are well within the elastic regime. Plotting the minima of the energy as a function of the number of budded domains on the vesicle, we find that it decreases with the number of domains (figure 5.5f). Therefore the fully phase-separated vesicle is the ground state, as we expected from the fact that the line tension is strong enough to dominate the shape.

5.4 Measuring the interactions

5.4.1 Domain position tracking

In order to determine quantitatively the interaction strength between the domains, we tracked their positions over time. In particular, we regarded situations like the one shown in figure 5.6a, in which a single domain is surrounded and held in place by a shell of 4 to 6 neighbor domains. We recorded the distance between the central domain and the center of mass of the shell domains (projected on the vesicle surface) over time and calculated the mean squared displacement (msd), see figure 5.6a for a typical example. Using only relative distances eliminates any influence of putative flow or overall movement of domains.

Although the precise form of the potential that confines the central domain is not known, we can approximate it around the local minimum by a harmonic potential $U(x) = \frac{1}{2}kx^2$ with spring constant k, where x is the distance from the center of mass of the nearest neighbors. If we treat the domain as a random walker with diffusion constant D, our model is formally equivalent to an Ornstein-Uhlenbeck process [113]. Alternatively, one can imagine all domains connected by harmonic springs. This approach also leads to an isotropic harmonic confining potential for the central domain. The msd of the domain is then given by:

$$\langle \Delta x^2(\Delta t) \rangle = \frac{4k_{\mathrm{B}}T}{k}\left[1 - \exp\left(-\frac{kD}{k_{\mathrm{B}}T}\Delta t\right)\right] \approx 4D\Delta t \quad \text{for small } \Delta t. \tag{5.12}$$

In practice, we determined the diffusion coefficient D (and a small offset due to the finite positional accuracy) from a linear fit to the first 3 time lags (see figure 5.6a), since the reliability of the data points is highest in that region. The inset of figure 5.7 shows the diffusion coefficient as a function of the size of the central domain. The other parameter of the Ornstein-Uhlenbeck model (5.12) for the msd of a domain is the spring constant k. We determined its value from a fit of equation (5.12) to the full experimental data set, where D was fixed to the value determined before. Figure 5.7 shows k normalized by the number of nearest neighbors as a function of the size of the central domain. On average $k = 1.4 \pm 0.5\, k_{\mathrm{B}}T/\mu\mathrm{m}^2$. This value supports the observation that domains are stable over extended periods of time: since the distance between domains is typically several μm the energy barrier that the domains have to overcome in order to fuse is well above $k_{\mathrm{B}}T$. Due to the limited amount of available trajectories, the error in the determination of k is fairly large. Hence it is not possible to deduce the quantitative dependence of k on the domain size. Therefore we determined k more precisely in a separate, independent way, based on domain distance statistics.

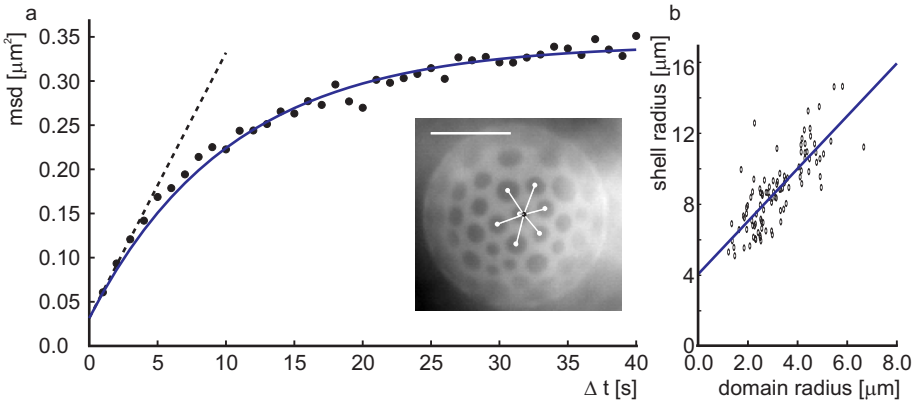

Figure 5.6: Domains caged in a shell of neighbors. (a) Typical example of the mean square displacement (msd) of the distance between a central domain and the center of mass of the surrounding domains (dots). The solid line is a fit to the Ornstein-Uhlenbeck model given by equation (5.12), the dashed line a linear fit to the first three data points, which we use to determine the diffusion coefficient. The inset shows an example of the tracking configuration. The centroids of the domains are indicated by white dots, and the center of mass of the six domains in the shell by a black dot. The distance between the centroid of the central domain and the center of mass is indicated by the gray line. The mean square displacement of this distance is used to determine the diffusional behavior of the central domain. Scalebar $20\ \mu$m. (b) Shell radius versus central domain radius, the solid line corresponds to a linear fit with slope 1.5 and offset $4.1\ \mu$m.

5.4.2 Domain distance statistics

The interaction potential between two domains can be directly inferred from the distribution of domain distances, as already demonstrated by Rozovsky *et al.* [105]. We consider a central domain surrounded by N nearest neighbors, whose combined imposed potential is given by $U(x)$. Then the probability $p(x)$ to find the central domain a distance x from the center of mass of the neighbors is proportional to the Boltzmann factor $p(x) \propto \exp\left(-\frac{U(x)}{k_B T}\right)$. As before we assume the imposed potential, at least locally, to be harmonic, $U(x) = \frac{1}{2}kx^2$, which gives for $p(x)$:

$$-\log\left(p(x)\right) = \text{const.} + \frac{1}{2}kx^2. \tag{5.13}$$

In order to determine k, we used (5.13) to fit $-\log\left(p(x)\right)$. We determined $p(x)$ from the distances of the 4 nearest neighbors of each domain, where we

binned the data according to the size of the central domain. Figure 5.8 shows an example of the distance distribution and a fit of the potential to $-\log(p(x))$.

The available data set for domain distances is much larger than the one we obtained from domain tracking. Consequently, the spring constant k can be determined with a smaller error, see figure 5.9. The average $k = 1.6 \pm 0.2\, k_B T/\mu\mathrm{m}^2$ coincides with the result found from domain tracking $k = 1.4 \pm 0.5\, k_B T/\mu\mathrm{m}^2$. Interestingly, k shows a a nonlinear behavior with a clear maximum for domains of an intermediate size which roughly coincides with the size of the most abundant domains, see figure 5.3.

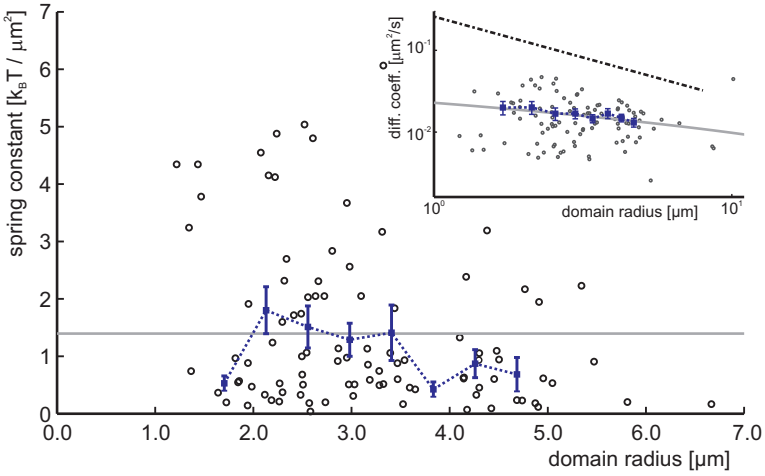

Figure 5.7: Spring constant k corrected for the number of nearest neighbors versus domain radius (circles), the squares correspond to binned data. The gray solid line marks the average $k = 1.4 \pm 0.5\, k_B T/\mu\mathrm{m}^2$. Reported error bars are standard errors of the mean. Inset: Diffusion coefficient versus domain radius (circles) for 103 trajectories. The squares represent binned data. For comparison, the dashed-dotted line gives the behavior of $D(r)\, k_B T/(16\eta r)$, which holds if the viscosity of water ($\eta \approx 10^{-3}\ \mathrm{Ns/m}^2$) is dominant [114]. The gray solid line shows a fit to the model described in [115] which gives $\eta' = 4.8 \times 10^{-8}\ \mathrm{Ns/m}$ for the 2D membrane viscosity. Reported error bars are standard errors of the mean.

5.4.3 Model for the spring constant

Due to the fact that the membrane of a GUV is both curved and finite in size, the calculation of the interaction potential between two distortions on such a membrane is a very difficult task. However, in the case where we are dealing

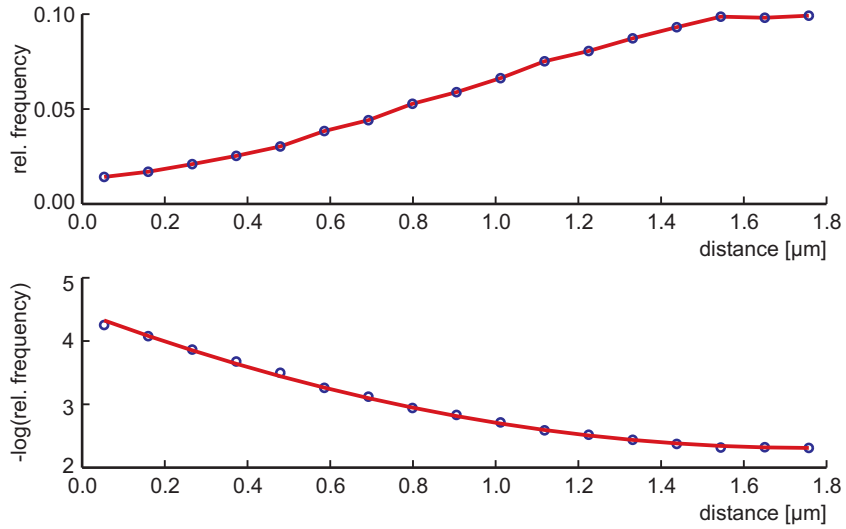

Figure 5.8: Spring constant k determined by domain distance statistics. Upper plot: relative frequency of edge-edge distances; lower plot: -log(rel. frequency) with fit to harmonic potential (solid line).

with a large number of small domains on a big vesicle the situation approaches that of domains on an infinite and asymptotically flat membrane. For two such domains with the shape of spherical caps, the interaction potential was first calculated by Goulian *et al.* [97] and reads

$$V = 4\pi\kappa(\alpha_1^2 + \alpha_2^2)\left(\frac{a}{r}\right)^4 \tag{5.14}$$

where r is the center-to-center distance between the two domains, a is a cut-off lengthscale taken to be the membrane thickness (a few nanometers), α_1 and α_2 are the domain's contact angles with the surrounding membrane (see figure 5.5d) and κ is the bending modulus of the background membrane. In appendix 5.C we give a derivation of equation (5.14), based on a calculation by Dommersnes and Fournier [99]. In order to be able to use equation (5.14) in our system, we again assume that the domains are nondeformable spherical caps. Because the ratio of the bending modulus of the L_o domains with that of the surrounding L_d membrane is significantly larger than 1 ($\kappa_o/\kappa_d \approx 4$, see chapter 4), this spherical cap approximation is valid.

As Dommersnes and Fournier showed [99], the interaction between multiple inclusions is not equal to the sum of their pairwise interactions. However, the scaling of the interaction with the distance between the domains r and the contact angles α_i does not change, only the prefactor does. For any bud-

ded domain surrounded by several other budded domains, we can therefore assume a potential of the form

$$V = \bar{C}\kappa a^4 \sum_{i=1}^{N} \frac{\alpha_0^2 + \alpha_i^2}{r_{0i}^4}, \tag{5.15}$$

where $\bar{C}$ is a numerical constant (which can be determined numerically using the method described in appendix 5.C), α_0 the contact angle of the domain we are interested in, α_i that of the ith neighbor and r_{0i} the distance between the central domain and its ith neighbor. The number of neighbors is N, which in experimental vesicles is typically 5 or 6, corresponding to a relatively dense packing of domains. Let us assume for simplicity that the equilibrium of the potential (5.15) is such that the nearest neighbors form a circle of radius r_0 around it, on which they are on average equally distributed (see figures 5.2 and 5.1a). This mean field assumption means that the central domain sees its environment as isotropic (it is not pushed in any particular direction) and its potential has a unique global minimum at the center of the circle. The energy of any displacement Δr of the central domain away from its energy minimum can then be calculated by an expansion in Δr of (5.15). The linear term in that expansion vanishes because of the isotropic distribution of the neighbors, in agreement with the assumption of the existence of a global potential minimum at $\Delta r = 0$. The first term of interest is therefore the quadratic term, which is given by

$$V_{\text{quadratic}} = \frac{C\kappa a^4}{2} \frac{\alpha_0^2 + \beta^2}{r_0^6} (\Delta r)^2, \tag{5.16}$$

where C is another constant and β the contact angle of a neighboring domain that would correspond to the time-average isotropic potential assumed above. Equation (5.16) allows us to experimentally determine the strength of the interactions between budded domains, since it yields an effective spring constant which can be measured:

$$k = C\kappa a^4 \frac{\alpha_0^2 + \beta^2}{r_0^6}. \tag{5.17}$$

In order to be able to predict the behavior of the spring constant k as a function of the domain size d (the length of its projected radius), we need to establish how α and r_0 vary with d. At present we have no way of determining $\alpha(d)$ from first principles, since that would require having a full description of the complete vesicle membrane. We can argue though that at least it should be an increasing function of d for small domains. When a domain has just grown large enough to bud out, its circumference will still be small, and the amount of membrane bending and stretching it can induce to reduce the line tension term will also be small. As the domain grows in size, this balance shifts, and by budding out further the domain makes its presence felt more strongly in

the surrounding membrane. Because in our experimental system we always consider vesicles with many small domains, we assume $\alpha(d)$ to be in the linear regime. We therefore phenomenologically write: $\alpha \propto (d - d_0)$, where d_0 is the domain size at which budding first occurs, which should be of the order of the invagination length ($0.5 - 1.0\ \mu$m, see section 5.3).

For $r_0(d)$ we do not need to make a guess, but can simply rely on experimental results, which show that r_0 depends linearly on d (figure 5.6b). Finally we will assume that $\alpha_0 \sim \beta$, since in experiments we typically find that domains are surrounded by domains of approximately equal size (see chapter 6). Using the linear dependencies of α_0 and r_0 on d in the expression for the spring constant (5.17), we find

$$k = A\frac{(d - d_0)^2}{(\bar{r}_0 + cd)^6}. \tag{5.18}$$

Equation (5.18) has two fitting parameters (A and d_0). The best fit of the experimental data is given by the dark gray solid line in figure 5.9. We find $A = 1.5 \times 10^5\ k_B T \mu\text{m}^2$ and $d_0 = 0.55\ \mu$m, which indeed is approximately the size of the invagination length ($0.7\ \mu$m). Qualitatively we find that due to the increase in repulsion strength with growing domain size the spring constant increases with domain size for small domains. For very large domains on the other hand the interdomain distance also grows, and because the interactions fall off very steeply with distance, the spring constant decreases. In between we find a maximum that corresponds to the most abundantly present domain size in the experimental vesicles.

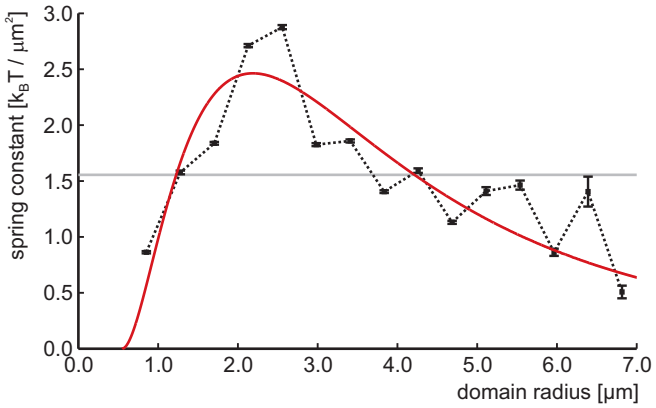

Figure 5.9: Effective spring constant k versus domain radius (circles), the squares correspond to binned data. The light gray solid line marks the average $k = 1.6 \pm 0.2\ k_B T/\mu\text{m}^2$ and the dark gray solid line the theoretical fit determined using equation (5.18).

5.5 Conclusion

The experimental results on vesicles with many domains demonstrate the existence of membrane mediated interactions between them. In this chapter we have quantified the strength of these interactions. We have shown that they originate in the curvature the domains locally impose on their environment. We have also shown that the phenomenon of partial domain budding can be explained as a competition between curvature and elastic forces on the one hand and tensile forces on the other hand. Furthermore, we found that the membrane mediated interaction influences the fusion behavior of domains, resulting in a preferred domain size. Using a simple Monte Carlo simulation we were able to reproduce the experimental domain size distribution. Finally we found that the dependence of the interaction strength on distance is consistent with existing theory, which gives a $1/r^4$ dependence.

Proteins in the membranes of living cells distort their surrounding membrane in the same fashion as lipid domains do. We therefore predict that similar membrane mediated interaction forces play a significant role in membrane structuring. Coarse grained simulations show that membrane mediated interactions can lead to the aggregation of membrane inclusions [103]. In our experiments we do not observe such attracting behavior, which suggests that our model system is more comparable to larger structures, like protein aggregates. We expect that such aggregates experience repulsive interactions if they impose a curvature on the membrane. If this curvature exceeds a certain critical size the aggregates will not be able to grow further, just like the domains stop growing after reaching a certain size. Moreover, the membrane mediated interactions have a longer range ($1/r^4$) than Van der Waals interactions ($1/r^6$) and should therefore be the dominant interaction effect in the absence of electrical charges. We therefore expect this interaction to play an important role in many biological processes.

5.A Domain growth by aggregation: master equation description

The traditional starting point for treating aggregation is the infinite set of equations that describe how the cluster size (or 'mass') distribution changes with time. They are originally due to Smoluchowski, and the master equation below is the discrete version of Smoluchowski coagulation equation [116]. 'Discrete' here refers to the domain sizes (areas), we assume the concentration $c_k(t)$ of domains with size k to be a continuous function, *i.e.*, we assume the number of domains to be large. We denote the reaction rate of domains with size i and

j by K_{ij}. The master equation for $c_k(t)$ is then given by:

$$\dot{c}_k(t) = \frac{1}{2}\sum_{i+j=k} K_{ij}c_i(t)c_j(t) - c_k(t)\sum_{i=1}^{\infty} K_{ij}c_i(t), \tag{5.19}$$

where the dot denotes a derivative with respect to time. The first term of (5.19) describes the gain in the concentration of domains of size $k = i + j$ due to the coalescence of a domain of size i with a domain of size j. The rate at which this aggregation process occurs is $K_{ij}c_i(t)c_j(t)$; the product $c_i(t)c_j(t)$ gives the rate at which the domains meet, and the reaction kernel K_{ij} is the rate at which domains actually coalesce when they encounter each other. The second (loss) term of (5.19) accounts for the loss of domains of size k due to their reaction with clusters of arbitrary size i. The prefactor of $1/2$ in the gain term ensures the correct counting of their relative contributions.

An important feature of equation (5.19) is that the total mass is conserved:

$$\sum_k k\dot{c}_k = \sum_k \sum_{i+j=k} \frac{1}{2}K_{ij}(i+j)c_ic_j - \sum_i \sum_k K_{ik}kc_ic_k = 0. \tag{5.20}$$

In the first term of (5.20), the sum over k causes the sums over i and j to become independent and unrestricted. Thus the gain and loss terms become identical and the total mass is conserved.

In the literature, exact solutions of (5.19) are known for three different kernels K_{ij}: $K_{ij} = \text{constant}$, $K_{ij} = i + j$, and $K_{ij} = ij$, or the constant, sum and product kernel respectively [116–119]. Here we will give the solution for the constant kernel (where we set $K_{ij} = 2$ for convenience). It shows that, when starting from an initial system of monomers (all domains equal in size), we arrive at an exponential distribution of domain sizes over time. For $K_{ij} = 2$, the master equation (5.19) reads

$$\dot{c}_k = \sum_{i+j=k} c_ic_j - 2c_k\sum_{i=1}^{\infty} \equiv \sum_{i+j=k} c_ic_j - 2c_kN, \tag{5.21}$$

where N is the zeroth moment of the mass distribution

$$N(t) = \sum_{i=1}^{\infty} c_i(t), \tag{5.22}$$

i.e., the concentration of clusters of any mass i. The monomer-only initial condition means that we set $c_k(t = 0) = \delta_{k,0}$. Because the master equation (5.21) for $c_k(t)$ depends only on $c_i(t)$ with $i \leq k$, we can solve these equations one by one by starting from $i = 1$, if we can determine $N(t)$ separately. To do so, we sum (5.21) over all k and find

$$\dot{N} = -N^2, \tag{5.23}$$

of which the general solution is given by

$$N(t) = \frac{N(0)}{1 + N(0)t} \to \frac{1}{t} \text{ as } t \to \infty. \tag{5.24}$$

Equation (5.24) tells us that $N(t)$ does not depend on the initial concentration $N(0)$ as $t \to \infty$. Moreover, combining equations (5.20) and (5.24), we find that in this limit the average mass of a domain grows linearly in time.

As stated, we can now progressively find $c_k(t)$ from (5.21) by substituting $N(t)$ from (5.24) and $c_i(t)$ for $i < k$ and integrating directly. Doing so, we find $c_1(t) = 1/(1+t)^2$ and $c_2(t) = t/(1+t)^3$. However, we can also solve for all $c_k(t)$ at once by rescaling (5.21). To do so, we write

$$\dot{c}_k + 2c_k N = \sum_{i+j=k} c_i c_j. \tag{5.25}$$

We introduce the integrating factor

$$I = \exp\left[2\int^t N(t')\,\mathrm{d}t'\right] = (1+t)^2, \tag{5.26}$$

and define $\phi_k = c_k I$. We also define a rescaled time variable by $\mathrm{d}x = \mathrm{d}t/I(t)$, or explicitly

$$x = \int_0^t \frac{\mathrm{d}t}{(1+t)^2} = \frac{t}{1+t}. \tag{5.27}$$

Writing (5.25) in terms of $\phi_k(x)$, we get the simple expression

$$\phi_x' = \sum_{i+j=k} \phi_i \phi_j, \tag{5.28}$$

where the prime denotes a derivative with respect to the new time variable x. Effectively we have rewritten (5.21) such that there are only gain terms. The solutions of (5.28) are given by $\phi_k = x^{k-1}$ up to a scaling factor. From the explicit solutions of $N(t)$ and $c_1(t)$ we find $\phi_1 = 1$. Using (5.26) and (5.27), we find the exact solution of (5.21)

$$c_k(t) = \frac{t^{k-1}}{(1+t)^{k+1}} \to \frac{1}{t^2} e^{-k/t} \text{ as } t \to \infty. \tag{5.29}$$

The solution (5.29) decays very quickly over time for any k, and all $c_k(t)$ in fact approach a common limit that decays as $1/t^2$ as $t \to \infty$. Moreover, for fixed time, we find that the distribution of domains decays exponentially with their size k.

5.B Monte Carlo simulations of the domain size distribution

In this appendix we study domain growth by aggregation using Monte Carlo simulations. We simulate both the case described in appendix 5.A, where domains fuse upon encounter, and the case in which the fusion rate depends on the domain sizes (or masses). For the size-independent fusion rate, equation (5.29) gives the exact solution for $c_k(t)$, the concentration of domains of size k at time t, assuming we start with a monodisperse set of domains of size 1. The exponential decay of $c_k(t)$ with k for fixed t is reproduced by the Monte Carlo simulations. When we introduce a size dependence in the fusion rate, we find that the decay time becomes much longer, and that the distribution for small sizes deviates from the exponential distribution. Since both are found in experiments, they are a clear indication that an interaction is present.

Like in appendix 5.A, we assume that the rate $k_{i,j}$ for the fusion of two domains of size (*i.e.*, area) i and j can be written as the product of two factors: the rate for random encounter by diffusion $k_{\text{diff}}(\{c_k\})$, which may depend on the distribution of domain sizes $\{c_k\}$, and the probability $p_{i,j}^{\text{merge}}$ for domain merger if the domains are close to each other:

$$k_{i,j} = p_{i,j}^{\text{merge}} k_{\text{diff}}(\{c_k\}). \tag{5.30}$$

In our simulations we start with $1/\varepsilon$ domains of size ε. During the simulation the domains are fused randomly with the rates $k_{i,j}$ given by (5.30). The fusion rate is converted to a fusion probability $p_{i,j}$ by multiplication with a small time step Δt. Since there are $\frac{1}{2}n(n-1)$ possible pairings of n domains we write the fusion probability $p_{i,j}$ as:

$$p_{i,j} = k_{i,j}\Delta t = \frac{1}{\frac{1}{2}N(N-1)} p_{i,j}^{\text{merge}} \left(\frac{1}{2}N(N-1)\right) k_{\text{diff}}(\{c_k\})\Delta t, \tag{5.31}$$

where the total number of domains is given by $N(t) = \sum_k c_k(t)$. If the time step Δt is chosen to be $\Delta t = \left[(\frac{1}{2}N(N-1))k_{\text{diff}}(\{c_k\})\right]^{-1}$, the fusion probability becomes

$$p_{i,j} = \frac{1}{\frac{1}{2}N(N-1)} p_{i,j}^{\text{merge}}. \tag{5.32}$$

The Monte Carlo algorithm we use is detailed in [120]. Briefly, in each Monte Carlo step, first a pair of domains is chosen randomly and the Monte Carlo time is increased by Δt. With a probability of $p_{i,j}^{\text{merge}}$ the domain fusion is executed.

In agreement with our experimental observations we do not allow for scission events, *i.e.*, the fission of a domain into two smaller domains. Due to the high line tension such events never occur in our experiments.

In order to take the spatial distribution and diffusion of domains into consideration, we adopt the scaling argument used in [93] and [106]. The time τ_{diff} for two domains to encounter each other at random due to diffusion scales like $\tau_{\text{diff}} \propto \langle r^2 \rangle / D(r)$, with r the domain radius and $D(r)$ the diffusion constant. Since we observe only a weak dependence of the diffusion coefficient on domain size ($D(r) \approx D$, see inset of figure 5.7), we set $k_{\text{diff}}(\{c_k\}) = \pi / \langle A \rangle$ with the average domain area $\langle A \rangle = \frac{1}{N} \sum_k k c_k$. This rate should give the correct time scale for domain fusion apart from a constant prefactor. To gauge the simulations with real experimental time scales, we let the system evolve to complete phase separation for non-interacting domains ($p_{i,j}^{\text{merge}} = 1$) and compare the resulting Monte Carlo time to measured time scales. In the case of (flat) domains, which are free to fuse, the time needed for complete separation was determined experimentally (see [106], normal coarsening) and is about 1-10 minutes. The corresponding Monte Carlo time in our simulations is $T_{\text{MC}} \approx 2$. Figure 5.4b shows intermediate domain size distributions for four different Monte Carlo times. Clearly, the exponential behavior is conserved in the presence of diffusion and the typical lengthscale of that distribution (*i.e.*, domain size) increases over time.

In the kinetic hindrance model for budded domains the probability for merger of two neighboring domains decreases with domain size. Since we do not attempt to obtain quantitative agreement with the experimental results, we can use any probability that decreases monotonically with domain size. We have performed simulations with both $p_{i,j}^{\text{merge}} = c/\sqrt{i * j}$ and $p_{i,j}^{\text{merge}} = c/(i * j)$. The results are presented in figure 5.4c and d respectively, showing intermediate domain size distributions for 4 different Monte Carlo times. The simulations reproduce the two qualitative features observed in experiments: the local maximum and the exponential tail, see figure 5.3. We find that for $T_{\text{MC}} > 100$ phase separation is still not complete. The process thus takes much longer than the time we found for complete phase separation in the case without interactions ($T_{\text{MC}} \approx 2$). The Monte Carlo simulations therefore show that microphase separation is a quasistatic state, confirming the result of section 5.3 (see also figure 5.5f).

5.C Interaction potential

For two conical inclusions (with spherical cross section), the membrane-mediated interaction potential (5.14) was first calculated by Goulian, Bruinsma, and Pincus [97], using variational calculus. Here we follow a construction by Dommersnes and Fournier [99], using an expansion in small deformations and a Green's function description, to get the potential for an arbitrary number of inclusions.

In this calculation, we assume the membrane to be infinitely large and asymptotically flat. We also assume the membrane to be uniform and tension-

less, such that the only contribution to the energy is the mean curvature term of the Canham-Helfrich energy (2.78). We assume there are only small deviations $u(x,y)$ from the (x,y) plane, and there are no overhangs, *i.e.*, $u(x,y)$ is well-defined for any point (x,y). These assumptions allow us to use the Monge gauge, in which we write $\vec{r} = (x, y, u(x,y))$. The free energy then reads in terms of u:

$$\mathcal{E} = \frac{\kappa}{2} \int \left(\nabla^2 u\right)^2 \mathrm{d}x\, \mathrm{d}y, \tag{5.33}$$

where κ as usual is the bending modulus of the membrane, and $\vec{\nabla} = (\partial_x, \partial_y)$ the differential operator on $\mathbb{R}^2$. We next put our N inclusions in the membrane at positions which we label $\vec{r}_k$, with $k = 1, \ldots, N$. The task at hand is to minimize (5.33) given the boundary conditions we thus impose at the points $\vec{r}_k$. These boundary conditions fix the local curvature tensor at $\vec{r}_k$. In the small deformation limit, the elements of that tensor are given by the second derivatives of the membrane shape, so by $\partial_{xx}u(\vec{r})$, $\partial_{xy}u(\vec{r})$ and $\partial_{yy}u(\vec{r})$. We fix the curvature constraints using $3N$ Lagrange multipliers Λ^k_{ij}. The Euler-Lagrange equations for the constrained minimization of (5.33) then read:

$$\nabla^2\nabla^2 u(\vec{r}) = \sum_{k=1}^{N} \left[\Lambda^k_{xx}\partial_{xx}\delta(\vec{r}-\vec{r}_k) + \Lambda^k_{xy}\partial_{xy}\delta(\vec{r}-\vec{r}_k) + \Lambda^k_{yy}\partial_{yy}\delta(\vec{r}-\vec{r}_k)\right], \tag{5.34}$$

with $\delta(\vec{r})$ the two-dimensional Dirac delta function. Because equation (5.34) is linear, we can write the general solution as a linear combination of derivatives of the Green's function of the operator $\nabla^2\nabla^2$. The solution is given by

$$u(\vec{r}) = \sum_{m=1}^{3N} \Lambda_m \Gamma_m(\vec{r}), \tag{5.35}$$

with

$$\Lambda = \begin{pmatrix} \Lambda^1_{xx} \\ \Lambda^1_{xy} \\ \Lambda^1_{yy} \\ \Lambda^2_{xx} \\ \vdots \end{pmatrix}, \qquad \Gamma(\vec{r}) = \begin{pmatrix} \partial_{xx}G(\vec{r}-\vec{r}_1) \\ \partial_{xy}G(\vec{r}-\vec{r}_1) \\ \partial_{yy}G(\vec{r}-\vec{r}_1) \\ \partial_{xx}G(\vec{r}-\vec{r}_2) \\ \vdots \end{pmatrix}. \tag{5.36}$$

The Green's function is given by

$$G(\vec{r}) = \frac{1}{16\pi} r^2 \log r^2, \tag{5.37}$$

with $r = |\vec{r}|$, satisfying $\nabla^2\nabla^2 G(\vec{r}) = \delta(\vec{r})$. We group the values of the $3N$

constraints in a column matrix K:

$$K = \begin{pmatrix} \partial_{xx} u(\vec{r}_1) \\ \partial_{xy} u(\vec{r}_1) \\ \partial_{yy} u(\vec{r}_1) \\ \partial_{xx} u(\vec{r}_2) \\ \vdots \end{pmatrix}. \tag{5.38}$$

The values of the Lagrange multipliers are set by the constraints in the $3N$ equations

$$\sum_{n=1}^{3N} M_{mn} \Lambda_n = K_m, \tag{5.39}$$

where M is the $3N \times 3N$ matrix

$$M = \begin{pmatrix} m_{11} & m_{12} & \cdots & m_{1N} \\ m_{21} & m_{22} & & \vdots \\ \vdots & & \ddots & \vdots \\ m_{N1} & \cdots & \cdots & m_{NN} \end{pmatrix}, \tag{5.40}$$

in which the m_{ij}'s are the 3×3 matrices given by

$$m_{ij} = \begin{pmatrix} \partial_{xxxx} G(\vec{r}_{ij}) & \partial_{xxxy} G(\vec{r}_{ij}) & \partial_{xxyy} G(\vec{r}_{ij}) \\ \partial_{xxxy} G(\vec{r}_{ij}) & \partial_{xxyy} G(\vec{r}_{ij}) & \partial_{xyyy} G(\vec{r}_{ij}) \\ \partial_{xxyy} G(\vec{r}_{ij}) & \partial_{xyyy} G(\vec{r}_{ij}) & \partial_{yyyy} G(\vec{r}_{ij}) \end{pmatrix}, \tag{5.41}$$

with $\vec{r}_{ij} = \vec{r}_i - \vec{r}_j$. Integrating equation (5.33) by parts, while taking into account the constraints (5.38), gives for the elastic energy

$$\mathcal{E} = \frac{\kappa}{2} K^T M^{-1} K, \tag{5.42}$$

where K^T is the transpose of K. From equations (5.35) and (5.39) we find for the equilibrium shape of the membrane

$$u(\vec{r}) = K^T M^{-1} \Gamma(\vec{r}). \tag{5.43}$$

To get explicit expressions, we write

$$\vec{r}_{ij} = \vec{r}_i - \vec{r}_j = r_{ij}(\cos\theta_{ij}\hat{x} + \sin\theta_{ij}\hat{y}), \tag{5.44}$$

which gives for m_{ij} in case $i \neq j$

$$m_{ij} = \frac{1}{4\pi r_{ij}^2} \begin{pmatrix} \cos(4\theta_{ij}) & \sin(2\theta_{ij}) & -\cos(4\theta_{ij}) \\ \quad -2\cos(2\theta_{ij}) & \quad \cdot(2\cos(2\theta_{ij})-1) & \\ \sin(2\theta_{ij}) & -\cos(4\theta_{ij}) & -\sin(4\theta_{ij}) \\ \quad \cdot(2\cos(2\theta_{ij})-1) & & \quad -\sin(2\theta_{ij}) \\ -\cos(4\theta_{ij}) & -\sin(4\theta_{ij}) & \cos(4\theta_{ij}) \\ & \quad -\sin(2\theta_{ij}) & \quad +2\cos(2\theta_{ij}) \end{pmatrix}. \tag{5.45}$$

For $i = j$, the expression (5.45) for m_{ij} diverges. This divergence is due to the fact that the energy (5.33) is a coarse-grained description which is only valid for distances $r \leq r_0$, with r_0 the membrane thickness. We should therefore introduce a cutoff in the theory at high wavevector of order $1/r_0$, which will allow us to calculate m_{ij} for $i = j$. To do so, we consider the derivatives of the Green's function (5.37) in Fourier space; for example

$$\partial_{xxxx} G(\vec{r}) = \frac{1}{(2\pi)^2} \int \frac{q_x^4}{q^4} e^{i\vec{q}\cdot\vec{r}} \, \mathrm{d}^2 q, \tag{5.46}$$

where $\vec{q} = (q_x, q_y)$ and $q = |\vec{q}|$. Introducing the high wavevector cutoff, we find

$$\partial_{xxxx} G(\vec{0}\,) = \frac{1}{(2\pi)^2} \int_0^{1/r_0} q \, \mathrm{d}q \int_0^{2\pi} \cos^4\theta \, \mathrm{d}\theta = \frac{3}{32\pi r_0^2}, \tag{5.47}$$

and similarly for the other matrix elements of (5.41). The entire matrix m_{ii} is given by

$$m_{ii} = \frac{1}{32\pi r_0^2} \begin{pmatrix} 3 & 0 & 1 \\ 0 & 1 & 0 \\ 1 & 0 & 3 \end{pmatrix}. \tag{5.48}$$

To recover the result by Goulian *et al.*, we consider two identical isotropic inclusions, each prescribing the curvature c. The matrix of constraints then reads

$$K^T = (c, 0, c, c, 0, c). \tag{5.49}$$

The elastic energy is now given by equation (5.42)

$$\mathcal{E} = \frac{512\pi\kappa(r_0 c)^2}{\left(\frac{R}{r_0}\right)^4 + 8\left(\frac{R}{r_0}\right)^2 - 32}, \tag{5.50}$$

where $R = r_{12}$ and we have discarded a constant term. Setting $r_0 = a/2$, and making an expansion around $R = \infty$, we find

$$\mathcal{E} = 8\pi\kappa(ac)^2 \left(\frac{a}{R}\right)^4 + \mathcal{O}\left(\frac{1}{R}\right)^6, \tag{5.51}$$

which is the result of Goulian *et al.* [97]. Using this formalism we can find the energy for any number of inclusions. The only limitation is that we have to invert the $3N \times 3N$ matrix M_{ij}. As Dommersnes and Fournier showed by an explicit calculation for a three particle system [99], the potential is not pairwise additive, however the dependence

$$V = \bar{C}\kappa a^4 \sum_{i=1}^{N} \frac{\alpha_0^2 + \alpha_i^2}{r_{0i}^4}, \tag{5.52}$$

given by equation (5.15) holds, and the constant $\bar{C}$ can be determined numerically.

CHAPTER 6

MEMBRANE MEDIATED SORTING

Inclusions in biological membranes may communicate via deformations they induce on the shape of that very membrane, a purely physical effect which is not dependent on any specific interactions. In this chapter we show that this type of interactions can organize membrane domains and proteins and hence may be significant in biological systems. Using a simple analytical model we predict that membrane inclusions sort according to the curvature they impose. We verify this prediction by both numerical simulations and by comparison to experimental observations of membrane domains in phase separated vesicles.

6.1 Introduction

In the previous chapter we studied forces between membrane inclusions mediated by the membrane itself. These forces operate on the mesoscopic scale, *i.e.*, their range is comparable to the size of a cell. Membrane mediated interactions may therefore play a role in cellular organization, alongside several well known other forces, such as hydrophobic, electrostatic and Van der Waals interactions [12]. Hydrophobic forces are responsible for creating the lipid bilayer membrane in the first place, as well as for including (trans)membrane proteins (which, like lipids, have both hydrophilic and hydrophobic parts) in it. Many highly specific protein-protein interactions are a consequence of electrostatics, which are indeed crucial to the functioning of most enzymes. However, for neutral or screened inclusions electrostatic interactions do not have long range effects, which means that long range order in the membrane stems from either Van der Waals or membrane mediated interactions. Since the first decays faster ($1/r^6$) than the second ($1/r^4$), we expect the dominant contribution to be due to forces mediated by the membrane curvature. These interactions have therefore attracted the interest of several groups over recent years [97–104]. Based on these results and the quantification of membrane mediated forces in chapter 5, we demonstrate in this chapter how membrane mediated interactions give rise to long range order in a biomimetic system. In the membranes of living cells a similar breaking of the homogeneity, by the formation of patterns and long-range order, carries significant biological implications for processes like signaling, chemotaxis, exocytosis and cell division.

We study the effect of membrane mediated interactions on domain organization and pattern formation in the same experimental system that we used in chapter 5. We consider the situation that we have many relatively small L_o domains on a vesicle with a L_d background. The domains are in a metastable, kinetically arrested state, which means they have partially budded out and no longer fuse. However, they are by no means static, but rather mobile, and reorganize continuously. Because larger domains exert a greater force on their neighbors (see section 5.4), the domains will collectively try to find a configuration in which larger domains have a larger effective area around them. We expect that, due to this size-dependent interaction, the domains demix by size to achieve an optimal configuration.

We note that this membrane mediated sorting effect is different from depletion interaction in the sense that the interaction we consider here is both long ranged and soft, whereas depletion is an effect seen in systems with hard-core repulsions. Moreover, the sorting effect occurs in a system with a continuous, polydisperse particle size distribution (see figure 5.3), severely limiting the depletion effect. Depletion may of course still play a small role, but can be ignored in comparison to the membrane mediated interactions discussed here.

In this chapter we present a simple model in which we analyze the possi-

ble distributions of domains on phase separated vesicles, and find that they exhibit a striking tendency to sort. We complement this model by performing both Monte Carlo and Brownian dynamics simulations using the membrane parameters we obtained from the shape and fluctuation fits in chapter 4. The simulations give the optimal domain distribution and show the sorting effect. We find that sorting is an unavoidable consequence of the size-dependent nature of the interactions and the finite area available on a vesicle. In addition, we compare with experimental results on phase separated, ternary vesicles, which do indeed show the sorting effect. In particular, we find a correlation between the size of a domain and the size of its neighbors, which is reproduced by our simulations.

6.2 Analytical model

A somewhat oversimplified analysis of the total energy of a fully mixed and a fully demixed system gives us a direct clue as to whether the domains segregate into regions of identical-sized ones or not. Because the bending rigidity of the L_o domains is much higher than that of the L_d background (see chapter 4), we assume the domains to be rigid inclusions, as in chapter 5. The pairwise repulsive interaction potential is therefore again given by [97]

$$V \sim \frac{\alpha^2 + \beta^2}{r^4}, \tag{6.1}$$

where α and β are the contact angles of the two inclusions or rigid domains (see figure 5.5; a derivation of (6.1) is given in appendix 5.C). Although the interactions are not pairwise additive, the qualitative dependence of V on the contact angles and inclusion distance does not change if more inclusions are added to the system [99]. It is therefore possible to use a mean-field description for a finite, closed system with many inclusions, from which the prefactor in equation (6.1) can be determined experimentally (see chapter 5). Moreover, we can write effective pairwise interactions for nearest-neighbor domains, as a function of their sizes and the distance between them.

For simplicity we look at a system with only two sizes of domains, which we will call big and small for convenience. In our model the most abundant experimental domain size (with a typical radius of $3.0\ \mu\mathrm{m}$, see figure 5.3) corresponds to the small domains. For the big domains we take a radius of $(3.0\ \mu\mathrm{m}) \cdot \sqrt{2} = 4.3\ \mu\mathrm{m}$, which means that their area is twice that of the small domains.

Let us denote the number of domains by N, the number of big domains by $N_b = \gamma N$ and that of small domains by $N_s = N - N_b = (1-\gamma)N$. Likewise we denote the contact angle of a big domain by α_b, that of a small domain by α_s, and the average contact angle of a domain's nearest neighbors (in

the mean-field approach) by β. If we neglect the small curvature of the background sphere, which has surface area A, we can associate an effective radius to each domain corresponding to the patch of area which it dominates (*i.e.*, in which it is the closest domain). In a completely mixed system the effective radius of all domains is equal and given by

$$R_{\text{eff}} = \sqrt{\frac{A}{\pi N}}. \tag{6.2}$$

In a fully mixed system each of the domains has $6 \cdot \gamma$ big and $6 \cdot (1-\gamma)$ small neighbors, which allows us to calculate the potential of that configuration in the mean field approach:

$$V_{\text{mixed}} = \frac{6}{16} N_b \frac{\alpha_b^2 + \beta^2}{A^2/(\pi^2 N^2)} + \frac{6}{16} N_s \frac{\alpha_s^2 + \beta^2}{A^2/(\pi^2 N^2)} \tag{6.3}$$

where $\beta = \gamma\alpha_b + (1-\gamma)\alpha_s$. In the fully demixed system, the big domains can take up a larger fraction ϕ of the vesicle surface than they occupy in the fully mixed system. By doing so they can increase the distance between them, reducing the interaction energy. The penalty for this reduction is a denser packing of the small domains, but since their repulsive forces are smaller, the total configuration energy can be smaller than in the mixed system. We consider the regions in which we have big and small domains separately and get two effective radii:

$$R^b_{\text{eff}} = \sqrt{\frac{\phi A}{\pi N_b}}, \tag{6.4}$$

$$R^s_{\text{eff}} = \sqrt{\frac{(1-\phi)A}{\pi N_s}}. \tag{6.5}$$

For the potential energy we obtain

$$V_{\text{demixed}} = \frac{6}{16} N_b \frac{2\alpha_b^2}{(\phi A/(\pi N_b))^2} + \frac{6}{16} N_s \frac{2\alpha_s^2}{((1-\phi)A/(\pi N_s))^2}, \tag{6.6}$$

where we have assumed the number of domains is large enough that ignoring the boundary between the two regions is justified. For a fully mixed system we would have $\phi = \gamma$, *i.e.*, the area fraction assigned to the big domains is equal to their number fraction. In the demixed system the parameter ϕ becomes freely adjustable and can be tuned to minimize the interaction energy. Comparing the demixed potential (6.6) to the mixed potential (6.3), we find

$$\begin{aligned} \frac{V_{\text{demixed}}}{V_{\text{mixed}}} &= 2\left[\frac{\gamma^3}{\phi^2}\left(\frac{\alpha_b}{\alpha_s}\right)^2 + \frac{(1-\gamma)^3}{(1-\phi)^2}\right] \\ &\quad \cdot\left[\gamma(1+\gamma)\left(\frac{\alpha_b}{\alpha_s}\right)^2 + 2\gamma(1-\gamma)\left(\frac{\alpha_b}{\alpha_s}\right) + (1-\gamma)(2-\gamma)\right]^{-1}. \end{aligned} \tag{6.7}$$

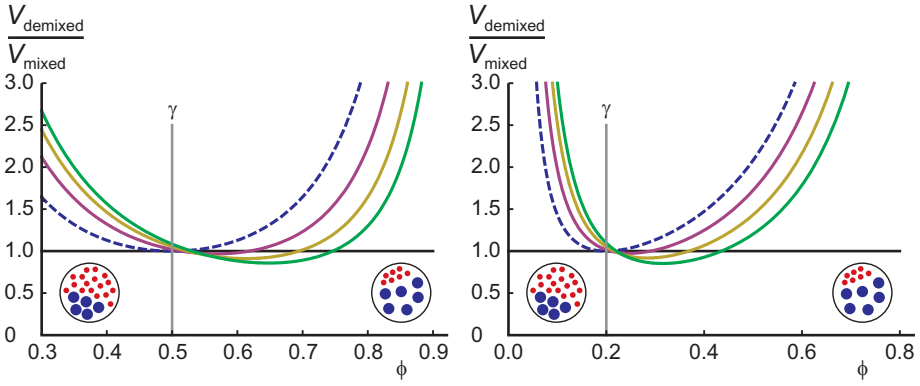

Figure 6.1: Comparison of the potential energies of the completely mixed and completely demixed state of a vesicle with domains of two different sizes. The freely adjustable parameter ϕ denotes the fraction of the vesicle's surface area claimed by the big domains. The top figure has $\gamma = \frac{1}{2}$ (equal numbers of big and small domains), and the bottom figure has $\gamma = \frac{1}{5}$ (one fifth of the domains is big). The dashed blue line indicates the case in which the big and small domains are equal in size (and hence have equal contact angles). The solid red, yellow and green lines indicate contact angle ratios α_b/α_s of 1.5, 2.0 and 2.5 respectively. Domain demixing occurs for any value of ϕ for which the potential ratio is less than 1 (black horizontal line). For comparison the number fraction γ of the big domains is indicated by the gray vertical line. Insets: typical distributions of domains for small (left) and big (right) values of ϕ. For small ϕ, the big domains are packed closely together and the small domains claim the largest area fraction, for large ϕ the situation is reversed.

Plots for several values of the parameters are given in figure 6.1. For a range of values of the adjustable parameter ϕ the energy of the demixed state is smaller than that of the mixed state; this effect becomes more pronounced as the difference in contact angle (and therefore repulsive force) increases. In the configuration which has the lowest total energy the area fraction ϕ claimed by the big domains is indeed larger than their number fraction γ.

6.3 Simulations

In the analytical model we only considered the two extreme configurations of a completely mixed and a completely demixed system. In order to be able to study also intermediate states of the system we performed Monte Carlo simulations in which we included all nearest-neighbor interactions. In these

simulations we again studied a binary system consisting of small and big domains, where the surface area of the big domains is twice that of the small ones. Starting from a random configuration of big and small L_o domains on a L_d sphere, we used Monte Carlo steps to find the energy minimum, and consistently found demixing. A typical example of a relaxation process and a configuration after 50,000 timesteps are shown in figure 6.2. The potential we used in the simulations is based on (6.1) and given by $V = V_{ij}/r^4$, with $i = 1$ for a small domain and $i = 2$ for a big one, and likewise for j. The V_{ij} values we obtained from the spring constant measurements described in chapter 5.

Complementing the Monte Carlo simulations, we also performed Brownian dynamics simulations. In these simulations, we calculate in each time step the force on each domain due to its nearest neighbors and displace it accordingly. Moreover, we add thermal fluctuations by displacing each domain a distance x over an angle θ in each timestep. The angles are sampled from a uniform distribution and the distances are sampled from the distribution $P(x) \sim \exp\left(-\frac{kx^2}{2k_BT}\right)$, where k is the effective spring constant due to the potential created by a domain's nearest neighbors (see section 5.4). In the simulations we use $k = 1.5\ k_BT/\mu\mathrm{m}^2$, corresponding to the mean value found experimentally (see figure 5.9. In the Brownian dynamics simulations, we do not just study a binary system but also a system with a more realistic exponential distribution of domain sizes (figure 5.3). Including multiple domain sizes allows for better comparison with experiment; in particular we can look for correlations between the size of a domain and its nearest neighbors. The Brownian dynamics simulations showed demixing like the Monte Carlo simulations did. An example of an obtained correlation plot is shown in figure 6.3a.

6.4 Experimental verification

Our theoretical prediction that domains segregate into regions of equal-sized ones is confirmed by experimental observations. In experiments detailed in appendix 4.A, we studied the distribution of budded domains on the entire vesicle. The vesicles we observed were lying on top of other vesicles, preventing distortion due to adhesion to the underlying coverslip. We consistently found that vesicles have regions where some domain sizes are overrepresented. An example of such an experiment is given in figure 6.3b, where two sides of the same vesicle are shown. Quantitatively we found that there is a correlation between the size of a domain and the average size of its nearest neighbors (also shown in figure 6.3b). The domain sorting occurred consistently in all 21 vesicles with budded domains we studied.

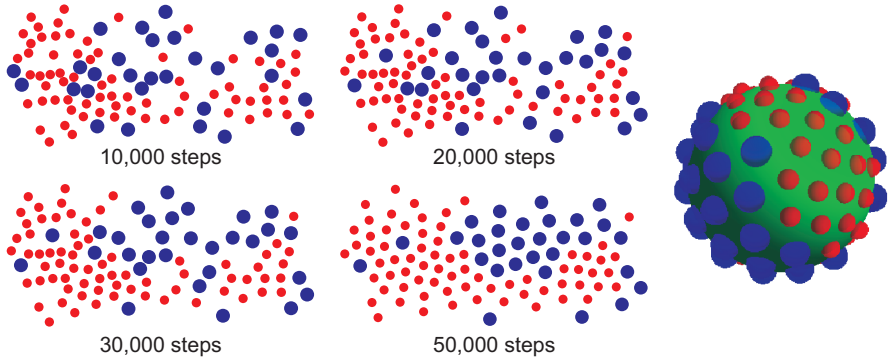

Figure 6.2: Monte Carlo relaxation of a random configuration of 70 small (red) and 30 big (blue) domains on a spherical vesicle. Left: a folded-open view of the entire vesicle, with the azimuthal angle along the horizontal direction and the polar angle along the vertical direction. The configuration is shown after 10,000 (top left), 20,000 (top right), 30,000 (bottom left) and 50,000 (bottom right) timesteps. Here $V_{12} = 3.3V_{11}$, $V_{22} = 4.5V_{11}$ and $k_{\text{B}}T = 0.25V_{11}$. Right: the configuration on a sphere after 50,000 timesteps.

6.5 Conclusion

As we have shown in this chapter, membrane mediated interactions on closed vesicles lead to the sorting of domains by size. Our analysis shows that this is due to the fact that larger domains impose a larger curvature on their surrounding membrane. We expect the same sorting effect to occur for other curvature inducing membrane inclusions, in particular cone shaped (trans)membrane proteins. This spontaneous sorting mechanism could potentially be used to create polarized soft particles. Moreover, similar sorting effects may occur in the membranes of living systems without the need of a specific interaction or an actively driven process.

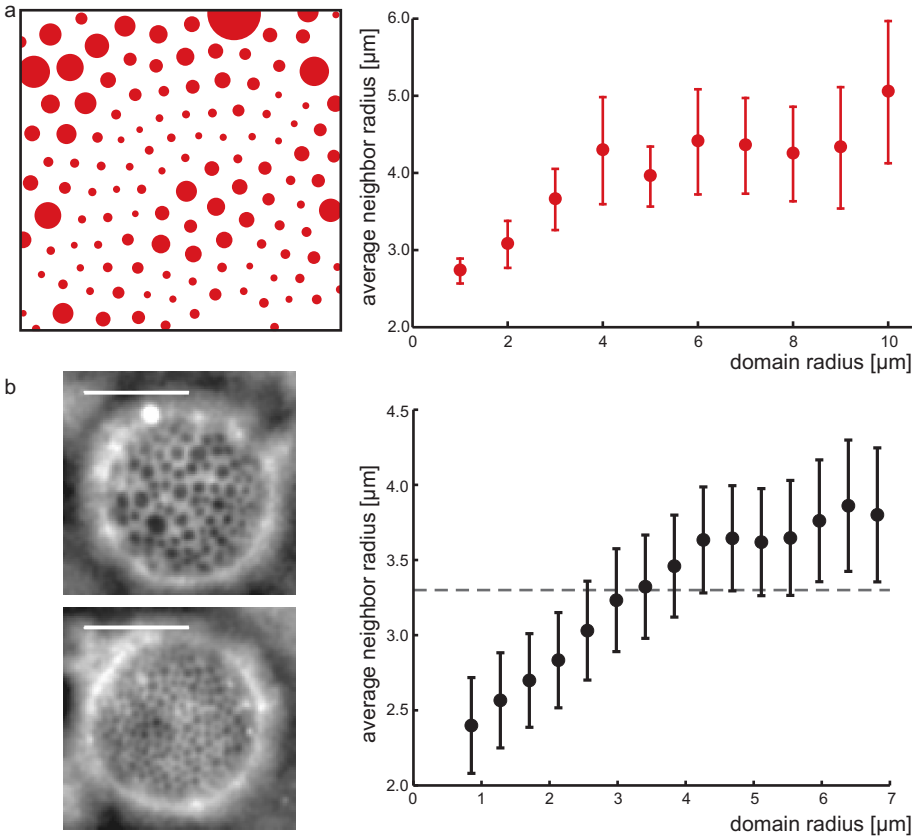

Figure 6.3: Correlations between the size of a domain and that of its nearest neighbors. (a) Results of the Brownian dynamics simulations. Left: example of the actual distribution of domains on the vesicle after 10,000 steps. Right: average correlation plot of ten Brownian dynamics simulations. Each simulation starts with 200 domains of $1.0\ \mu\mathrm{m}$ diameter. The force between two domains scales with the distance between them as $1/r^5$. The spring constant we used for the random displacements is $1.5\ k_{\mathrm{B}}T/\mu\mathrm{m}^2$. (b) Experimental data. Left: two sides of the same vesicle showing very different domain sizes; scalebar $20\ \mu\mathrm{m}$. Right: correlation plot averaged over 21 experimental vesicles; the dashed line corresponds to the average $3.3\ \mu\mathrm{m}$. Domain sizes are grouped in equally sized bins.

CHAPTER 7

TUBE PULLING BY MOLECULAR MOTORS

In cells, membrane tubes are extracted by molecular motors. Although individual motors cannot provide enough force to pull a tube, clusters of such motors can. In this chapter we use a minimal *in vitro* model system to investigate how the tube pulling process depends on fundamental properties of the motor species involved. Previously, it has been shown that processive motors can pull tubes by dynamic association at the tube tip. Remarkably, as was recently shown in experiment, nonprocessive motors can also cooperatively extract tubes. Moreover, the tubes pulled by nonprocessive motors exhibit rich dynamics as compared to those pulled by their processive counterparts. The experiments show distinct phases of persistent growth, retraction and an intermediate regime characterized by highly dynamic switching between the two. We interpret the different phases in the context of a single-species model. The model assumes only a simple motor clustering mechanism along the length of the entire tube and the presence of a length-dependent tube tension. The resulting dynamic distribution of motor clusters acts as both a velocity and distance regulator for the tube. We show the switching phase to be an attractor of the dynamics of this model, suggesting that the switching observed experimentally is a robust characteristic of nonprocessive motors. A similar system could regulate *in vivo* biological membrane networks.

7.1 Introduction

Dynamic interactions between the cell's cytoskeletal components and the lipid membranes that compartmentalize the cell interior are critical for intracellular trafficking. A trademark of these cytoskeletal-membrane interactions is the presence of continuously changing membrane tube networks. In *e.g.* the endoplasmic reticulum *in vivo* [121, 122] and in cell-free extracts [123–126], new membrane tubes are constantly formed while old ones disappear. Colocalization of these membrane tubes with the underlying cytoskeleton has led to the finding that cytoskeletal motor proteins can extract membrane tubes [126]. Motors must work collectively to extract membrane tubes [25,26,127], because the force needed to form a tube, $\mathcal{F}_{\text{tube}}$ [47], is larger than the mechanical stall force of an individual motor [128].

In this chapter we investigate how the tube pulling process depends on fundamental properties of the motors involved. We use two motor proteins from the Kinesin family [129], which walk on microtubules (MTs), the stiffest components of the cytoskeleton. As a model processive motor, we use Kinesin-1 (which we will call Kinesin for convenience), because it is the motor used *in vivo* for transport of vesicles and membrane material towards the plus end of microtubules. These processive Kinesin motors take many steps toward the plus end (to the cell periphery) before unbinding from a microtubule (MT) and have a duty ratio of approximately 1 (fraction of time spent bound to the MT) [130]. The nonprocessive motor we use is nonclaret disjunctional (Ncd), from the Kinesin-14 family, a motor protein which is highly homologous to Kinesin-1, yet fundamentally different biophysically. It is strictly non-processive: motors unbind after a single step [130] characterized by a duty ratio of 0.15 [22]. Both the Kinesin and Ncd motors are unidirectional, but they move in opposite directions. Kinesin moves towards the plus end of the MT (directed towards the plasma membrane), Ncd moves towards the minus end (directed towards the nucleus) [23]. Although Ncd is not involved in tube formation *in vivo*, it is an ideal candidate to study the effect of processivity on the tube pulling process *in vitro* because of its high similarity to Kinesin. Throughout this chapter we will therefore compare the results of pulling experiments with Kinesin and Ncd.

The bulk characteristics of molecular motors which walk on biopolymers like MTs can be studied in gliding assays [130–132]. In a gliding assay the motors are rigidly bound to a glass substrate, in such a way that the walking heads are pointing away from the glass surface. The biopolymers are then deposited on top of the substrate and their motion is followed. Typically the motors are not labeled (and thus invisible), whereas the polymers are tracked by attaching fluorescent molecules to them. Gliding assay experiments are used to measure the walking speeds of molecular motors, as a function of motor density and ATP concentration. In the specific case of Kinesin walking on microtubules, such experiments show a well-defined velocity of about $500\ \mathrm{nm/s}$, indepen-

dent of the motor concentration, which is consistent with the fact that Kinesin is highly processive. The same gliding assay with Ncd motors shows a linear dependence of MT gliding speeds on motor concentration, up to a saturation of $120\ \mathrm{nm/s}$ [133]. The linear dependence of motor concentration is a hallmark of nonprocessivity [130]. Because of their nonprocessive walking behavior, it is not *a priori* obvious that Ncd motors can cooperatively pull membrane tubes.

In the experiments described in this chapter, we study the formation of membrane tube networks pulled from Giant Unilamellar Vesicles (GUVs) by motors walking on immobilized MTs (figure 7.1a, for details see appendix 7.A). The experiments were performed by P. M. Shaklee, who has a joint position at the Leiden experimental biophysics group and at AMOLF in Amsterdam. Earlier experiments showed that using Kinesin in the same setup resulted in the formation of extended membrane tube networks [25, 26]. The key findings of the experiments with Ncd are that Ncd motors readily extract tubes, and that the tubes display more complex dynamics than those pulled by processive motors. We observed the emergence of a distinct switching behavior: the tube alternates between forward and backward movement with variable speeds, ranging from $+120\ \mathrm{nm/s}$ to $-220\ \mathrm{nm/s}$. This bidirectional switching is a phenomenon entirely absent in membrane tubes extracted by processive Kinesin motors, which proceed at constant speeds up to $400\ \mathrm{nm/s}$.

Though the bidirectional tube behavior we observe could result from motors forced to walk backward under tension [24], thus far there is no experimental evidence to support this interpretation for unidirectional motors [134, 135]. Moreover, the retraction speeds are much higher than the maximum speeds measured in Ncd gliding assays so that the reverse powerstroke would have to be much faster than the experimentally found speeds. We suggest a mechanism by which nonprocessive motors form clusters along the length of the entire tube, each of which is capable of withstanding the force due to tube tension. These clusters are dynamic entities containing a fluctuating amount of motors. The motors in the cluster at the tip of the membrane tube pull forward, until the fluctuating cluster size falls below a critical value and the tip cluster can no longer support the tube. We implement this model mathematically and show that its necessary consequence is a distinct switching behavior in membrane tubes extracted from a vesicle under tension. We analyze the experimental results in the context of this model and we predict the distribution of motor clusters all along the length of a membrane tube. The resulting dynamic distribution of motor clusters acts as both a velocity and a distance regulator for the tube. Finally, using simulations, we trace the evolution of the system and find the same bidirectional behavior as observed experimentally. In short, we show that not only can nonprocessive, unidirectional Ncd motors act cooperatively to extract membrane tubes - they do so in a highly dynamic, bidirectional switching fashion. Our findings suggest an alternative explanation for *in vivo* bidirectional tube dynamics, often credited to the presence of a mixture of plus and minus end directed motors.

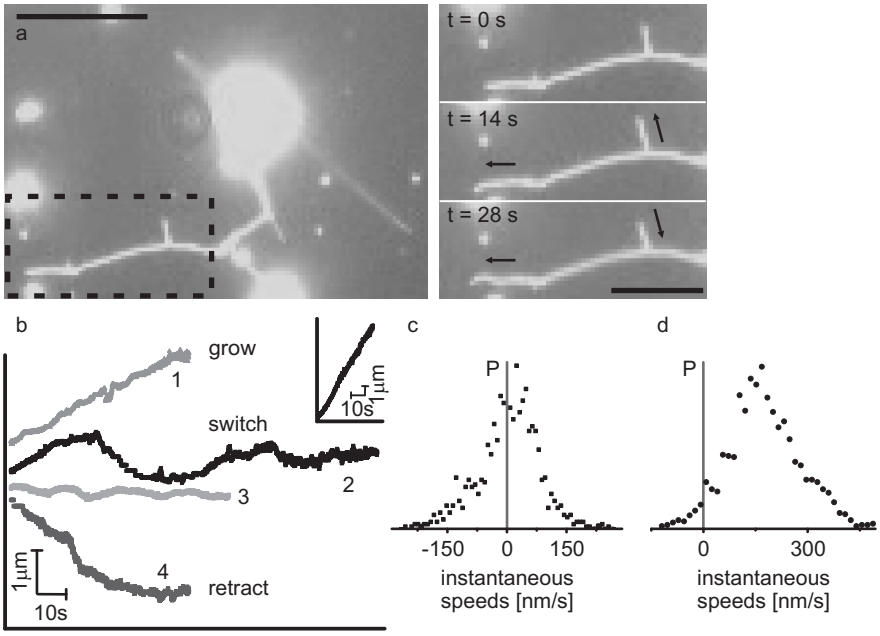

Figure 7.1: Membrane tubes formed by nonprocessive motors. (a) Fluorescence image of a membrane tube network extracted from GUVs by nonprocessive motors walking on MTs on the underlying surface. The time sequence images on the right show the detailed evolution of the network section within the dashed region on the left. The entire movie can be found in the supplementary material of [30]. Arrows indicate direction of membrane tube movement: the left arrows indicate a growing tube and the right arrows show a tube that which is switching between growth and retraction (left scalebar, $10\ \mu\mathrm{m}$, right scalebar, $5\ \mu\mathrm{m}$). (b) Example traces of membrane tube tips formed by nonprocessive motors as they move in time. There are three distinct behaviors: tube growth (1), tube retraction (4) and switching between growth and retraction (2 and 3), a bidirectional behavior. The behavior is distinctly different for membrane tubes pulled by Kinesin (inset) where tubes grow at steady high speeds. (c) The distribution of instantaneous tip speeds for membrane tubes pulled by Ncd is asymmetric and centers around zero, with both positive and negative speeds. (d) The distribution of instantaneous tip speeds for membrane tubes pulled by Kinesin is symmetric around a nonzero positive value, and does not include negative speeds.

7.2 Experimental results

The results in this section are from the experiments by P. M. Shaklee. Details on the experiments are given in appendix 7.A and [133]. We investigate the influence of motor properties on membrane tube pulling with a minimal system where biotinylated motor proteins are linked directly via streptavidin to a fraction of biotinylated lipids in GUVs. Upon sedimentation to a MT-coated surface, and addition of ATP, motors extract membrane tubes from the GUVs. These membrane tubes form networks, which follow the pattern of MTs on the substrate. Tubes and networks are formed in experiments with Kinesin motors [25] as well as in experiments with Ncd motors [30]. Figure 7.1a shows a fluorescence time series of membrane tubes pulled from a GUV by Ncd motors. The entire movie can be found in the supplementary material of [30]. The motion of the tip of a membrane tube being pulled by Ncd shows remarkable variability. The arrow on the lower right hand corner of the image of figure 7.1a indicates a retracting membrane tube and the remaining arrows show growing membrane tubes. Moreover, in the experiments we find not only tubes that persistently grow or retract, but also tubes that switch from periods of forward growth to retraction. We characterize these tube dynamics by tracing the tube tip location as it changes in time. Figure 7.1b shows example traces of Ncd-pulled membrane tube tips in time: one of tube growth, one of retraction and two that exhibit a bidirectional movement. We verify that this bidirectional tube movement is unique to nonprocessive motors by comparing to membrane tubes pulled by processive motors. Under the same experimental conditions Kinesins produce only growing tubes (figure 7.1b inset). In the rare cases of tube retraction with Kinesin, tubes snap back long distances at high speeds, at least 10 times faster than growth speeds. In these cases, it is likely that the motors pulling the tube have walked off the end of the underlying MT.

We further quantify membrane tube dynamics by calculating instantaneous speeds for individual tip traces by subtracting endpoint positions of a window moving along the trace. As described in appendix 7.A, we use a window size of $1\ \mathrm{s}$ for the Ncd, and $2\ \mathrm{s}$ for the Kinesin membrane tube tip traces. Figure 7.1c shows an example of the resulting distribution and frequency of tip speeds for a single dynamically switching membrane tube formed by Ncd (trace 2 from figure 7.1b). Figure 7.1d shows the speeds for a membrane tube pulled by Kinesin. The speed distributions for Kinesin and Ncd are distinctly different. Kinesin speeds show a Gaussian distribution around a high positive speed. From gliding assays, one expects that Kinesin would pull membrane tubes at approximately $500\ \mathrm{nm/s}$. The Kinesin motors along the bulk of the membrane tube are moving freely in a fluid lipid bilayer, do not feel any force and may walk at maximum speed toward the membrane tube tip. However, the motors at the tip experience the load of the membrane tube and their speeds are damped [25, 26, 134]. The Gaussian distribution of speeds we find for Kinesin elucidates the influence of load on the cluster of motors accumulating

at the tip of the membrane tube. The distribution of speeds for Ncd is asymmetric and centered around zero with both positive and negative speeds. A simple damping of motor walking speed at the membrane tip, as in the case of Kinesin, does not provide an explanation for the distribution of negative membrane tube speeds found in the tubes pulled by Ncd. The unique tube pulling profile of the nonprocessive motors suggests that they provide a mechanism to mediate membrane retractions and hence, bidirectional tube dynamics.

7.3 Model

Koster *et al.* [25] showed that membrane tubes can be formed as a result of motors dynamically associating at the tube tip. Collectively, the clustered motors can exert a force large enough to pull a tube. Evans *et al.* [45, 46] found that this force scales as $\mathcal{F}_{\text{tube}} \sim \sqrt{\kappa\sigma}$, where κ is the membrane bending modulus and σ the surface tension (see section 2.3.5). Koster *et al.* predicted a stable tip cluster to pull a tube, which has been verified experimentally by Leduc *et al.* [26] and supported by a microscopic model by Campàs *et al.* [28].

Although accurate for membrane tubes produced by processive motors, the Kinesin model does not explain the bidirectionality in tubes formed by nonprocessive motors. There must be an additional regulatory mechanism for the tube retractions to explain the negative speed profiles seen in experiments with Ncd. We propose a mechanism to account for these retractions wherein dynamic clusters form along the entire length of the tube. In the case of Kinesin, motors walk faster than the speed at which the tube is pulled, and accumulate at the tip cluster [25, 26]. However, in the case of Ncd the situation is completely different. Because they are nonprocessive, these motors simply can not walk to the tip of the membrane tube. Moreover, once bound, it takes a long time before they take a step and unbind again. Compared to freely diffusing motors ($D = 1\ \mu\text{m}^2/\text{s}$ [26]), a MT-bound motor (bound for approximately $0.1\ \text{s}$ [22, 136]) is therefore effectively stationary. Consequently, there are MT-bound motors all along the length of the tube. Local density fluctuations (and possibly cooperative binding [137]) lead to areas of higher concentration of bound motors, resulting in the formation of many motor clusters, not just a single cluster at the tube tip.

In both cases, the cluster present at the tip has to be large enough to overcome $\mathcal{F}_{\text{tube}}$. Because an individual motor can provide a force up to approximately $5\ \text{pN}$ [128] and a typical $\mathcal{F}_{\text{tube}}$ is $25\ \text{pN}$ [25], a cluster must consist of at least several motors to sustain tube pulling. Statistical fluctuations can make the tip cluster too small to overcome $\mathcal{F}_{\text{tube}}$, resulting in a retraction event. In the case of Ncd, as soon as the retracting tip reaches one of the clusters in the bulk, the tube is caught, and the retraction stops. Growth can then resume, or another retraction event takes place. The process of clustering along the membrane tube, as illustrated in figure 7.2, and the associated rescue mechanism

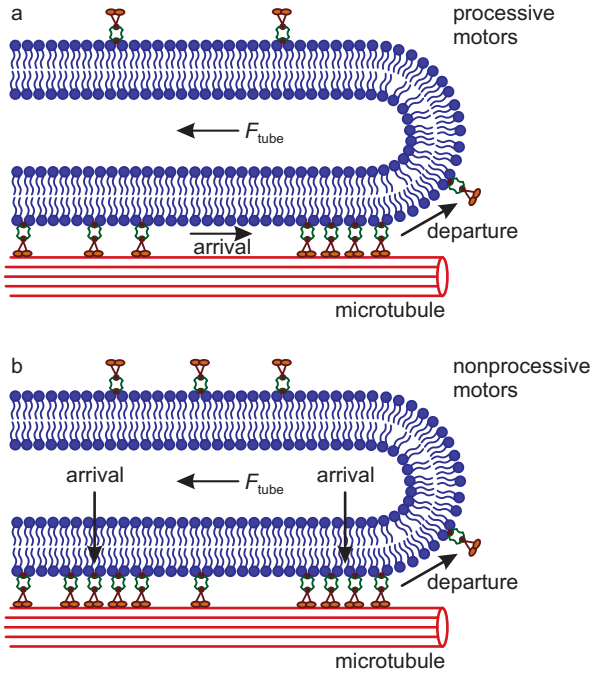

Figure 7.2: Sketch of the pulling of a membrane tube by a cluster of molecular motors. (a) Pulling by a cluster of processive Kinesin motors. Motors can bind to the microtubule anywhere along the membrane tube. Because the bound motors along the tube do not experience a load, they catch up with the cluster of motors at the tip, which thus gets replenished continuously. The only cluster is the tip cluster which pulls the tube; motors occasionally unbind from this cluster. (b) Pulling by a cluster of nonprocessive Ncd motors. Here too, motors can bind to the microtubule anywhere along the membrane tube. Since the motors can not walk continually towards the tip, they do not replenish the tip cluster. However, because Ncd motors stay bound for a long time, random density fluctuations cause clusters to appear anywhere along the membrane tube. The tip cluster can only be replenished by motors binding near or at the tip and is therefore small. If the number of motors in the tip cluster becomes too small to withstand the tube tension, a retraction event occurs, in which the tube snaps back rapidly to the next cluster.

are absent from the mechanism that describes Kinesin tube pulling. There, however, the tip cluster is typically very large (30-50 motors [25]), so fluctuations large enough to make it disappear are very rare.

In our model for pulling by Ncd motors two different mechanisms drive forward and backward tube motion, so we expect two different types of characteristic motion profiles. Retraction is regulated by motor clusters that can form anywhere along the length of the tube: their locations are randomly taken from a uniform probability distribution. Consequently the distance between them follows an exponential distribution. The long steptime of MT-bound Ncd motors allows us to temporally resolve the effect of the disappearance of clusters from the tube tip: individual retraction events. We therefore expect to recover this exponential distribution in the retraction distances.

The forward velocity depends on the size of the cluster at the tube tip, in agreement with the results from the gliding assay experiments [130]. Per experimental timestep there are many motors arriving at and departing from each cluster. Moreover, while taking a time trace we observe pulling by several different clusters of motors. Because there are many clusters in an individual trace, we can employ the Central Limit Theorem to approximate the distribution of cluster sizes by a Gaussian. If the number of motors in the tip cluster is large enough to overcome the tube force, the speed at which the cluster pulls scales with the number of excess motors: $v = A(n-c)$, up to a saturation point (typically at a cluster size of about 12 motors [130]). Here n is the number of motors, c the critical cluster size and A the scaling constant that depends on the turnover rate, stepsize and tube tension. The forward speed distribution will therefore inherit the Gaussian profile of the cluster size distribution, where the mean and spread of this distribution depend on the average tip cluster size. The probability density of the exponential distribution function depends on a single parameter λ, the mean retraction distance. The Gaussian distribution depends on both the mean $\langle n \rangle$ and the spread σ_n of the tip cluster.

The tube dynamics are described by the probability distribution of the tip displacement per unit time. From the individual probability densities for retraction and growth we find the combined density $f(\Delta L)$, the full probability density of advancing or retracting a distance ΔL:

$$f(\Delta L) = \begin{cases} (1-Z)\frac{1}{\lambda}\exp\left(-\frac{|\Delta L|}{\lambda}\right) & \Delta L < 0 \\ & \text{(retract)} \\ \frac{1}{\sigma_n\sqrt{2\pi}}\exp\left[-\frac{1}{2}\left(\frac{(\Delta L/s)-(\langle n\rangle - c)}{\sigma_n}\right)^2\right] & \Delta L \geq 0 \\ & \text{(advance)} \end{cases} \tag{7.1}$$

where n is the size of the cluster at the tip, c is the minimal cluster size necessary to support the tube, and s the steplength, which is equal to the size of a MT subunit ($8\,\mathrm{nm}$) [130]. The normalization constant Z depends on $\bar{n} = \langle n \rangle - c$

and σ_n and is given by

$$Z = \frac{1}{2}\left[1 + \mathrm{erf}\left(\frac{\bar{n}}{\sigma_n\sqrt{2}}\right)\right]. \tag{7.2}$$

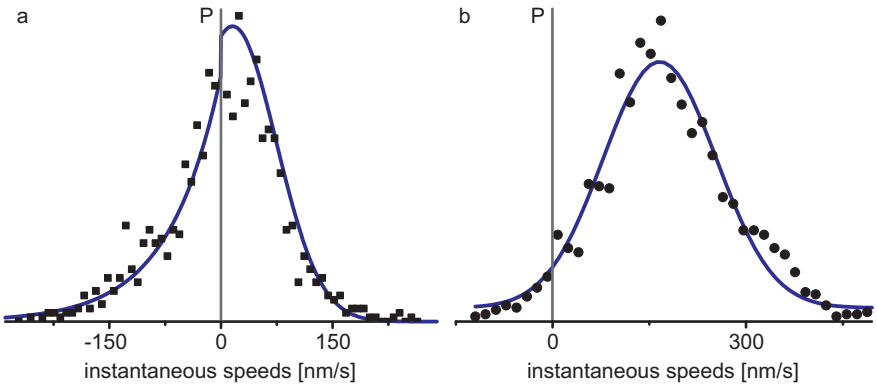

Figure 7.3: Distribution of instantaneous speeds of the tip of a membrane tube pulled by molecular motors. (a) Tip speed distribution of a tube pulled by nonprocessive Ncd motors, resulting in a a bidirectionally moving membrane tube (trace 2 in figure 7.1b). The speed distribution can be described as a combination of two different processes: pulling by nonprocessive motors and tube tension induced retraction. Therefore the forward and backward speeds follow different distributions, as described by equation (7.1); the solid line shows the best fit of this distribution. (b) Tip speed distribution of a tube pulled by processive Kinesin motors, resulting in a tube growing at constant speed (inset in figure 7.1b). The speed distribution can be described by a Gaussian (best fit shown as a solid line), indicating that there is always a cluster present at the tip to pull the tube forward.

7.4 Phase diagram

From the experimental data we cannot determine $\langle n\rangle$ and c individually, but only speed profiles which scale with the difference $\bar{n} = \langle n\rangle - c$, the number of excess motors present in the tip cluster that actually pull. To determine $A\bar{n}$, $A\sigma_n$ and λ, we make use of the fact that Z is the fraction of forward motions, providing a relation between $\bar{n}$ and σ_n. We then have a two-parameter fit for the entire speed distribution, or two single-parameter fits for the forward and backward parts of the total speed distribution.

We apply our model to experimental data and find that the different mechanisms for forward and backward motion accurately describe the experimental Ncd tip traces (figure 7.3a). As predicted, Kinesin motors only show forward pulling speeds, described by a Gaussian distribution (figure 7.3b). The marked contrast in speed profiles of processive and nonprocessive motors is a signature of different biophysical processes: for processive motors a single cluster remains at the tip ensuring a constant forward motion whereas tubes pulled by nonprocessive motors are subject to alternating growth and retraction phases.

Growth and retraction are accounted for by the two different mechanisms in our model. Combined, they explain the three different types of observed behavior: growth, retraction, and switching between these. To unravel the relationship between the two mechanisms in describing membrane tube behavior, we plot the characteristic growth rate $A\bar{n}$ versus the characteristic retraction length λ in a 'phase diagram'. Because a trace exhibiting switching behavior should have an average displacement of zero, we can derive a 'switching condition' from the probability distribution (7.1) by requiring the expectation value of ΔL to vanish. The line in the phase diagram where this switching condition is met is given by:

$$\lambda_s = A\bar{n}\frac{Z}{1-Z} + \frac{A\sigma_n}{\sqrt{2\pi}}\frac{1}{1-Z}\exp\left[-\frac{1}{2}\left(\frac{\bar{n}}{\sigma_n}\right)^2\right] \tag{7.3}$$

where Z is the normalization constant given by equation (7.2). In figure 7.4a we plot the lines for which the switching condition holds for the range of values for $A\sigma_n$ we find in the experimental traces ($50\,\mathrm{nm/s} \leq A\sigma_n \leq 70\,\mathrm{nm/s}$). We also plot the experimentally obtained values for $A\bar{n}$ and λ of the four traces given in figure 7.1b. We clearly see different regimes. Growing tubes have large average cluster size and small distances between clusters. Retracting tubes show the inverse characteristics (small cluster size and large distance between clusters). The switching tubes are in between, in a relatively narrow region.

7.5 Simulations

The switching regime covers only a small part of the total available parameter regime in the phase diagram (see figure 7.4a). That we observe switching behavior in approximately $50\ \%$ of the experimental traces indicates that these parameters are dynamic quantities that change over time. Our experimental observation times are too short to track these changes, but we can implement them in simulations. When introducing dynamics into our model, it is important to realize that the tube force $\mathcal{F}_{\text{tube}}$ is not independent of the tube length, an additional observation not yet integrated into the model. As tubes grow longer the vesicle itself starts to deform. Consequently, the tube force increases with the tube length, an effect also observed experimentally [138].

The force exerted by a single motor is constant, so a larger force requires more motors to pull at the same time for a tube to grow. A length-dependent pulling force therefore naturally leads to a typical lengthscale L_c, on which the force exerted by an average tip cluster exactly balances the force exerted by the tension in the tube. Rather than to explicitly introduce a force into our system, we model the length-dependence by rescaling the number of motors available for pulling. We do so by introducing an exponential factor that compares the length of the tube to the lengthscale L_c. The number of motors on the entire tube as a function of time is then given by

$$N(t) = C2\pi R_0 L(t) e^{-L(t)/L_c}, \tag{7.4}$$

where C is the average motor concentration on the GUV and R_0 is the tube radius.

Combined, equations (7.1) and (7.4) form a dynamical system which describes the time-dependent membrane tube behavior when pulled by nonprocessive motors. We simulate that system with values for C and R_0 from the experimental data. In the simulations, we assume that tubes are initially pulled from motor-rich regions on the GUV; this assumption is not necessary but helps to get the pulling process started, while limiting the retraction distances. As a tube grows longer, clusters are spread further apart and the average cluster size decreases. The average retraction distance increases with increasing tube length, $L(t)$, and scales inversely with the total number of motors, $N(t)$, on the tube: $\lambda \sim L(t)/N(t)$. Similarly, the average number of motors at the tip scales with the total number of motors $N(t)$ and inversely with the tube length $L(t)$: $\langle n \rangle \sim N(t)/L(t)$. We choose the simulation timestep to match the experimental sampling rate of 25 Hz. In each timestep we add Gaussian noise to the position of the tip to account for the experimental noise. In the simulations we observe two kinds of behavior: tubes that grow and subsequently retract completely after relatively short times, and tubes that evolve to a switching state. In control simulations where the exponential factor in equation (7.4) is left out, we find either fully retracting or continuously growing membrane tubes, never switching.

Figure 7.4b shows two examples of simulated switching traces. We follow the average number of motors at the tip $\langle n \rangle$ and the retraction distance λ as they change in time. The simulated evolution from growth to a switching state can be seen in the phase diagram shown in figure 7.4a. In the switching state, the tube length and total number of motors on the tube are essentially constant, and equation (7.3) is satisfied.

The highlighted sections of the simulated traces shown in figure 7.4b represent all possible characteristic behaviors of tubes pulled by nonprocessive motors. The occurrence of all three types of behavior in a long simulated tube tip trace suggests that the experimental observations are snapshots of a single evolving process. The simulations indicate that all these processes eventually move to the switching regime. The switching state is therefore a dynamic

attractor of this system. The position of the attractor in the phase diagram corresponds to a regulated tube length, determined by the GUV's motor concentration and surface tension.

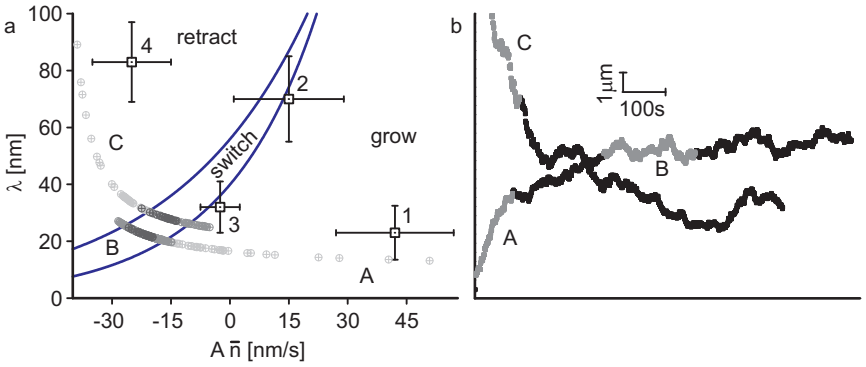

Figure 7.4: Membrane tube phase diagram and simulations. (a) Phase diagram showing mean retraction distance λ vs. effective growth speed $A\bar{n}$. Lines represent the switching condition described by equation (7.3) for $A\sigma_n = 50\ \mathrm{nm/s}$ and $A\sigma_n = 70\ \mathrm{nm/s}$. Squares 1-4 correspond to traces 1-4 in figure 7.1b, where the errors are determined by the mean square difference between the data points and the fit of distribution (7.1). As expected qualitatively, retracting membrane tubes fall well into the retraction regime with large retraction distance and small cluster sizes, while growing membrane tubes have large cluster sizes and smaller distances between clusters. (b) Two simulated tube tip traces of a membrane tube pulled by nonprocessive motors. The time evolution of the parameters λ and $A\bar{n}$ for both traces is shown in the phase diagram (a), by circles getting darker in time. We find that both simulated tubes evolve towards a switching state. The highlighted sections (A, B, C) of the simulated traces represent all possible characteristic behaviors of tubes pulled by nonprocessive motors.

7.6 Conclusion

Both processive and nonprocessive motors can collectively pull tubes from membrane vesicles. Tubes pulled by processive motors are growing at a constant speed. On the other hand, tubes pulled by nonprocessive motors exhibit a variety of speeds and even bidirectionality in their motion. Two different mechanisms are involved in producing this bidirectional behavior: pulling by motors and retraction by tension. We captured both mechanisms in a single

model. In this model motors spontaneously organize into clusters due to random fluctuations in motor density. The cluster at the tip is responsible for the forward motion and the backward motion originates from the tube retracting to the next stable motor cluster. Our model predicts the emergence of a dynamic attractor at an equilibrium tube length where bistability occurs, in agreement with the experimental observations.

7.A Experiments

The experimental data given in chapter 7 were obtained by P. M. Shaklee from the Leiden experimental biophysics group and AMOLF, and are used here with permission. In this appendix we briefly sketch the experimental procedure for obtaining the experimental data shown in figures 7.1, 7.3 and 7.4. More details can be found in [133].

The Giant Unilamellar Vesicles (GUVs) used in the tube pulling experiments consist primarily of DOPC lipids. To visualize them, a small amount of fluorescent Rhodamine lipid is included in the membrane bilayer. Moreover, to provide for binding sites for the molecular motors, a small amount of biotin lipids is included as well. GUVs are prepared in such a way that there is no osmotic pressure gradient across their membrane. After formation of the GUVs, $2\,\mathrm{mg/ml}$ streptavidin is added to 50 μl of vesicle solution. The streptavidin acts as a linker between the biotin lipids in the GUVs and the motors; the quantity of streptavidin added is chosen such that all biotin binding sites on the vesicles are saturated. Finally $2\ \mu\mathrm{l}$ of motor solution (Kinesin or Ncd, $\sim 650\ \mu\mathrm{g/ml}$) is added and incubated for 10 minutes, allowing all motors from the solution to bind to available biotin-streptavidin complexes.

Microtubules (MTs) are prepared from tubulin dimers, the MT building blocks consisting of an α and a β tubulin protein. The MTs are allowed to polymerize in a buffer solution for 15 minutes at $37^{\circ}\mathrm{C}$, and subsequently stabilized by adding $10\ \mu\mathrm{M}$ taxol protein. The solution containing the stabilized MTs is dropped on a prepared glass coverslip, where they are incubated for 10 minutes to adhere. MTs that do not stick to the surface are removed by rising twice with a buffer solution. Finally the surface is coated with α-Casein protein.

The Kinesin motors used are the first 401 residues of the Kinesin-1 heavy-chain from *Drosophila melanogaster*, with a hemaglutinin tag and a biotin at the N-terminus. To produce them, they are expressed in *Escherichia coli* and purified as described in [139]. The Ncd motors are the residues K195-K685 of the nonclaret disjunctional (Ncd) from *Drosophila melanogaster*, with a 6x-His tag [136] and biotin. They are expressed and purified in the same fashion as the Kinesins.

In the experiments $40\ \mu\mathrm{l}$ of the vesicle solution (containing GUVs with attached motors) is dropped on top of the glass coverslips decorated with the stabilized MTs. A saturating solution of $1\ \mu\mathrm{l}\ 100\ \mathrm{mM}$ ATP is added to provide

the fuel source for the motors.

Images are acquired on an epifluorescence inverted microscope equipped with a CCD camera at videorate. We developed a Matlab® algorithm to trace the membrane tube growth dynamics by following the tip displacement as a function of time. The algorithm determines the intensity profile along a tube and extended beyond the tip. A sigmoidal curve fit to the profile to determines the tip location with subpixel precision of $40\ \mathrm{nm}$. We traced tip locations for 7 individual Kinesin-pulled membrane tubes (all growing, a single one showing a rapid retraction event) and 15 Ncd tubes (5 growing, 3 retracting, and 7 switching). We calculated instantaneous speeds for individual tip traces by subtracting endpoint positions of a window moving along the trace. Initially we used a range of window sizes, from $0.5\ \mathrm{s}$ to $12\ \mathrm{s}$, to calculate instantaneous speeds from the tip traces. We found that, for the Ncd data, a window size of $1\ \mathrm{s}$ is large enough to average out experimental system noise (signal due to thermal noise, fluorophore bleaching and microscope stage drift) but small enough to preserve the unique bidirectional features we see in tube data. Windows of 2 and $3\ \mathrm{s}$ begin to overaverage the data, and even larger window sizes smooth away the prevalent changes in speeds and directionality already qualitatively evident in the data. For Kinesin, however, the resulting speeds we found using a window size of $2\ \mathrm{s}$ (minimum size for the Kinesin data, the experimental signal is noisier than for the Ncd data) differ very little from the speeds we get using up to an $8\ \mathrm{s}$ window. Ultimately, we used small window sizes that are still large enough to average out experimental noise but preserve as much of the signal details as possible: $1\ \mathrm{s}$ for Ncd tip traces and $2\ \mathrm{s}$ for Kinesin traces, with steps of $0.04\ \mathrm{s}$. We determined the noise in our system (signal due to thermal noise, fluorophore bleaching and microscope stage drift) by analyzing stationary membrane tubes with our tip-tracing algorithm and calculating instantaneous speeds in the same fashion as for active tube tips. The speeds from a noise trace showed a Gaussian profile centered around zero with a spread of $40\ \mathrm{nm/s}$.

BIBLIOGRAPHY

[1] S. Munro, Cell **115**, 377 (2003).

[2] C. Dietrich, L. A. Bagatolli, Z. N. Volovyk, N. L. Thompson, M. Levi, K. Jacobson, and E. Gratton, Biophys. J. **80**, 1417 (2001).

[3] A. V. Samsonov, I. Mihalyov, and F. S. Cohen, Biophys. J. **81**, 1486 (2001).

[4] S. L. Veatch and S. L. Keller, Phys. Rev. Lett. **89**, 268101 (2002).

[5] S. L. Veatch and S. L. Keller, Biophys. J. **85**, 3074 (2003).

[6] T. Baumgart, S. T. Hess, and W. W. Webb, Nature **425**, 821 (2003).

[7] S. L. Veatch and S. L. Keller, Phys. Rev. Lett. **94**, 148101 (2005).

[8] P. I. Kuzmin, S. A. Akimov, Y. A. Chizmadzhev, J. Zimmerberg, and F. S. Cohen, Biophys. J. **88**, 1120 (2005).

[9] S. A. Akimov, P. I. Kuzmin, J. Zimmerberg, and F. S. Cohen, Phys. Rev. E **75**, 011919 (2007).

[10] A. J. Garcia-Saez, S. Chiantia, and P. Schwille, J. Biol. Chem. **282**, 33537 (2007).

[11] D. M. Engelman, Nature **438**, 578 (2005).

[12] B. Alberts, A. Johnson, J. Lewis, M. Raff, K. Roberts, and P. Walter, *Molecular biology of the cell*, 5th ed. (Garland Science, New York, NY, U.S.A., 2008).

[13] M. Ehrlich, W. Boll, A. van Oijen, R. Hariharan, K. Chandran, M. L. Nibert, and T. Kirchhausen, Cell **118**, 591 (2004).

[14] K. Simons and E. Ikonen, Nature **387**, 569 (1997).

[15] S. J. Singer and G. L. Nicolson, Science **175**, 720 (1972).

[16] M. Edidin, Annu. Rev. Biophys. Biomol. Struct. **32**, 257 (2003).

[17] A. Lee, Biochim. Biophys. Acta, Biomembr. **1612**, 1 (2003).

[18] E. Sackmann, J. Phys.: Condens. Matter **18**, R785 (2006).

[19] E. Nogales and H.-W. Wang, Curr. Opin. Cell Biol. **18**, 179 (2006).

[20] F. Gittes, B. Mickey, J. Nettleton, and J. Howard, J. Cell Biol. **120**, 923 (1993).

[21] R. D. Vale and R. A. Milligan, Science **288**, 88 (2000).

[22] E. Pechatnikova and E. Taylor, Biophys. J. **77**, 1003 (1999).

[23] T. G. Wendt, N. Volkmann, G. Skiniotis, K. N. Goldie, J. Müller, E. Mandelkow, and A. Hoenger, EMBO J. **21**, 5969 (2002).

[24] M. Badoual, F. Jülicher, and J. Prost, Proc. Natl. Acad. Sci. USA **99**, 6696 (2002).

[25] G. Koster, M. Van Duijn, B. Hofs, and M. Dogterom, Proc. Natl. Acad. Sci. USA **100**, 15583 (2003).

[26] C. Leduc, O. Campàs, K. B. Zeldovich, A. Roux, P. Jolimaitre, L. Bourel-Bonnet, B. Goud, J.-F. Joanny, P. Bassereau, and J. Prost, Proc. Natl. Acad. Sci. USA **101**, 17096 (2004).

[27] S. Klumpp and R. Lipowsky, Proc. Natl. Acad. Sci. USA **102**, 17284 (2005).

[28] O. Campàs, Y. Kafri, K. B. Zeldovich, J. Casademunt, and J.-F. Joanny, Phys. Rev. Lett. **97**, 038101 (2006).

[29] S. P. Gross, M. Vershinin, and G. T. Shubeita, Curr. Biol. **17**, R478 (2007).

[30] P. M. Shaklee, T. Idema, G. Koster, C. Storm, T. Schmidt, and M. Dogterom, Proc. Natl. Acad. Sci. USA **105**, 7993 (2008).

[31] O. Campàs, C. Leduc, P. Bassereau, J. Casademunt, J.-F. Joanny, and J. Prost, Biophys. J. **94**, 5009 (2008).

[32] W. O. Hancock, Curr. Biol. **18**, R715 (2008).

[33] R. S. Millman and G. D. Parker, *Elements of differential geometry* (Prentice-Hall, Englewood Cliffs, NJ, U.S.A., 1977).

[34] M. Spivak, *A Comprehensive Introduction to Differential Geometry (5 volumes)*, 3rd ed. (Publish or Perish Press, Berkeley, CA, U.S.A., 1999).

[35] M. do Carmo, *Differential Geometry of Curves and Surfaces* (Prentice-Hall, Englewood Cliffs, NJ, U.S.A., 1976).

[36] R. D. Kamien, Rev. Mod. Phys. **74**, 953 (2002).

[37] P.-G. De Gennes, *Scaling concepts in polymer physics* (Cornell University Press, Ithaka, NY, U.S.A., 1970).

[38] S. Lang, *Algebra*, 3rd ed. (Addison-Wesley Publishing Company, Reading, MA, U.S.A., 1993).

[39] C. W. Misner, K. S. Thorne, and J. A. Wheeler, *Gravitation* (Freeman, San Francisco, CA, U.S.A., 1973).

[40] E. A. Coddington and N. Levinson, *Theory of ordinary differential equations* (McGraw-Hill, New York, U.S.A., 1955).

[41] P. B. Canham, J. Theoret. Biol. **26**, 61 (1970).

[42] W. Helfrich, Z. Naturforsch. C **28**, 693 (1973).

[43] S. Semrau, Ph.D. thesis, Leiden University, Leiden, The Netherlands, 2009.

[44] K. A. Brakke, Exper. Math. **1**, 141 (1992).

[45] E. Evans and A. Yeung, Chem. Phys. Lipids **73**, 39 (1994).

[46] E. Evans, H. Bowman, A. Leung, D. Needham, and D. Tirrel, Science **273**, 933 (1996).

[47] I. Derényi, F. Jülicher, and J. Prost, Phys. Rev. Lett. **88**, 238101 (2002).

[48] Ou-Yang Z.-C. and W. Helfrich, Phys. Rev. A **39**, 5280 (1989).

[49] Hu J.-G. and Ou-Yang Z.-C., Phys. Rev. E **47**, 461 (1993).

[50] W.-M. Zheng and J. Liu, Phys. Rev. E **48**, 2856 (1993).

[51] F. Jülicher and U. Seifert, Phys. Rev. E **49**, 4728 (1994).

[52] F. Jülicher and R. Lipowsky, Phys. Rev. E **53**, 2670 (1996).

[53] J.-B. Fournier, Soft Matter **3**, 883 (2007).

[54] S. L. Veatch and S. L. Keller, Biochim. Biophys. Acta, Biomembr. **1746**, 172 (2005).

[55] S. L. Veatch, K. Gawrisch, and S. L. Keller, Biophys. J. **90**, 4428 (2006).

[56] H. B. Callen, *Thermodynamics and an introduction to thermostatistics*, 2nd ed. (Wiley, New York, NY, U.S.A., 1985).

[57] G. Strobl, *The physics of polymers*, 1st ed. (Springer, Berlin, Germany, 1996).

[58] S. Komura, H. Shirotori, P. D. Olmsted, and D. Andelman, Europhys. Lett. **67**, 321 (2004).

[59] S. Komura, H. Shirotori, and P. D. Olmsted, J. Phys.: Condens. Matter **17**, S2951 (2005).

[60] A. Radhakrishnan and H. McConnell, Proc. Natl. Acad. Sci. USA **102**, 12662 (2005).

[61] H. McConnell, Biophys. J. **88**, L23 (2005).

[62] G. G. Putzel and M. Schick, Biophys. J. **95**, 4756 (2008).

[63] G. G. Putzel and M. Schick, Biophys. J. **96**, 4935 (2009).

[64] J. L. Meijering, Philips Res. Rep. **6**, 183 (1951).

[65] J. Sivardière and J. Lajzerowicz, Phys. Rev. A **11**, 2101 (1975).

[66] A. Robard, D. Patterson, and G. Delmas, Macromolecules **10**, 706 (1977).

[67] M. Rabeony, D. Siano, D. Peiffer, E. Siakah-Kioulafa, and N. Hadjichristidis, Polymer **35**, 1033 (1994).

[68] R. Koningsveld, W. H. Stockmayer, and E. Nies, *Polymer phase diagrams: a textbook* (Oxford University Press, Oxford, UK, 2001).

[69] R. Lipowsky, J. Phys. II (France) **2**, 1825 (1992).

[70] S. Semrau, T. Idema, L. Holtzer, T. Schmidt, and C. Storm, Phys. Rev. Lett. **100**, 088101 (2008).

[71] S. Semrau, T. Idema, T. Schmidt, and C. Storm, Biophys. J. **96**, 4906 (2009).

[72] P. M. Chaikin and T. C. Lubensky, *Principles of condensed matter physics* (Cambridge University Press, Cambridge, U.K., 1995).

[73] D. J. Keller, H. M. McConnell, and V. T. Moy, J. Phys. Chem. **90**, 2311 (1986).

[74] E. Sparr, K. Ekelund, J. Engblom, S. Engstrom, and H. Wennerstrom, Langmuir **15**, 6950 (1999).

[75] S. A. Pandit, D. Bostick, and M. L. Berkowitz, Biophys. J. **86**, 1345 (2004).

[76] S. A. Pandit, G. Khelashvili, E. Jakobsson, A. Grama, and H. L. Scott, Biophys. J. **92**, 440 (2007).

[77] H. J. Risselada and S. J. Marrink, Proc. Natl. Acad. Sci. USA **105**, 17367 (2008).

[78] W.-C. Hung, M.-T. Lee, F.-Y. Chen, and H. W. Huang, Biophys. J. **92**, 3960 (2007).

[79] P. F. Almeida, Biochim. Biophys. Acta, Biomembr. **1788**, 72 (2009).

[80] J. F. Hancock, Nat. Rev. Mol. Cell Biol. **7**, 456 (2006).

[81] S. Fisk and B. Widom, J. Chem. Phys. **50**, 3219 (1969).

[82] F. Jülicher and R. Lipowsky, Phys. Rev. Lett. **70**, 2964 (1993).

[83] J.-M. Allain, C. Storm, A. Roux, M. B. Amar, and J.-F. Joanny, Phys. Rev. Lett. **93**, 158104 (2004).

[84] R. F. M. de Almeida, A. Fedorov, and M. Prieto, Biophys. J. **85**, 2406 (2003).

[85] A. Tian, C. Johnson, W. Wang, and T. Baumgart, Phys. Rev. Lett. **98**, 208102 (2007).

[86] F. M. Goñi, A. Alonso, L. A. Bagatolli, R. E. Brown, D. Marsh, M. Prieto, and J. L. Thewalt, Biochim. Biophys. Acta, Mol. Cell. Biol. Lipids **1781**, 665 (2008).

[87] A. R. Honerkamp-Smith, P. Cicuta, M. D. Collins, S. L. Veatch, M. den Nijs, M. Schick, and S. L. Keller, Biophys. J. **95**, 236 (2008).

[88] M. Mutz and W. Helfrich, J. Phys. (France) **51**, 991 (1990).

[89] J. J. Pécréaux, H.-G. Döbereiner, J. Prost, J.-F. Joanny, and P. Bassereau, Eur. Phys. J. E **13**, 277 (2004).

[90] D. P. Siegel and M. M. Kozlov, Biophys. J. **87**, 366 (2004).

[91] V. A. J. Frolov, Y. A. Chizmadzhev, F. S. Cohen, and J. Zimmerberg, Biophys. J. **91**, 189 (2006).

[92] J. Liu, M. Kaksonen, D. G. Drubin, and G. Oster, Proc. Natl. Acad. Sci. USA **103**, 10277 (2006).

[93] M. S. Turner, P. Sens, and N. D. Socci, Phys. Rev. Lett. **95**, 168301 (2005).

[94] W. Helfrich and R.-M. Servuss, Nuovo Cimento D **3**, 137 (1984).

[95] D. Boal, *Mechanics of the Cell* (Cambridge University Press, Cambridge, UK, 2001).

[96] S. Ramaswamy, Physica A **186**, 154 (1992).

[97] M. Goulian, R. Bruinsma, and P. Pincus, Europhys. Lett. **22**, 145 (1993).

[98] J.-M. Park and T. C. Lubensky, J. Phys. I France **6**, 1217 (1996).

[99] P. G. Dommersnes and J.-B. Fournier, Biophys. J. **83**, 2898 (2002).

[100] H. T. McMahon and J. L. Gallop, Nature **438**, 590 (2005).

[101] M. M. Müller, M. Deserno, and J. Guven, Europhys. Lett. **69**, 482 (2005).

[102] J. Zimmerberg and M. M. Kozlov, Nat. Rev. Mol. Cell Biol. **7**, 9 (2006).

[103] B. J. Reynwar, G. Illya, V. A. Harmandaris, M. M. Müller, K. Kremer, and M. Deserno, Nature **447**, 461 (2007).

[104] A. Tian and T. Baumgart, Biophys. J. **96**, 2676 (2009).

[105] S. Rozovsky, Y. Kaizuka, and J. T. Groves, J. Am. Chem. Soc. **127**, 36 (2005).

[106] M. Yanagisawa, M. Imai, T. Masui, S. Komura, and T. Ohta, Biophys. J. **92**, 115 (2007).

[107] M. M. Müller, M. Deserno, and J. Guven, Phys. Rev. E **72**, 061407 (2005).

[108] R. Lipowsky and R. Dimova, J. Phys.: Condens. Matter **15**, S31 (2003).

[109] U. Seifert, Adv. Phys. **46**, 13 (1997).

[110] W. Rawicz, B. A. Smith, T. J. McIntosh, S. A. Simon, and E. Evans, Biophys. J. **94**, 4725 (2008).

[111] E. Evans and W. Rawicz, Phys. Rev. Lett. **64**, 2094 (1990).

[112] U. Seifert and S. Langer, Europhys. Lett. **23**, 71 (1993).

[113] C. W. Gardiner, *Handbook of stochastic methods for physics, chemistry and the natural sciences* (Springer, Berlin, Germany, 2004).

[114] P. Cicuta, S. L. Keller, and S. L. Veatch, J. Phys. Chem. B **111**, 3328 (2007).

[115] E. P. Petrov and P. Schwille, Biophys. J. **94**, L41 (2008).

[116] M. V. Smoluchowski, Phys. Z. **17**, 557 (1916).

[117] J. B. McLeod, Q. J. Math. **13**, 119 (1962).

[118] L. Binglin, J. Phys. A: Math. Gen. **20**, 2347 (1987).

[119] M. Shirvani and H. van Roessel, Z. angew. Math. Phys. **43**, 526 (1992).

[120] S. Semrau, H. Schoeller, and W. Wenzel, Phys. Rev. B **72**, 205443 (2005).

[121] M. Terasaki, L. B. Chen, and K. Fujiwara, J. Cell Biol. **103**, 1557 (1986).

[122] C. M. Waterman-Storer and E. D. Salmon, Curr. Biol. **8**, 798 (1998).

[123] S. L. Dabora and M. F. Sheetz, Cell **54**, 27 (1988).

[124] R. D. Vale and H. Hotani, J. Cell Biol. **107**, 2233 (1988).

[125] V. Allan and R. Vale, J. Cell Sci. **107**, 1885 (1994).

[126] J. D. Lane and V. J. Allan, Mol. Biol. Cell **10**, 1909 (1999).

[127] F. Jülicher and J. Prost, Phys. Rev. Lett. **75**, 2618 (1995).

[128] S. M. Block, C. L. Asbury, J. W. Shaevitz, and M. J. Lang, Proc. Natl. Acad. Sci. USA **100**, 2351 (2003).

[129] R. D. Vale, T. S. Reese, and M. P. Sheetz, Cell **42**, 39 (1985).

[130] J. Howard, *Mechanics of motor proteins and the cytoskeleton* (Sinauer Associates, Sunderland, MA, USA, 2001).

[131] J. Howard, A. J. Hudspeth, and R. D. Vale, Nature **342**, 154 (1989).

[132] T. Duke, T. E. Holy, and S. Leibler, Phys. Rev. Lett. **74**, 330 (1995).

[133] P. M. Shaklee, Ph.D. thesis, Leiden University, Leiden, The Netherlands, 2009.

[134] E. Meyhöfer and J. Howard, Proc. Natl. Acad. Sci. USA **92**, 574 (1995).

[135] M. W. Allersma, F. Gittes, M. J. deCastro, R. J. Stewart, and C. F. Schmidt, Biophys. J. **74**, 1074 (1998).

[136] M. J. deCastro, R. M. Fondecave, L. A. Clarke, C. F. Schmidt, and R. J. Stewart, Nature Cell Biol. **2**, 724 (2000).

[137] P. M. Shaklee, T. Idema, L. Bourel-Bonnet, M. Dogterom, and T. Schmidt, submitted (2009).

[138] O. Rossier, D. Cuvelier, N. Borghi, P. H. Puech, I. Derényi, A. Buguin, P. Nassoy, and F. Brochard-Wyart, Langmuir **19**, 575 (2003).

[139] E. C. Young, E. Berliner, H. K. Mahtani, B. Perez-Ramirez, and J. Gelles, J. Biol. Chem. **270**, 3926 (1995).

SAMENVATTING

Structuur, vorm en dynamica van biologische membranen

Biofysica is de studie van de natuurkunde achter biologische processen. Haar werkterrein is voornamelijk de individuele cel. Cellen zijn de kleinste levende systemen en de bouwstenen van alle levende organismen. De binnenkant van een cel wordt van zijn omgeving gescheiden door een celmembraan. In eukaryotische cellen (cellen die een celkern met daarin het DNA bevatten) zorgen inwendige membranen ook voor interne structuur binnen een cel. In het onderzoek waarvan de resultaten beschreven zijn in dit proefschrift hebben we de eigenschappen van deze biologische membranen onderzocht, in het bijzonder hun structuur, vorm en dynamica. Er is een grote variatie in de moleculaire samenstelling van membranen, die directe gevolgen heeft voor hun vorm en structuur, waarbij die twee ook elkaar direct weer beïnvloeden. Bij de dynamica bestuderen we naast het membraan zelf nog een andere belangrijke component van de cel, de moleculaire motor. Motoren zijn cruciaal voor transport binnen de cel en voor het proces van celdeling. De combinatie van motoren en membranen resulteert in een actief, dynamisch systeem, zoals we dat in levende cellen vinden.

Structuur en vorm

De bouwstenen van membranen zijn lipide moleculen. Lipiden bestaan uit een deel dat goed oplosbaar is in water (een hydrofiele 'kop') en één of meer lange, vetachtige delen die slecht oplosbaar zijn in water (hydrofobe 'staarten'). In een omgeving met veel water organiseren lipide moleculen zich daardoor spontaan in grotere structuren waarin de koppen in contact staan met watermoleculen, terwijl de staarten daarvan worden afgeschermd. Voor lipiden die ongeveer een cilindervorm hebben is de optimale structuur een dubbele laag, met de koppen aan de buitenkant en de staarten binnenin. Alle biologische membranen bestaan uit zo'n dubbele laag van lipiden. De lipiden vormen met elkaar een tweedimensionale vloeistof: ze kunnen vrij bewegen in de twee richtingen binnen het membraan, maar het membraan niet in de derde richting verlaten.

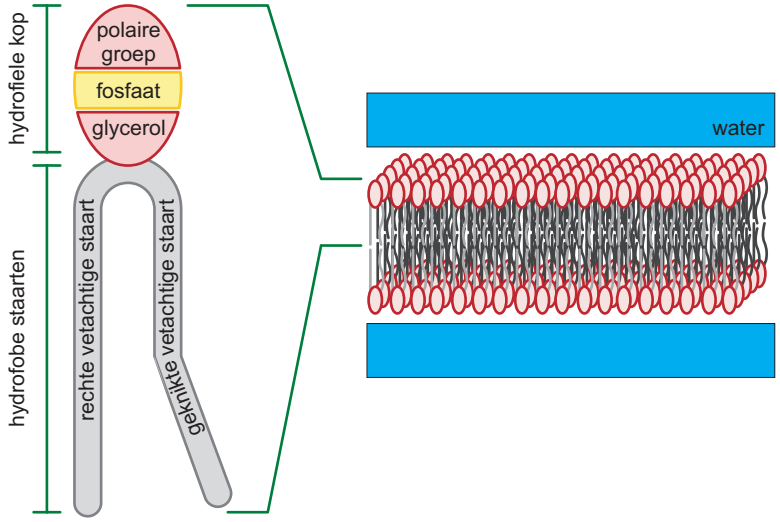

Figuur 8.1: Membranen zijn opgebouwd uit lipide moleculen, met een hydrofiele (in water oplosbare) kop en één of meer hydrofobe (niet in water oplosbare) staarten. Wanneer we proberen lipiden in water op te lossen, vormen ze spontaan een dubbele laag met de koppen aan de buiten- en de staarten aan de binnenkant.

De meeste lipiden in biologische membranen hebben twee staarten. Een belangrijke uitzondering is cholesterol, dat maar één staart heeft en bovendien een vrij kleine kop. De staarten kunnen recht zijn, maar ook knikken bevatten, een gevolg van hun moleculaire samenstelling (knikken komen voor op punten waar de polymeerketen een onverzadigde, dubbele verbinding tussen twee opeenvolgende koolstofatomen heeft). De richting van een stuk staart na een knik, gerekend vanaf de kop, is onbepaald, terwijl die van een rechte staart vastligt. Hierdoor is een membraan gemaakt van lipiden met geknikte staarten minder geordend dan een membraan dat bestaat uit lipiden met rechte staarten. Dit verschil in ordening is zo bepalend voor de interne structuur van het membraan, dat de membranen met verschillende mate van ordening in een verschillende fasetoestand zitten. In beide gevallen is het membraan een vloeistof en de twee fasetoestanden duiden we aan als geordende vloeistof (L_o) en ongeordende vloeistof (L_d). Als we een mengsel maken waarin een lipide met geknikte staarten, een met rechte staarten en cholesterol in de juiste verhouding voorkomen, ontstaat een membraan waarin zowel L_o als L_d gebiedjes (die we domeinen noemen) voorkomen.

Het proces van faseschеiding in L_o en L_d domeinen binnen het membraan is hetzelfde als het spontaan ontmengen van bijvoorbeeld water en olie. Net zoals tussen water en olie een oppervlaktespanning ontstaat op de grens tussen de twee vloeistoffen, is er ook een spanning tussen de domeinen in het membraan, maar dan een lijnspanning (het membraan is immers een tweedimensionale vloeistof en de rand van een domein daarom een eendimensionale lijn). Deze lijnspanning zorgt er in de eerste plaats voor dat de domeinen cirkelvormig worden: de vorm met de kortste omtrek voor een bepaald oppervlak. In de tweede plaats zorgt de lijnspanning ervoor dat het gunstig is om domeinen samen te voegen. Als gecombineerd domein kunnen twee kleine domeinen immers een grotere cirkel vormen en zo samen een kortere rand krijgen. Het ligt daarom voor de hand te verwachten dat we altijd zien dat alle domeinen samensmelten. In de praktijk gebeurt dat ook vaak, maar soms veel langzamer dan we zouden verwachten. Dat komt door een derde effect van de lijnspanning: die vervormt ook het membraan om de rand van een domein korter te maken. Dat gebeurt door gebruik te maken van de derde dimensie: door het domein en het membraan eromheen te buigen, kan de rand van het domein korter worden. Hoeveel energie het kost om het membraan zo te buigen hangt weer af van de samenstelling en fasetoestand van het membraan. De vorm die het membraan aanneemt is daardoor een balans tussen lijnspanning aan de ene en buigzaamheid aan de andere kant. Het buigen van een domein om hem een kortere rand te geven heeft invloed op zijn omgeving: die vervormt mee. Dat heeft een remmend effect op het proces van het samensmelten van de domeinen, want om twee domeinen bij elkaar te brengen moet het membraan eerst extra gebogen worden. Daardoor ontstaat een afstotende kracht tussen de domeinen, en verdelen ze zich over het membraan, waardoor het membraan gestructureerd wordt. Voor gesloten membranen met ruwweg

een bolvorm (een erg simpel model voor het membraan van een cel) blijken grote domeinen elkaar bovendien harder af te stoten dan kleine, wat gevolgen heeft voor de verdeling van domeinen over het hele membraan. We hebben het fasegedrag van de membranen bestudeerd in hoofdstuk 3. In hoofdstuk 4 hebben we de vorm van de membranen uitgerekend aan de hand van een model waarin de lijnspanning en de buigbaarheid van de verschillende domeinen zijn meegenomen. Bovendien hebben we de berekende vorm vergeleken met experimenteel bepaalde vormen en zo de buigbaarheid en lijnspanning gemeten. In hoofdstuk 5 hebben we gekeken naar de krachten tussen de domeinen. De verdeling van domeinen over het hele membraan is het onderwerp van hoofdstuk 6, waarin blijkt dat de domeinen spontaan worden gesorteerd naar grootte.

Dynamica en motoren

Moleculaire motoren zijn de werkpaarden van de cel. Motoren spelen een belangrijke rol bij het transport binnen een cel, bij het kopieëren van de genetische code in het DNA en bij het proces van celdeling. De motoren die wij bestuderen hebben één of twee 'voeten' waarmee ze kunnen lopen over het cytoskelet, een netwerk van lange, stijve polymeren in een cel dat een vergelijkbare functie heeft als het skelet in het menselijk lichaam (al is het cytoskelet enerzijds veel eenvoudiger en anderzijds veel dynamischer). Naast voeten hebben de motoren ook een 'laadzone', een plek waar een nuttige lading verankerd kan worden. Die lading is vaak verpakt in een membraan, en is soms zelfs het membraan zelf. Door collectief aan een membraan te trekken kunnen motoren het vervormen, en zo meewerken aan verschillende processen die in een cel optreden, zoals bijvoorbeeld het opnemen van voedsel en het transporteren van eiwitten. Het proces dat we in het bijzonder bestudeerd hebben is het ontstaan van membraantubes: lange, dunne buisjes van membraan die met relatief geringe kracht uit een membraan getrokken kunnen worden. Eén individuele motor is niet sterk genoeg om zo'n tube te trekken, maar door met vijf of zes motoren samen te werken lukt dat wel.

Een eigenschap van de motoren die in belangrijke mate de dynamica van het tube trekken bepaalt is hun processiviteit. Motoren met twee voeten, die kunnen lopen door steeds de ene voor de ander te zetten, hebben een hoge processiviteit (we noemen ze processieve motoren). Een groepje van processieve motoren kan tubes maken die zo lang kunnen worden als de cel zelf, waarbij de tube steeds met constante snelheid vooruit wordt getrokken. Aan de andere kant zijn er ook niet-processieve motoren, met maar één voet (of maar één actieve), die daardoor per keer ook maar één stap kunnen zetten. Opmerkelijk genoeg blijken ook deze motoren collectief tubes te kunnen trekken. Deze tubes gedragen zich wel compleet anders dan die van de processieve motoren: ze groeien met variabele snelheden en wisselen dat af met retracties, waarin ze snel over relatief grote stukken kunnen terugtrekken. Met een model

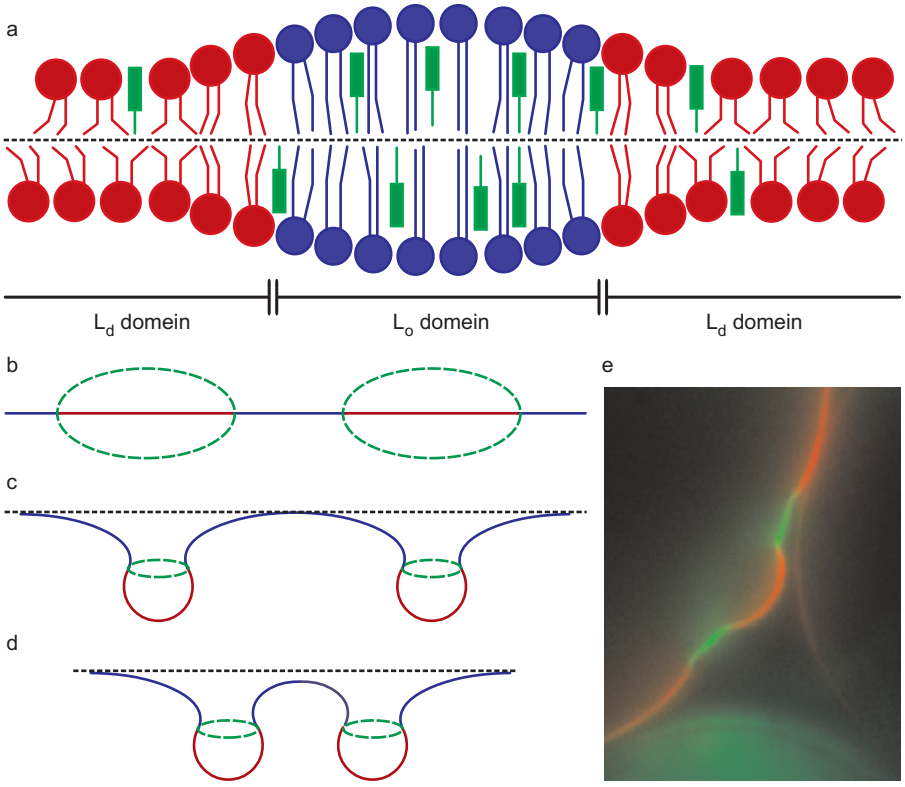

Figuur 8.2: Membranen die bestaan uit een combinatie van cholesterol , lipiden met rechte staarten en lipiden met geknikte staarten in de juiste verhouding, ondergaan spontane fasescheiding. Figuur a toont een schets van een membraan met geordende (L_o) en ongeordende (L_d) domeinen. Als gevolg van de fasescheiding ontstaat een lijnspanning op de rand van de domeinen. In figuur b, c en d is er een lijnspanning op de groene gestreepte lijn. Door het domein te laten uitdeuken buiten het vlak van het membraan wordt de rand van het domein korter, maar wordt domeinen samenvoegen wel moeilijker. Figuur e toont een microscoopopname van een membraan waarin de verschillende domeinen met rood en groen gelabeld zijn.

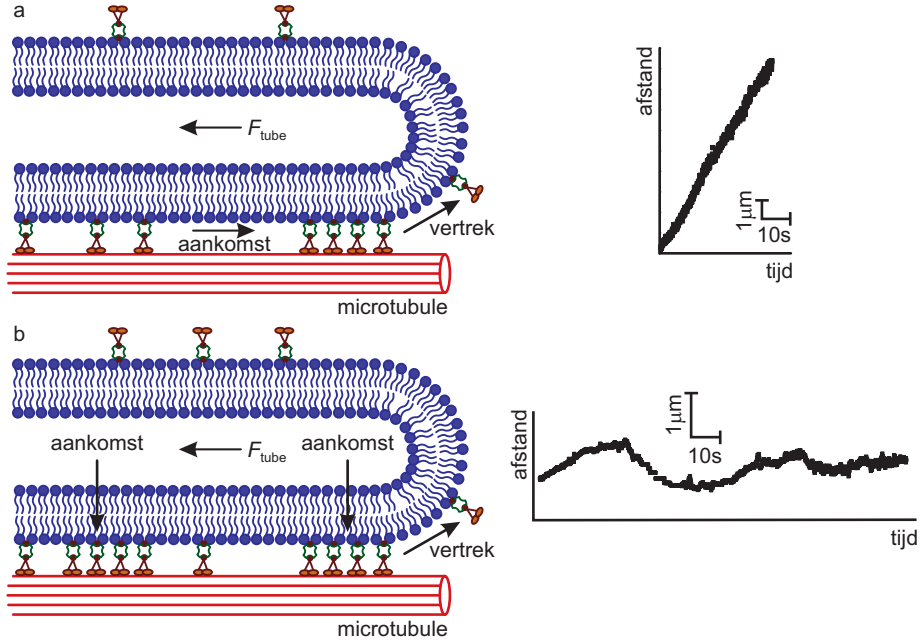

Figuur 8.3: Moleculaire motoren die verantwoordelijk zijn voor de transportprocessen binnen een cel hebben één of twee actieve voeten waarmee ze over onderdelen van het cytoskelet kunnen lopen (hier een microtubule). Door samen te werken kunnen zulke motoren membraantubes trekken. De dynamica van zo'n tube hangt sterk af van de processiviteit van de motoren. Processieve motoren kunnen continu trekken met constante snelheid (figuur a). Motoren die niet trekken kunnen de trekkende motoren inhalen en gaan meehelpen. Niet-processieve motoren kunnen wel tubes trekken, maar die fluctueren in lengte (figuur b). Motoren kunnen wel clusters vormen langs de tube, maar geen andere clusters inhalen. Als de trekkende cluster te klein wordt, trekt de tube zich terug tot de volgende cluster, waardoor een oscillerend patroon ontstaat.

waarin de motoren in clusters samenwerken en deze clusters gevormd worden langs de hele tube kunnen we dit gedrag verklaren en kwantificeren. Bovendien blijkt uit computersimulaties van dit systeem dat dit dynamische proces van groei en terugtrekking leidt tot een gereguleerde lengte van de tube, waarbij die lengte weer bepaald wordt door de samenstelling van het membraan. Deze processen zijn het onderwerp van hoofdstuk 7. In levende systemen spelen ze een belangrijke rol. De stabiele, lange tubes die getrokken worden door processieve motoren fungeren als brug en verbinding tussen verschillende onderdelen van een cel, en zelfs tussen cellen onderling. De dynamische tubes van de niet-processieve motoren zorgen ervoor dat het membraan tegelijkertijd een groot en vooral dynamisch oppervlak heeft zodat voedingsstoffen en eiwitten snel opgenomen kunnen worden en dat het bovendien gemakkelijk delen kan afsplitsen.

De structuur, vorm en dynamica van membranen zijn aan de ene kant biologische eigenschappen van en cruciaal voor de processen die zich afspelen binnen een cel. Anderzijds zijn ze het gevolg van de onderliggende fysische wetten en kunnen als natuurkundig systeem beschreven en bestudeerd worden. Eenzelfde soort fysische beschrijving kan gegeven worden van veel andere biologische processen binnen de cel. Uiteindelijk is de cel echter meer dan de som van de delen, en moeten we, om haar als geheel te kunnen begrijpen, beschrijvingen vinden voor het complexe systeem waarin al deze delen met elkaar samenhangen. De combinatie van membranen en motoren in hoofdstuk 7 is daar een voorbeeld van, al gaat het ook daar om slechts een eerste stap. In de biofysica valt nog veel te ontdekken.

PUBLICATIONS

1. S. Semrau*, T. Idema*, L. Holtzer, T. Schmidt, and C. Storm, *Accurate determination of elastic parameters for multi-component membranes*, Phys. Rev. Lett. **100**, 088101 (2008) [Chapter 4].

2. P.M. Shaklee*, T. Idema*, G. Koster, C. Storm, T. Schmidt, and M. Dogterom, *Bidirectional membrane tube dynamics driven by nonprocessive motors*, Proc. Natl. Acad. Sci. USA **105**, 7993-7997 (2008) [Chapter 7].

3. S. Semrau*, T. Idema*, T. Schmidt, and C. Storm, *Membrane mediated interactions measured using membrane domains*, Biophys. J. **96**, 4906-4915 (2009) [Chapter 5].

4. T. Idema, J.M.J. van Leeuwen, and C. Storm, *Phase coexistence and line tension in ternary lipid systems*, accepted for publication in Phys. Rev. E (2009) [Chapter 3].

5. T. Idema*, S. Semrau*, C. Storm, and T. Schmidt, *Membrane mediated sorting*, submitted (2009) [Chapter 6].

6. M. Basan, T. Idema, M. Lenz, J.-F. Joanny, and T. Risler, *The cadherin-catenin system as a pathway for contact inhibition and tumorigenesis*, submitted (2009).

7. P.M. Shaklee, T. Idema, L. Bourel-Bonnet, M. Dogterom, and T. Schmidt, *Kinesin recycling in stationary membrane tubes*, submitted (2009).

(*) authors contributed equally.

CURRICULUM VITAE

Op 20 april 1981 ben ik geboren in Winterswijk. In Aalten bezocht ik het Christelijk College Schaersvoorde, waar ik in 1999 het VWO diploma behaalde. Daarna studeerde ik wiskunde en natuurkunde aan de Universiteit Leiden. Mijn natuurkundestudie sloot ik af met een scriptie over de stroming in viscoelastische vloeistoffen in de groep van prof. dr. ir. W. van Saarloos. Op 31 augustus 2004 behaalde ik cum laude het doctoraaldiploma natuurkunde. In het daarop volgende jaar sloot ik mijn wiskundestudie af met een scriptie over dynamische systemen, in het bijzonder Lotka-Volterra modellen, in de groep van prof. dr. S.M. Verduyn Lunel. Ook het wiskundedoctoraal verkreeg ik cum laude op 29 juni 2005.

In september 2005 begon ik aan een promotieonderzoek in de theoretische natuurkunde, binnen de statistische biofysicagroep van prof. dr. H. Schiessel aan het Instituut Lorentz van de Universiteit Leiden. Gedurende dit onderzoek, waarvan de belangrijkste resultaten zijn opgenomen in dit proefschrift, werkte ik op theoretisch gebied voornamelijk samen met dr. C. Storm (2005-2007 Universiteit Leiden, daarna Technische Universiteit Eindhoven). Daarnaast heb ik intensief samengewerkt met de experimentele groepen van prof. dr. T. Schmidt (Universiteit Leiden) en prof. dr. M. Dogterom (Universiteit Leiden en AMOLF-Amsterdam). Gedurende mijn promotieonderzoek verbleef ik twee maanden (januari en februari 2008) in de groep van prof. dr. J.-F. Joanny aan het Institut Curie in Parijs.

In september 2005 bezocht ik een tweewekelijkse zomerschool in Leuven (België), en in juli 2006 een van vier weken in Boulder (Colorado, USA). Daarnaast bezocht ik korte (zomer)scholen in Heeg, Driebergen en Bad Honnef (Duitsland). Ik heb mijn werk gepresenteerd op internationale conferenties in Cargèse (Frankrijk), Baltimore (Maryland, USA), Amsterdam, Les Houches (Frankrijk) en Parijs (Frankrijk) en nationale conferenties in Leiden, Lunteren, Eindhoven en Veldhoven. Ook heb ik presentaties over mijn werk gegeven in seminars in Leiden, Krakow (Polen), Parijs (Frankrijk), Los Angeles (Californië, USA), Philadelphia (Pennsylvania, USA) en Cambridge (Verenigd Koninkrijk).

Tenslotte heb ik tijdens mijn promotie werkcolleges gegeven in de vakken statistische fysica 1 en klassieke mechanica 2 en meegewerkt aan een serie lezingen wiskunde voor fysici. Van januari 2007 tot en met december 2008 was

ik lid en plaatsvervangend voorzitter van de centrale ondernemingsraad van de stichting FOM.

DANKWOORD

In tegenstelling tot het stereotiepe beeld van de solitaire verstrooide professor is wetenschap bedrijven een collectief gebeuren. Voor mijn promotieonderzoek geldt dat wel in het bijzonder: alle resultaten in dit proefschrift komen voort uit intensieve samenwerkingen met andere theoretici en experimentalisten. Zonder deze manier van werken was het zeker niet mogelijk geweest om onderzoek in deze vorm te doen. Dat geldt in het bijzonder de zeer vruchtbare en plezierige samenwerking met mijn experimentele collega-promovendi Stefan en Paige. Meer passende paranimfen bij mijn promotie dan jullie zijn dan ook niet denkbaar. Daarnaast heb ik bijzonder veel gehad aan de vele discussies met Kees en Hans, waarin veel ideeën zijn ontstaan en afgeschoten, maar er altijd aan het eind iets overbleef.

During my PhD I had the privilege to encounter many groups of excellent scientists. The Institute Lorentz, my home institute for the last four years, is both scientifically and socially a wonderful place to work. Other groups with whom I interacted frequently include the experimental biophysics group and the applied mathematics group in Leiden, the theoretical biophysics group at the VU in Amsterdam, the biophysicists and associated 'overlopers' at AMOLF and the theoretical and experimental soft matter groups at the Institut Curie. I would like to thank all of you for the stimulating discussions as well as the many fun hours we had together.

Een aantal mensen in deze groepen wil ik graag meer persoonlijk bedanken. Jasper, Johan, Markus and Martin, thanks for being excellent roommates and for sticking out with me. Rhoda en Liesbeth, dankjewel allebei voor het delen van de ups en downs en voor jullie altijd open deur. Wouter, Paul en Stefan, bedankt voor jullie gezelschap op verschillende buitenlandse reizen, die ze zowel makkelijker als leuker maakten. Olaf en Jan, met jullie erbij werd het werkcollege geven een stuk leuker en Marianne en Fran bedankt voor jullie inzet en grote vaardigheid bij het gedaan krijgen van het simpele tot het onmogelijke.

Hoewel onderzoek doen een zowel interessante als aangename activiteit is, is het niet de enige waarmee ik mij heb beziggehouden - wat indirect weer bijdraagt aan het verbeteren van datzelfde onderzoek. Een leerzame afwisseling was het werk in de COR-FOM, waarvoor ik de overige leden wil bedanken. Niet

minder belangrijk zijn de vele contacten binnen de LBG, waar ik op een andere maar evengoed inspirerende manier ook veel geleerd heb. In het bijzonder wil ik daarbij Ad, Eveline, Sandra en Mijke bedanken, voor de verbondenheid en vriendschapsband die ik van elk van jullie op je eigen manier gekregen heb.

Roel en Harm-Jan, dank jullie wel voor onze eenheid in verscheidenheid, en veel succes met jullie eigen nieuwe uitdagingen. Mijn vader wil ik bedanken voor zijn pragmatische blik en voor het mij leren van de 80/20 regel en mijn moeder voor haar geduld en altijd luisterend oor. Nog veel belangrijker, en dat geldt voor jullie allebei, zijn jullie onvoorwaardelijke steun en de mogelijkheid altijd op jullie te kunnen terugvallen. Mariska, dankjewel voor het vertrouwen dat je me geeft, en voor de manier waarop je mij mezelf laat zijn en dat tegelijkertijd prachtig aanvult!